Geodetic and meteorological studies of the water vapor delay signal in InSAR with the use of numerical weather model

数値気象モデルを用いたInSARにおける水蒸気遅延シグナルの測地学的・気象学的研究

Youhei Kinoshita

Department of Natural History Sciences, Graduate School of Science,

Hokkaido University

Submitted for the degree of Doctor of Philosophy

February 2014

Contents

List of Figures

List of Tables

Abstract

Spatial and temporal variations of the neutral atmosphere cause fluctuations in the propagation delay of radio waves that are used in space geodetic techniques such as the Global Navigation Satellite system (GNSS), Very Long Baseline Interferometry (VLBI), and Synthetic Aperture Radar Interferometry (InSAR). It is difficult to precisely model the neutral atmospheric delay even if the state-of-the-art numerical weather simulation is used because of the high spatiotemporal variability and the poor observation of water vapor in the lower atmosphere. Therefore, this atmospheric delay results in significant spatial phase changes in InSAR images. In GNSS, the propagation delay effect due to the atmosphere can be estimated in an efficient way in conjunction with the position determination, whereas in InSAR the propagation delay effect can not be easily separated from other signals associated with actual surface deformation and errors due either to orbit inaccuracy or to digital elevation model (DEM). In contrast, without any crustal deformations and other errors, InSAR can detect water vapor distribution with high spatial resolution and thus is potentially useful for meteorological applications. In this thesis, I study the propagation delay due to water vapor in InSAR images as both meteorological signal and noise for detecting surface deformations using Phased Array type L-band SAR (PALSAR) aboard Advanced Land Observing Satellite (ALOS) data and the high-resolution nu-

merical weather model (NWM). The thesis includes the following two topics:

(1) Are numerical weather model outputs helpful to reduce tropospheric delay signals in InSAR data?

In InSAR, the delay effect due to water vapor can generate apparent signals on the order of a few centimeters or more, and prevent us from detecting such geophysical signals as those due to secular crustal deformation. In order to examine if and to what extent NWM outputs are helpful to reduce the tropospheric delay signals at spatial scales of 5~50 km wavelengths, we compared three approaches of tropospheric signal reduction, using 54 interferograms in central Hokkaido, Japan. The first approach is the conventional topography-correlated delay correction that is based on the regional DEM. The second approach is based on the Japan Meteorological Agency's operational meso-scale analysis model (MSM) data, where we compute tropospheric delays and subtract them from the interferogram. However, the MSM data are available at predefined epochs, and their spatial resolution is about 10 km, and therefore we need to interpolate both temporally and spatially to match with interferograms. Expecting to obtain a more physically plausible reduction of the tropospheric effects, we ran a 1-km mesh high-resolution numerical weather model WRF (Weather Research and Forecasting model) by ourselves, using the MSM data as the initial and boundary conditions. The third approach is similar to the second approach except that we make use of the WRF-based tropospheric data.

Results show that if the topography-correlated phases are significant, both the conventional DEM-based approach and the MSM-based approach reveal comparable performances. However, when the topography-correlated phases are insignificant,

none of the approaches could efficiently reduce the tropospheric phases. Although it could reduce the tropospheric signals in a local area, in none of the case studies did the WRF model produce the "best" performance. Whereas the global atmospheric model outputs are shown to be effective in reducing long-wavelength tropospheric signals, we consider that further improvements are needed for the initial and boundary condition data for high-resolution NWM, so that the NWM-based approach will become more reliable even in the case of a non-stratified troposphere.

(2) InSAR observation and numerical modeling of the water vapor signal during a heavy rain: A case study of the 2008 Seino event, central Japan

This study reports the first detection and analysis of a localized water vapor distribution obtained using InSAR during the Seino heavy rain episode on 2 September 2008. The InSAR data retrieved during the ALOS/PALSAR emergency observations for the event revealed a radar line-of-sight (LOS) change of up to 130 mm within 10 km caused by water vapor. Based on the signal, we estimated the three-dimensional water vapor distribution using the ray-tracing method, which indicated a column of nearly saturated water vapor within a 10 km^2 area reaching from the surface to 9000 m above ground level. To geophysically confirm this signal, numerical weather simulations were performed using WRF model, revealing a deep convection that caused a similar delay signal in the interferogram and was initiated by orographic lift caused by the Yoro Mountains. Another simulation that did not include the Yoro Mountains did not produce a deep convection. These simulation results demonstrated the importance of realistic topography in the high-resolution numerical weather modeling. The WRF simulation also suggested that the effect of

hydrometeors can account for approximately 20 % of the maximum LOS change but this effect is even more localized than the effect of water vapor.

概要

中性大気の時空間的変動は衛星測位システム (GNSS), 超長基線電波干渉法 (VLBI), 合成開口レーダー干渉法 (InSAR) などのマイクロ波を用いる宇宙測地技術に伝搬遅延効果を引き起こす. 特に下層大気中の水蒸気の時空間的変動および観測自体の少なさから, 最新の数値気象モデルを以てしても中性大気による伝搬遅延効果を正確に見積もることは困難である. それゆえに伝搬遅延効果は空間的な位相変化として InSAR 画像中に現れる. GNSS の場合には, 中性大気による伝搬遅延効果は観測点の位置と同時に高い精度で推定されるが, InSAR の場合には中性大気伝搬遅延, 特に対流圏以下で起こる対流圏伝搬遅延は地殻変動, 軌道推定誤差, 数値標高モデル (DEM) の誤差, 電離層擾乱による位相変化などのシグナルから分離するのが容易ではない. 一方で, 地殻変動などの他のシグナルの寄与が無い場合には, InSAR は非常に高い空間分解能で大気中の水蒸気の分布を捉えることができ, それゆえに気象学的な応用が可能である. 本論文では, InSAR 画像に現れる水蒸気による伝搬遅延について, それを気象学的なシグナルと見做した場合と地殻変動検出におけるノイズと見做した場合について ALOS/PALSAR データと高空間分解能数値気象モデルを用いて行った研究について記述する. 本論文は以下の 2 つの話題について記述する.

(1) 数値気象モデル WRF モデルを用いた InSAR における対流圏伝搬遅延補正

効果の検証

InSAR において, 水蒸気による伝搬遅延効果は数 cm からそれ以上の見かけ上のシグナルとなって現れ, それゆえに経年的地殻変動のような地球物理学的なシグナルの検出にとって障害となっている. 数値気象モデルの計算結果が空間波長 5 - 50 km の対流圏伝搬遅延の補正にどの程度有効なのかを検証するため, 我々は北海道中央部での 54 の干渉画像に対して以下に述べる 3 つの対流圏伝搬遅延補正法の効果を比較検証した. 第一の補正法は従来から用いられている DEM に基づいた地形相関遅延補正法である. 第二の補正法は気象庁のメソ数値気象モデル (MSM) データに基づいた補正法で, MSM データから伝搬遅延量を計算し, 干渉画像から引くものである. ここで MSM データは 3 時間毎のデータしか存在しておらず, かつ水平空間分解能も 10 km と干渉画像と比べて粗いため, 干渉画像に合わせるために時間的にも空間的にも内挿する必要がある. より物理的に最もらしい遅延補正を行うため, 我々は数値気象モデル WRF(Weather Research and Forecasting model) を用いて SAR 観測時刻における大気状態のシミュレーションを行った. 水平空間分解能は 1 km, 初期値・境界値には MSM データを用い, WRF の計算結果から MSM 補正法と同様に伝搬遅延量の計算を行った.

補正の結果, 干渉画像中に地形に相関したシグナルが卓越している場合には, DEM による補正と MSM による補正は同等の補正効果を示した. しかしながら, 地形に相関したシグナルが小さい場合には, 3 つのいずれの補正法も有効ではなかった. WRF による補正法は, 事例によっては局所的な伝搬遅延の補正に成功していたが, 全体としては他の補正法ほど有効な補正をしなかった. 全球大気モデルによる補正が対流圏伝搬遅延の長波長成分を有効に補正できることが示されている一方, 高空間分解能の NWM を以てしても対流圏伝搬遅延のより短波長な成分を有効に補正できないのは初期値・境界値の現実大気再現度の

不正確さに起因しているのであろう. より現実大気に近い初期値・境界値を用いることで, 対流圏伝搬遅延の地形に非相関な成分に対しても NWM は有効な補正法になるであろう.

(2) InSAR データで捉えた 2008 年西濃豪雨時の水蒸気シグナル: 3 次元水蒸気モデリングと WRF モデルを用いた再現実験

本研究は InSAR で捉えた 2008 年 9 月 2 日の西濃豪雨時の水蒸気シグナルの検出事例の紹介とその事例解析の結果を報告する. ALOS/PALSAR の緊急観測から得られた干渉画像から空間スケール約 10 km で視線方向に約 130 mm 変化する局所的な水蒸気伝搬遅延シグナルが検出された. この局所的シグナルに基づいて我々は波線追跡法を用いて 3 次元水蒸気分布の推定を行った. 推定の結果, 局所的シグナルの位置に地表から高度 9000 m に達する水蒸気の飽和した領域を推定した. この局所的シグナルを地球物理学的に検証するため, 我々は数値気象モデルの WRF を用いて局所的シグナルの再現実験を行った. その結果, 干渉画像での局所的シグナルに振幅・空間スケール共に似た伝搬遅延を引き起こす発達した対流を再現することに成功した. この対流はシグナルの南約 10 km に存在する養老山地での地形性上昇流によって引き起こされていることが示唆された. そこで地形による影響を調べるため DEM から養老山地を取り除いた感度実験を行った結果, 元のシミュレーションで再現された対流は再現されなかった. この結果は高空間分解能の数値気象モデルにとって現実的な地形が重要であることを示している. また, WRF のシミュレーション結果から水蒸気ではなく降水粒子による伝搬遅延の影響を見積もった結果, 降水粒子の影響は水蒸気による伝搬遅延量の約 20 %に達し, その効果は水蒸気による伝搬遅延の領域に比べより局在化していた.

Acknowledgment

This dissertation concludes five years of my graduate study at Hokkaido University. I would like to express my gratitude to all the people who have helped me in my graduate course.

First and foremost, I would like to offer my special thanks to my superviser, Professor Masato Furuya for his guidance, close support, discussion and mentorship during the course of my graduate student at Hokkaido University. He also gave me opportunities to attend academic meetings in both home and abroad so that I had good fortunes to meet many scientists.

Also, I would like to thank Professor Kosuke Heki, Professor Junji Koyama, Professor Kiyoshi Yomogida, Professor Kazunori Yoshizawa, Professor Masaru Inatsu, Professor Yasushi Fujiyoshi, and Dr. Yuta Mitsui for their constructive comments. In particular, Professor Masaru Inatsu gave me insightful comments and discussions from the standpoint of a meteorologist. I am deeply grateful to all my colleagues in Space Geodesy laboratory in Hokkaido University for discussions and warm support.

I would like to appreciate Dr. Ryuichi Ichikawa, Dr. Thomas Hobiger at National Institute of Information and Communications Technology, and Dr. Masanobu Shimada at Earth Observation Research Center at Japan Aerospace Exploration Agency as both my advisers and co-authors of my study.

I would like to thank JSPS fellowship for a grant that makes it possible to complete this study. I was supported by this fellowship from a financial perspective.

The PALSAR level 1.0 data in this study were provided by the PALSAR Interferometry Consortium to Study our Evolving Land surface (PIXEL) under cooperative research contracts between the Earthquake Research Institute at the University of Tokyo and JAXA. The PALSAR data belong to JAXA and the Ministry of Economy, Trade and Industry. The weather radar data and MSM data were acquired from the GPV archive site (http://database.rish.kyoto-u.ac.jp/arch/jmadata/) managed by the Research Institute for Sustainable Humanosphere, Kyoto University. GEONET data were provided by the Japan Association of Surveyors.

Chapter 1

Introduction

1.1 Geodetic monitoring

Geodesy is one of the oldest science with a history of more than two thousand years which determines the size, shape, and rotation of the Earth using measurements of distance, time, and gravity. The traditional measurements were associated with land surveying (to measure the distance and direction) and gravity observations (to determine the geoid). Geodesists study geodynamical phenomena such as crustal motion, tides, and polar motion using these observation data and mathematical model. Although traditional geodetic observations have been contributed to determine the shape and rotation of the Earth and to study geodynamical phenomena, they were insufficient in terms of both density and accuracy. Measurements were limited to certain areas in the world, and the frequent observations were lacking. To elucidate mechanisms of natural phenomena occurring on and in the Earth scientifically,

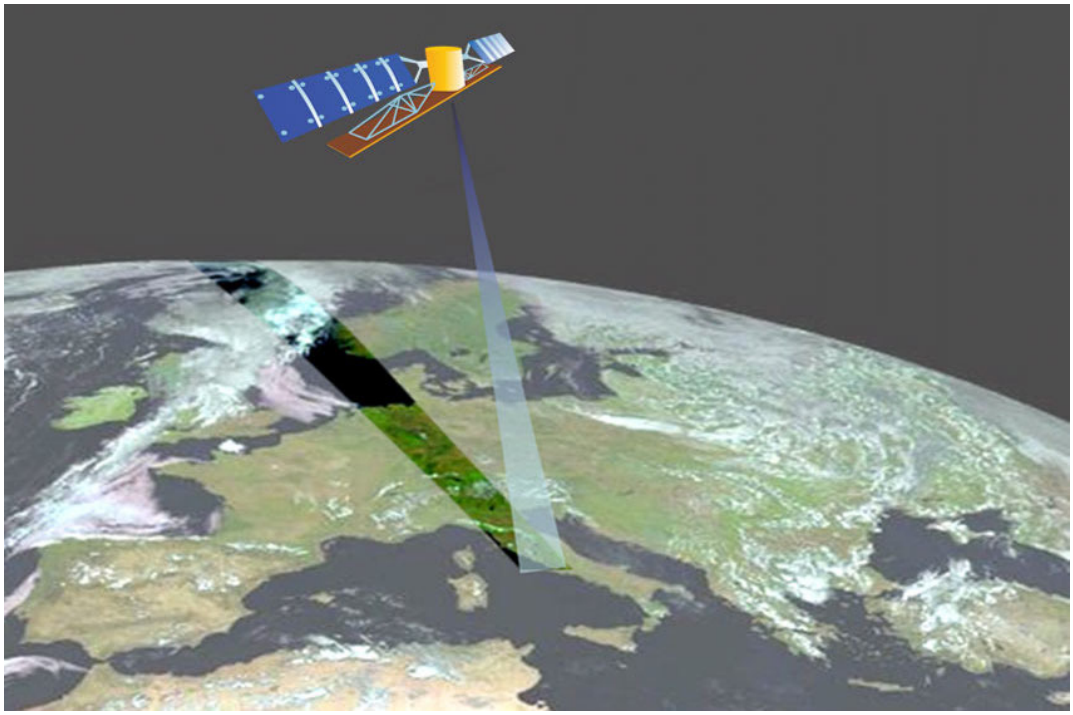

Figure 1.1: Schematic of a SAR satellite acquiring strip map images. (http://treuropa.com/technique/sar-imagery/)

precise and dense observations are essential.

Since the end of twentieth century, new type of geodetic techniques such as Global Navigation Satellite System (GNSS) and Very Long Baseline Interferometry (VLBI) has been playing an important role to determine the Earth's rotation and orientation, to measure motions of the tectonic plates [*Seeber*, 2000]. The field of these new techniques are often called *space geodesy*. In Particular, GNSS was originally designed as a navigation and time transfer system [*Bevis et al.*, 1992]. The development of the GNSS technology over the past decade has made GNSS as a powerful geodetic tool for studying crustal deformation with a precision of centimeters to sub-millimeters [*Segall and Davis*, 1997]. Concurrently, Synthetic Aperture Radar (SAR), one of the remote sensing techniques, has been proven to be a power-

ful tool for studying geophysical phenomena (Figure 1.1). SAR observation has been used to derive high-resolution topographic maps of both the Earth and Venus [*Meyer and Sandwell*, 2012], because SAR is an active radar that transmits microwaves and receives scattered signals in itself. Since 1990's, SAR Interferometry or interferometric SAR (InSAR) has evolved, and is now considered an established method for measuring surface topography at high spatial and vertical resolution as well as for measuring surface deformations associated with earthquakes, volcanic activities, and other ground deformation [e.g. *Massonnet and Feigl*, 1998; *Delacourt et al.*, 1997; *Galloway et al.*, 1998]. In a narrow sense, SAR is not a method of space geodesy. Nevertheless, because some fundamentals and applications are similar to other geodetic techniques, SAR could be regarded as the one of geodetic tools.

1.2 Propagation delay for space geodesy

The refractive index in the Earth's atmosphere is different from that in the vacuum. This fact causes the variation of velocity and the ray-propagating direction for the microwave used in space geodetic techniques, which is called the propagation delay effect. The principle of the propagation delay can be explained by the Snell's law (Figure 1.2),

$$\frac{\sin\theta_1}{\sin\theta_2} = \frac{v_1}{v_2} = \frac{n_2}{n_1}. \tag{1.1}$$

Here, θ_1 and θ_2 denote the incidence angle and the refracting angle, v_1 and v_2 denote velocity of propagating waves in medium 1 and medium 2, respectively, and n_1 and n_2 denote refractive indices in medium 1 and medium 2, respectively. The propagation delay effect influences the precision of the determination of the receiver's position

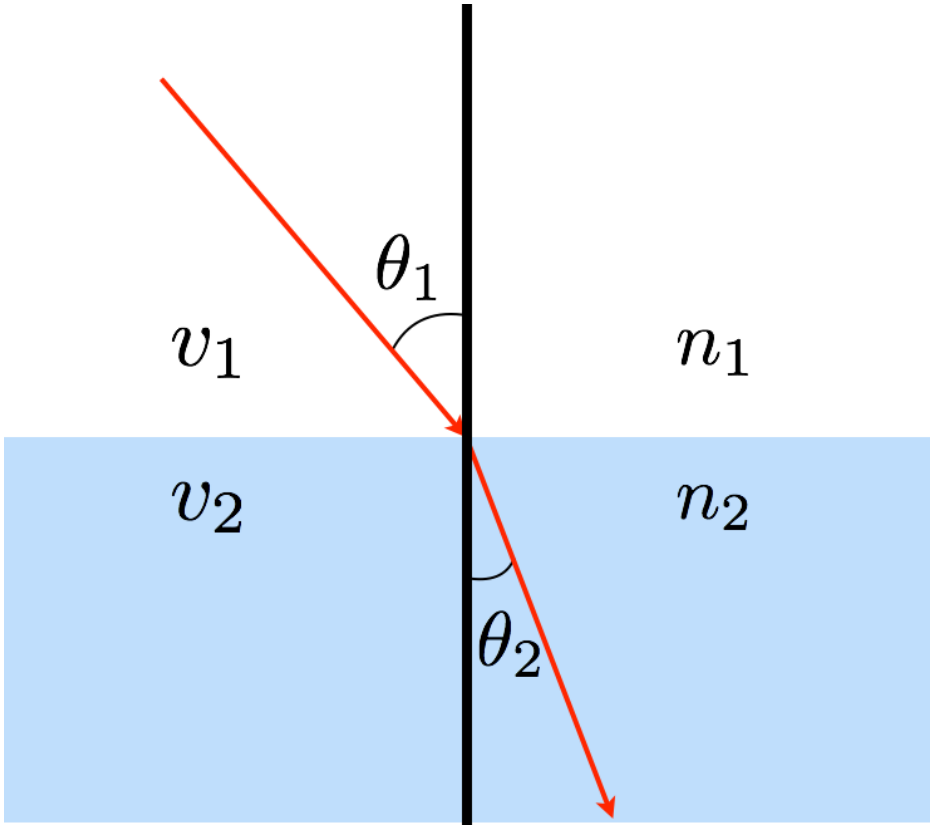

Figure 1.2: Schematic of the Snell's law.

and the detection of the crustal deformation. In this sense, this effect have to be modeled appropriately to separate from the actual deformation.

The presence of the atmosphere affects the measurement precision of the space geodetic observations. In particular, the relatively large relative index of water vapor at radio frequencies is due to dipole nature of the water vapor molecule [*Solheim et al.*, 1999]. The distribution of water vapor is highly variable in terms of both space and time, so that the propagation delay due to water vapor is often revealed as short-scale fluctuations in space and time in space geodetic observations. In GNSS, the propagation delay effect due to the atmosphere can be estimated in an efficient way in conjunction with the position determination. On the other hand, in InSAR

the propagation delay effect can not easily separated from other signals associated with actual surface deformations and errors due to orbit inaccuracy and the digital elevation model (DEM) [*Hanssen*, 1998].

Meanwhile, the propagation delay signal due to the neutral atmosphere in space geodetic observations could be regarded as the signal representing the atmospheric condition from the perspective of meteorology [*Bevis et al.*, 1992]. The propagation delay consists of two components, the *hydrostatic* delay and the *wet* delay. According to *Saastamoinen* [1972] the hydrostatic delay can be modeled with a high accuracy using the surface pressure (details are described in Chapter 3). Therefore, the neutral atmospheric delay reflects water vapor in the troposphere. The product related to water vapor derived from GNSS observations is the precipitable water vapor (PWV), which is the height of water column if all the water in that column were precipitated as rain. Currently, GNSS receivers' network is operationally used to provide near-real-time estimates of PWV [*Foster et al.*, 2005] and to assimilate routine weather forecasts [e.g. *Nakamura et al.*, 2004]. In the past, the water vapor signal in InSAR has not been used for such a purpose and there have been few studies that focused on the water vapor signal in InSAR as a signal for meteorology. However, InSAR can detect the water vapor distribution with a high spatial resolution and thus has possibilities to be used for meteorological applications. *Pichelli et al.* [2010] mentioned that the the water vapor signal derived from InSAR would probably largely reduce uncertainties on the initial condition of the numerical weather model because of the high spatial resolution. The difficulties to use the water vapor signal in InSAR image for meteorological applications stand on: 1) the difficulty to separate the water vapor signal from other signals; 2) the characteristic feature that

the InSAR-derived phase signal is the difference of two data acquisition time, but not the absolute value of the propagation delay. If we overcome these difficulties, InSAR could be regarded as a sensor for water vapor mapping and complement GNSS observations.

1.3 The objective of this study

We work on the water vapor propagation delay in InSAR, regarding as both "noise" for crustal movement measurements and "signal" for the meteorological study. The main objectives of this study are: 1) to evaluate the ability of the high-resolution numerical weather model to correct for the neutral tropospheric delay in InSAR; 2) to validate InSAR as a water vapor sensor using the SAR data derived during a heavy rain event. Each of the studies is described in detail in Chapter 4 and Chapter 5, respectively. The contents of this thesis are summarized as follows;

Chapter 2: A brief overview of the SAR and InSAR techniques is described in this chapter. The observations from the SAR instrument is composed of contributions from many different processes. In this chapter, we also briefly present the contribution due to the ionosphere to SAR and InSAR products. In particular whose frequency of the microwave is within the L-band (ranging from 1 GHz to 2 GHz).

Chapter 3: Chapter 3 presents some background on the propagation delay in the atmosphere for space geodetic measurements. We firstly describe the brief fundamental of GNSS in Section 3.1, and then present the theory of the neutral atmospheric delay in GNSS in Section 3.2. Next we present an overview of the neutral atmospheric delay in InSAR phase signal. The reason why we describe the case of

GNSS prior to that of InSAR is that the principle of the neutral atmospheric delay in GNSS is theoretically the same as that in InSAR, and the propagation delay theory of GNSS was developed earlier than that of InSAR.

Chapter 4: This chapter presents the study addressing a question, "Are numerical weather model outputs helpful to reduce tropospheric delay signals in InSAR data?". To measure crustal deformations, the neutral atmospheric delay is the dominant error source because of its heterogeneity in space and time. Previous studies attempt to mitigate the atmospheric delay effect from interferograms using various approach such as the stacking and the numerical weather model output. Nevertheless, there are few studies that statistically assessed the effect of the delay correction. Here we will show the statistical evaluation of the effect of the delay correction using the numerical weather model and compared its efficiency with the conventional topography-correlated correction method.

Chapter 5: In Chapter 5, we will show the case study that detected the water vapor distribution signal with InSAR during the heavy rain event so-called "Seino heavy rain event" occurred on 2 September 2008. This is the first case that the distribution of water vapor during the heavy rain using InSAR. In this interferogram, we could detect the localized large-amplitude signal associated with a deep convective system. We attempt to model three-dimensional water vapor distribution based on the localized signal and performed the numerical weather simulation to clarify the mechanism of this event.

Chapter 6: The conclusion of this thesis is presented in this chapter.

Chapter 2

SAR interferometry

2.1 SAR

SAR is one of the remote sensing techniques and is a side-looking radar system that accomplished high spatial resolution in the along-track direction (also called the azimuth direction) by creating a large antenna synthetically during the signal processing. In the real aperture radar, the resolution ε is proportional to the wavelength of microwaves λ and inversely proportional to the antenna diameter d, that is,

$$\varepsilon = R\frac{\lambda}{d}, \tag{2.1}$$

where R denotes the slant range from the antenna to the target. However, using SAR technique, the resolution in the azimuth resolution could be theoretically expressed

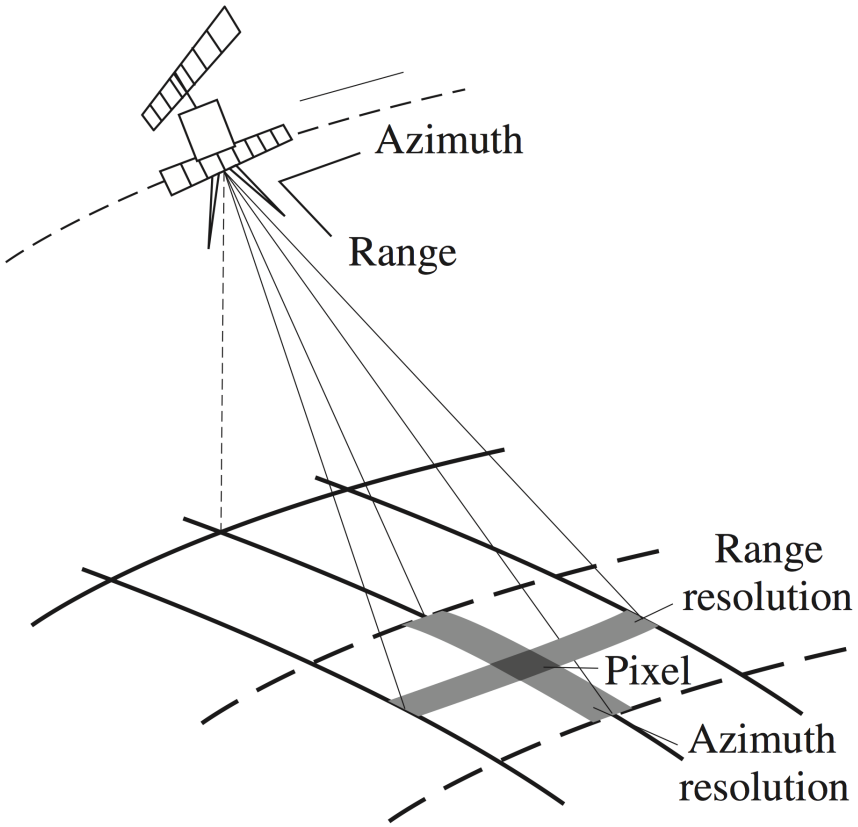

Figure 2.1: The SAR imaging geometry [*Seeber*, 2000].

as [*Furuya*, 2011],

$$\varepsilon \approx \frac{d}{2}. \tag{2.2}$$

As a consequence, the resolution in the azimuth direction is proportional to the antenna diameter and independent on the slant range R. This fact may seem to be strange, but this is the key feature of the synthetic aperture radar system. In the case of Phased Array type L-band SAR (PALSAR) aboard Advanced Land Observing Satellite (ALOS), the antenna size in the azimuth direction is about 8.9 m, and hence the azimuth resolution reaches up to 4.5 m. On the other hand, in the range direction which is perpendicular to the azimuth direction, the resolution is determined by the

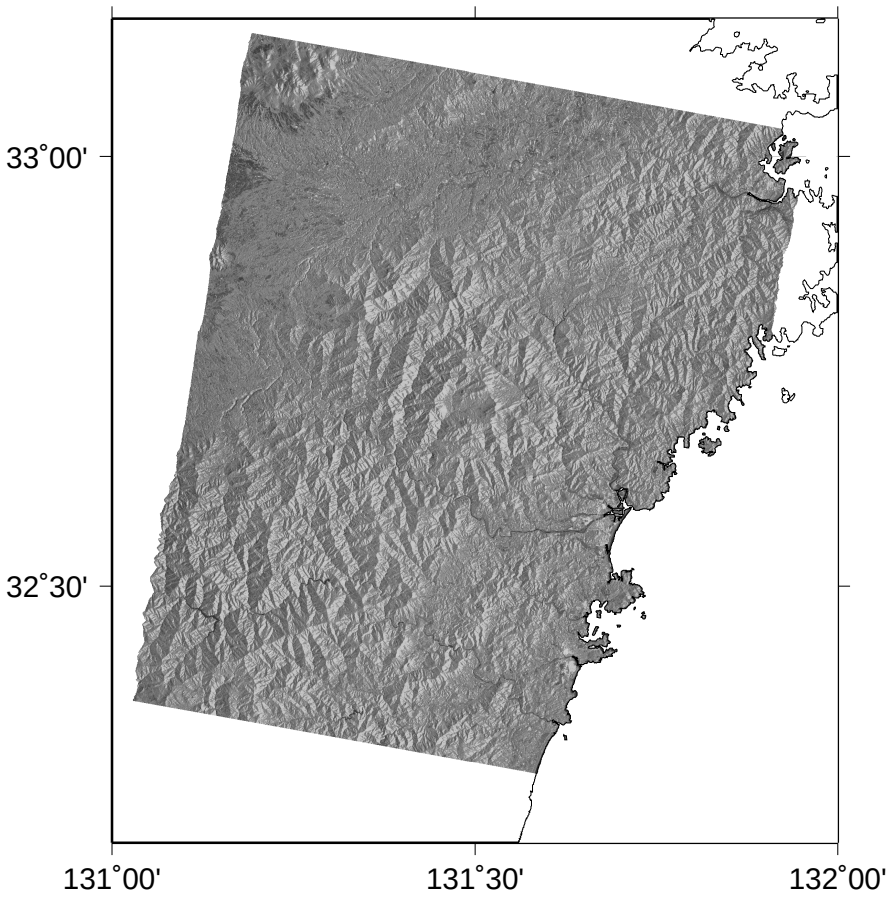

Figure 2.2: An example of SAR intensity image.

bandwidth of the transmitted pulse. The high resolution in the range direction is accomplished by the matched filter and pulse compression concepts used also for enhancing the azimuth resolution.

The basic imaging geometry is illustrated in Figure 2.1 [*Seeber*, 2000]. The SAR antenna transmits electromagnetic pulses at a rate donated by the pulse repetition frequency (PRF) towards the area to be imaged, and collects returned echoes from targets. The received signal is converted to digital data by the receiver. After that, the SAR raw data was processed with signal processing techniques mentioned

before [*Curlander and McDonough*, 1991; *Cumming and Wong*, 2005]. In this work we use SAR observations acquired from PALSAR onboard ALOS satellite. The wavelength of radiation used by PALSAR is $\lambda = 23.6$ [cm] (L-band) and the center frequency is $f = 1270$ [MHz]. The antenna beam pattern defines the width of the image swath (swath width) in the direction perpendicular to the azimuth direction, that is typically 70 km in Fine mode and 300 km in ScanSAR mode.

The typical product derived from single SAR raw data after signal processing is called Single Look Complex (SLC) image. The SLC image consists of a two-dimensional array of complex values in range and azimuth directions. This means that each element of the array, called *pixel*, has an amplitude and phase calculated from complex values through Euler's formula. Usually, the information of an amplitude derived from a SLC data is used to generate an intensity image (Figure 2.2). The SAR intensity image shows a distribution of light-dark variation. The brighter pixel indicates the area where there are intense scattering, and the darker pixel indicates the area where there are weak scattering.

The intensity image have been used for monitoring areas that are difficult to directly access such as eruptive craters [*Saepuloh et al.*, 2013], because SAR is an active imaging method and does not need any ground-based observation points. In addition, the microwave used for SAR have much longer wavelengths than optical or infrared waves, and therefore penetrates clouds easily. The use of the microwave also enable us to acquire SAR data day and night. As a consequence, these advantages provide us with temporally continuous observation chances. On the other hand, the disadvantage of SAR is its long recurrent period (e.g. 46 days for ALOS, 35 days for Envisat). However, future space SAR missions would improve the recurrent period

(e.g. 14 days for ALOS-2, 12 days for Sentinel-1).

Table 2.1: An overview of satellite SAR systems.

SAR system	Launch Year	Country	Band	Wavelength (cm)	repetition period
SEASAT	1978	USA	L	23.5	14 days
ERS-1	1991	ESA	C	5.7	35 days
JERS-1	1992	Japan	L	23.5	44 days
ERS-2	1995	ESA	C	5.7	35 days
RADARSAT-1	1995	Canada	C	5.7	24 days
ENVISAT	2002	ESA	C	5.7	35 days
ALOS	2006	Japan	L	23.5	46 days
RADARSAT-2	2007	Canada	C	5.7	24 days
TerraSAR-X	2007	DLR	X	3.1	11 days
COSMO-SkyMed	2007	Italy	X	3.1	15 days
Sentinel-1	2013 (TBD)	ESA	C	5.7	12 days
ALOS-2	2013 (TBD)	Japan	L	23.5	14 days

SAR image contains both geometric and radiometric information through the use of the microwave. The use of microwave tells us the properties of the target that are different from optical remote sensing. Major fields of SAR uses are listed below:

- topographic mapping,
- land use,
- erosion, deforestation, desertification,
- sea state, flood monitoring, ice flow,
- sedimentation, oil-shock detection and
- archeological structure.

Table 2.1 shows an overview of previous and planned satellite SAR systems. In this study, we only use ALOS/PALSAR data.

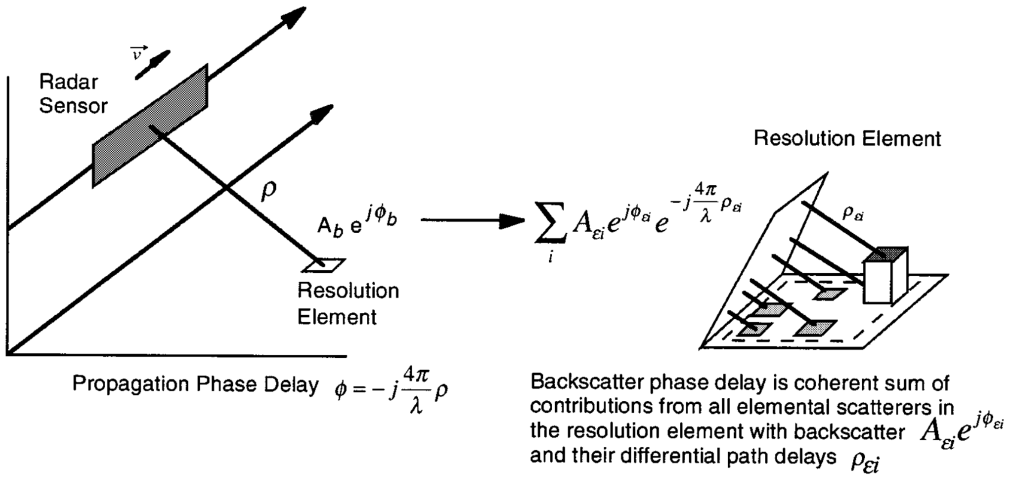

Figure 2.3: The conceptual image of scatter phase shift [*Rosen et al.*, 2000].

2.2 SAR interferometry

The SAR image contains both intensity and phase informations. Basically, the phase of a pixel ϕ includes information on the phase shift caused by scattering effect ϕ_s and the propagation phase delay from the SAR antenna to the ground target and back, ϕ_p,

$$\phi = \phi_s + \phi_p, \tag{2.3}$$

where the signal propagation delay ϕ_p is related to the distance between the SAR antenna to the ground target R,

$$\phi_p = \frac{4\pi}{\lambda} R. \tag{2.4}$$

The phase can only be measured modulo 2π. Basically, the backscatter phase shift ϕ_s is the net phase of the coherent sum of the contributions from all elemental scatterers inside the resolution element. Therefore each pixel has their individual backscatter

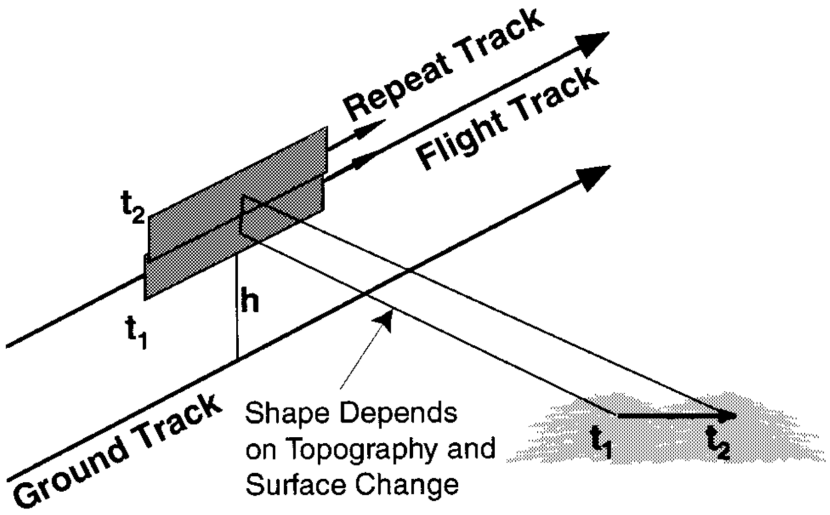

Figure 2.4: The conceptual image of the repeat-pass interferometry [*Rosen et al.*, 2000].

phases [*Rosen et al.*, 2000, Figure 2.3]. If two radar images were acquired from two nearby antenna locations, these images have elements with nearly the same backscatter phases. In the phase difference, the scattering part ϕ_s will be effectively canceled in each resolution element, if the scattering property did not vary between the two images. In consequence, the scattering part ϕ_s in Equation (2.3) will be eliminated and the phase difference $\Delta\phi$ is then,

$$\begin{aligned} \Delta\phi &= \phi_2 - \phi_1 = \phi_{p2} - \phi_{p1} \\ &= \frac{4\pi}{\lambda}(R_2 - R_1), \end{aligned} \tag{2.5}$$

where numbers of subscripts represents observation periods. Equation (2.5) indicates that the residual phase represents only the difference of distances between two observations. This is the fundamental equation of InSAR.

The two receiving antenna required for the interferometry can be arranged in

a different manner. The along-track interferometer maintains a baseline between two antenna separated along the flight track. This arrangement is used for surface motion measurements. With the single-pass interferometer, two SAR images are recorded simultaneously. This arrangement was used with the *Shuttle Radar Topography Mission* (SRTM) which used X-band and C-band SAR antennas. The SRTM produced the high-resolution DEM with the spatial resolution of approximately 90 m within 56 degrees south and the 60 degrees north. In the repeat-pass interferometry, a SAR antenna repeats its track and measures the same area after several days or months. This technique requires the precise orbit information and to pass the same track to interfere two SAR observation data. The slightly displaced imaging position causes some topographic fringe in the interferogram due to the parallax between two SAR images [*Rosen et al.*, 2000], and the orbit error causes orbital fringe in the interferogram. Orbital fringes could be regarded as the three-dimensional Young's experiment of interference [*Furuya*, 2011]. We will discuss later how to remove these fringes. The repeat-pass interferometry has been widely used to generate elevation maps and to detect surface deformations associated with earthquakes, volcanic activities and so on.

The measured phase in InSAR, ϕ_{InSAR}, contains several signals besides surface deformation and topographic fringe, that is,

$$\phi_{InSAR} = \phi_{def} + \phi_{topo} + \phi_{orbit} + \phi_{iono} + \phi_{atm} + \phi_{noise}. \tag{2.6}$$

In equation (2.6), ϕ_{def} represents the phase change due to surface deformations occurred during two SAR acquisition, ϕ_{topo} represents the topographic fringe, ϕ_{orbit}

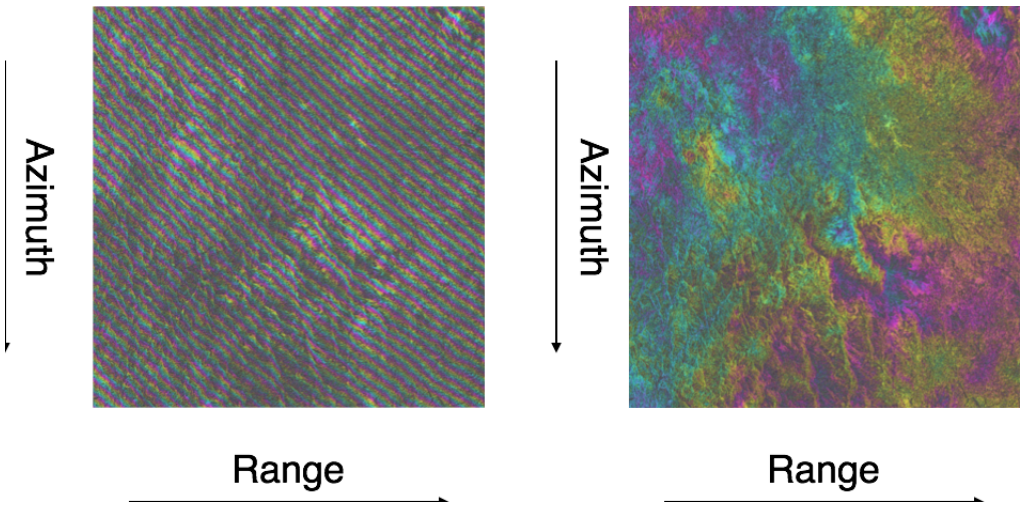

Figure 2.5: (Left) An initial interferogram at the location of Miyazaki prefecture, that has been obtained from ALOS/PALSAR data (B_{perp} = 51.8 [m]). Striped pattern in the entire interferogram are orbital fringes. (Right) A flattened interferogram. Orbital fringes are successfully removed.

represents orbital fringe, ϕ_{iono} represents the phase shift due to the ionospheric disturbance, ϕ_{atm} represents the propagation delay due to the neutral atmosphere, and ϕ_{noise} represents the noise which are temporal and spatial decorrelation due to vagitations, changes of the surface condition and so on.

In the initial interferogram, orbital fringe appears by the same mechanism as the Young's experiment, and hence could be removed using orbit data at the two SAR data acquisitions (Figure 2.5). However, when the given orbit data contain errors, those generate long-wavelength fringes in the interferogram and obscure the interpretation, especially the long-wavelength small-amplitude deformation like interseismic deformation [*Shizaei et al.*, 2011]. The conventional approach to reduce the fringe due to errors in the orbit determination is to fit a polynomial plane (usually linear or quadratic plane) and estimate the coefficients by means of the least square

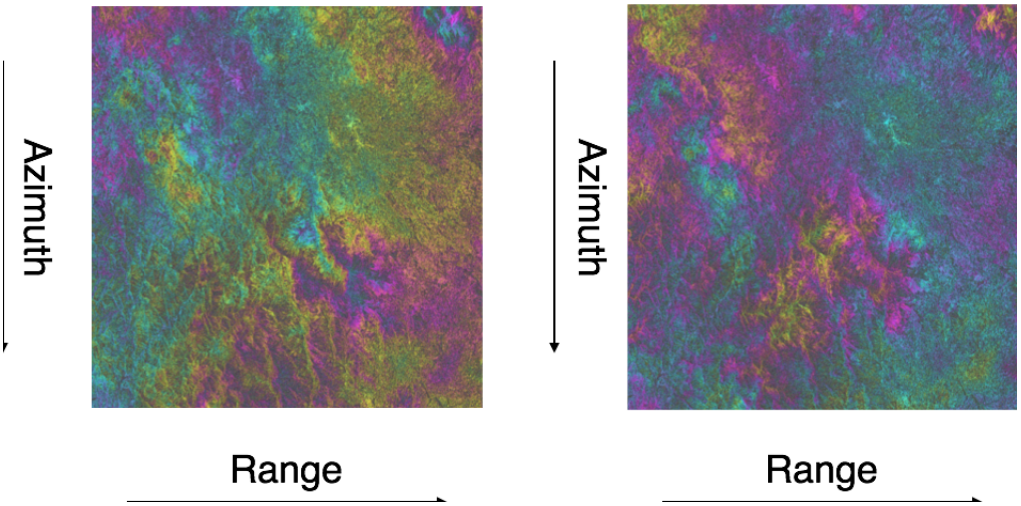

Figure 2.6: (Left) A flattened interferogram at the location of Miyazaki prefecture, that has been obtained from ALOS/PALSAR data (B_{perp} = 51.8 [m]). (Right) An interferogram after removing topographic fringe using DEM.

manner. For example, when the model quadratic plane is expressed as,

$$\phi_{orbit}^{quad} = a_1 x + a_2 y + a_3 x^2 + a_4 y^2 + a_5 xy, \tag{2.7}$$

where x and y represent pixels in the range and azimuth direction, respectively, we estimate the coefficients a_i.

The topographic fringe ϕ_{topi} originates in the difference between two slightly distant orbits and topography. The phase difference due to topography is related to the distance of two satellite orbits, a *baseline B*, especially the perpendicular component of the baseline B_{perp} (hereafter called the perpendicular baseline), that is the projection perpendicular to the slant range. This is because the separation of two orbits causes the parallax effect similar to the conventional stereoscopic approach, and an amount of the parallax effect is determined by B_{perp}. The relationship between topographic fringe and the perpendicular baseline can be expressed as [*Rosen et al.*,

2000],

$$\phi_{topo} = \frac{\lambda R \sin\theta}{2B_{\perp}}, \tag{2.8}$$

where θ denotes the incidence angle which is defined as the angle between the radar line-of-sight (LOS) and the local vertical at the target point of the surface. For monitoring and detecting surface displacements, topographic fringe should be removed. This could be achieved by simulating topographic fringe using DEM or by three-pass interferometry [*Zebker et al.*, 1997].

The ionospheric effect to the InSAR phase measurement ϕ_{iono} was mainly due to small-scale turbulence in the ionosphere, such as the traveling ionospheric disturbance (TID) and the plasma bubble [*Meyer et al.*, 2006]. The ionospheric effect to the refractivity is dispersive (as discussed in the later chapter), and hence the influence of this effect is dominant for the lower frequency L-band SAR like ALOS/PALSAR, not for C-band Envisat ASAR and X-band TerraSAR-X and CosmoSkyMed. *Gray et al.* [2000] showed the so-called *azimuth streaking effect* in the azimuth offset image and the interferogram derived from RADARSAT SAR data in polar regions. The magnitude of ionospheric disturbances is relatively small and is below 1 TECU for small-scale structures smaller than 10 km. An example of the azimuth streak is shown in Figure 2.7. *Meyer et al.* [2006] presented the relationship between the azimuth streak in the azimuth offset image and the ionospheric effect in the interferogram theoretically, that is,

$$\frac{2}{c}\Delta x = \alpha \cdot \Delta\phi_{iono} \tag{2.9}$$

where c denotes the speed of light, Δx is the azimuth shift in the azimuth offset image, $\Delta\phi_{iono}$ is the phase difference due to the ionospheric effect, and α is a system- and

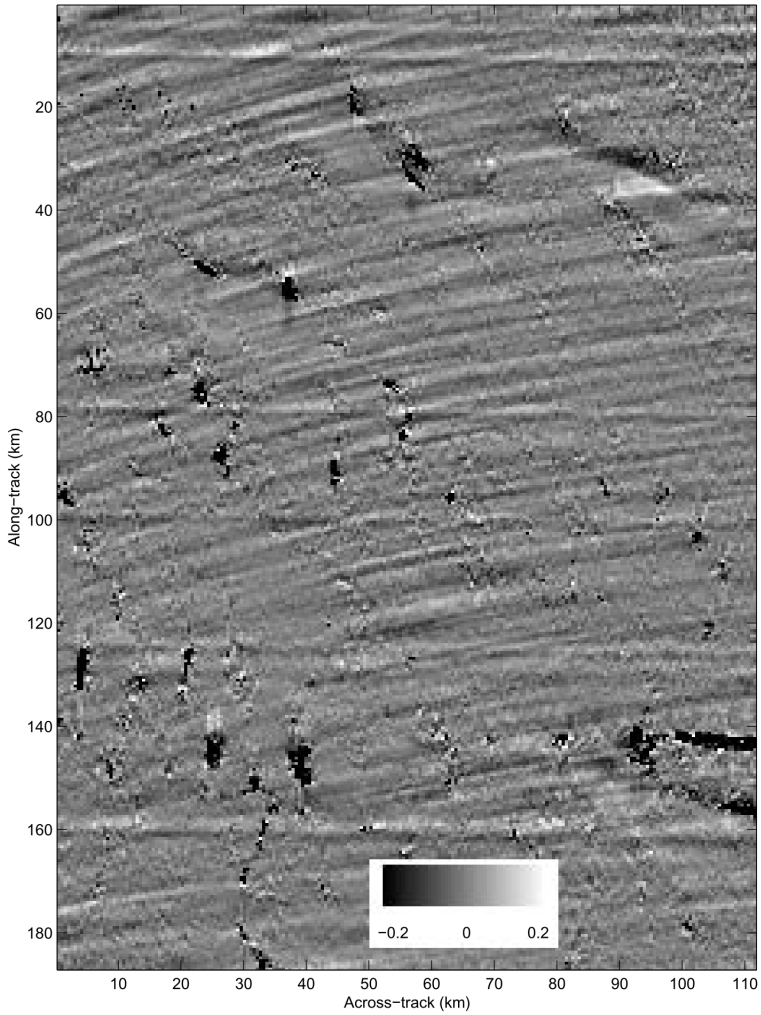

Figure 2.7: An example of the azimuth streak [*Gray et al.*, 2000].

geometry-dependent factor and should be determined with the least square manner. Using the relationship expressed in Equation (2.9), *Raucoules and Michele* [2010] attempted to correct for ionospheric disturbances in the interferogram from the azimuth offset data in the case of 2008 Sichuan earthquake derived from ALOS/PALSAR. Their results showed the effectiveness of the correction method proposed by *Meyer et al.* [2006]. Figure 2.8 shows an example of the ionospheric correction with the method proposed by *Meyer et al.* [2006]. In this case, the ionospheric effect in the

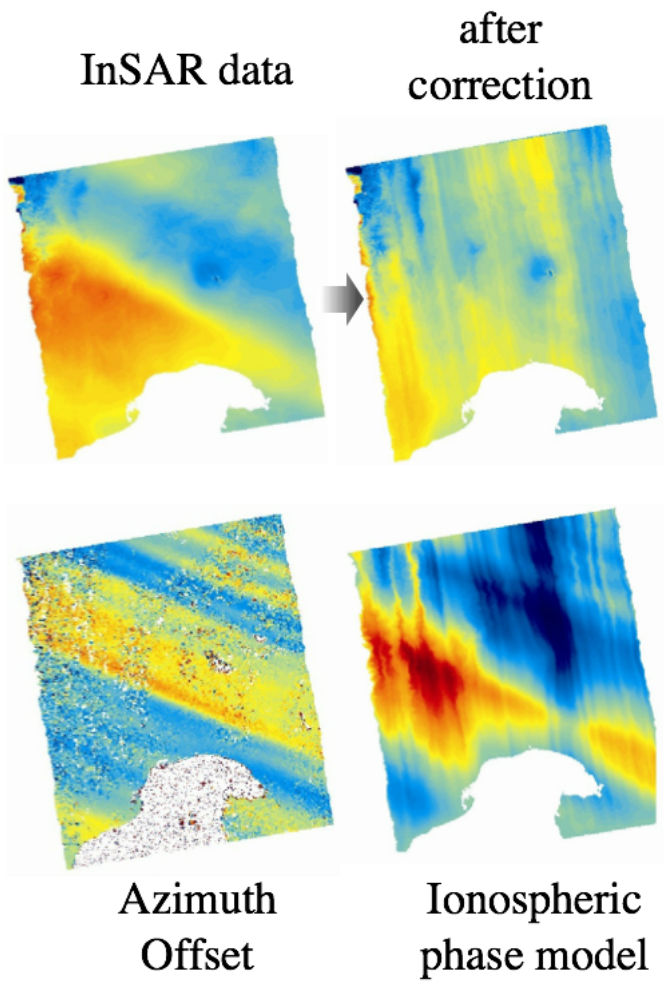

Figure 2.8: An example of the correction of the ionospheric effect. The SAR data were acquired by ALOS/PALSAR around Mt. Fuji.

interferogram is significantly reduced. However, there are no statistical approach to validate the effectiveness of this method, and the validation of this method is left for the future work.

The neutral atmospheric delay ϕ_{atm} in Equation (2.6) has roots in the spatial heterogeneity of the refractivity in the atmosphere and the in the difference of propagation delays between two SAR acquisition time [*Zebker et al.*, 1997]. Because SAR is based on the microwave with similar frequencies to GNSS, the principle of

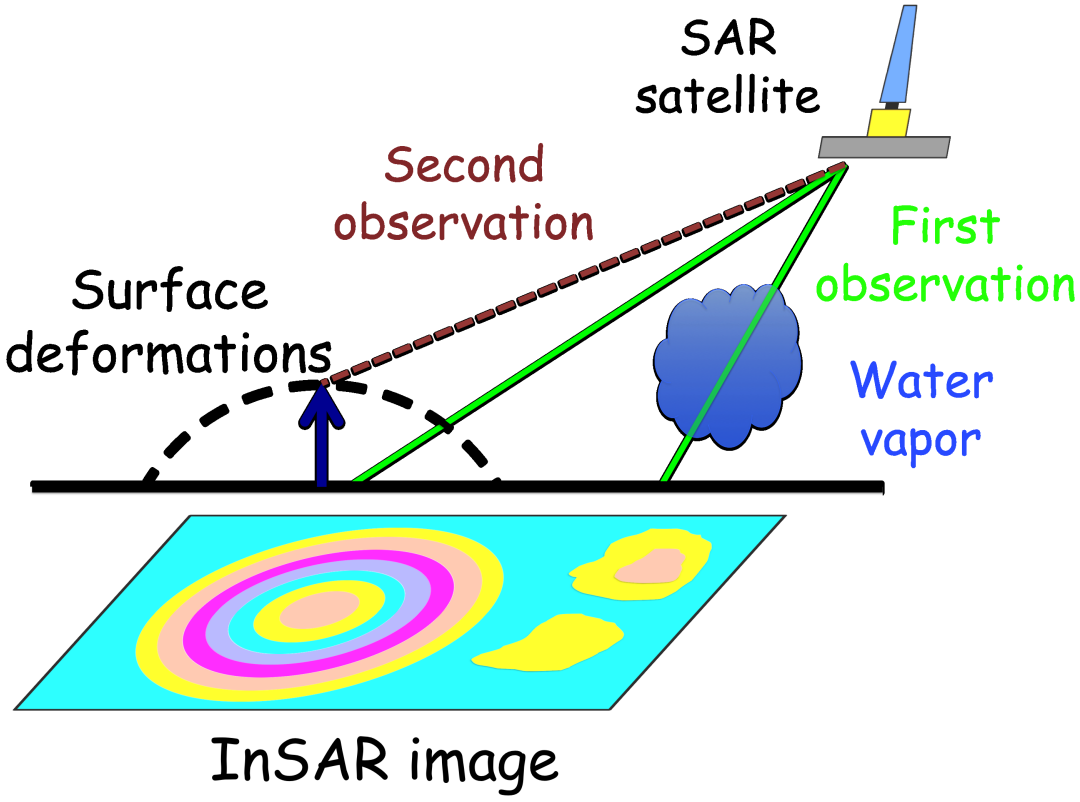

Figure 2.9: A conceptual image of detecting surface deformations in InSAR.

the propagation delay effect is the same as GNSS. In the following chapter, we will discuss the neutral atmospheric delay in InSAR in detail.

The most-used application of InSAR would be to detect spatial distribution of surface displacements. Figure 2.9 illustrates a conceptual image of detecting surface deformations in InSAR. Since *Massonnet et al.* [1993] successfully detected the broad and intricate fringe patterns associated with the seismic fault motion of the Landers M = 7.2 earthquake of 1992, many InSAR-based crustal deformation studies have been reported [e.g. *Beauducel et al.*, 2000; *Bechor and Zebker*, 2006]. The advantage of using InSAR, instead of GNSS, is to generate high-resolution deformation maps with an accuracy of centimeters to sub-centimeters and in consequence

InSAR allows us to explore the complexity of the fault geometry. Conversely, InSAR has several disadvantages such as the long recurrence period of a few tens of days (e.g. 46 days for ALOS) mentioned before, and the existence of the atmospheric propagation delay effect (both ionosphere and neutral atmosphere) with an amplitude of several centimeters to few tens of centimeters [*Zebker et al.*, 1997] (we will describe this in the next chapter.). In addition, InSAR cannot measure surface deformations with 3-D displacement vector, but only in the LOS direction. Even so, InSAR is a powerful tool to detect surface deformations and could complement GNSS observations.

Chapter 3

Neutral atmospheric delay

3.1 Introduction

In this chapter, we describe the contribution of the neutral atmosphere to InSAR and GNSS. The background materials presented here are quotes from *Bevis et al.* [1992] and *Zebker et al.* [1997] among others. In InSAR and GNSS, the primary error source for the detection of crustal deformation comes from the spatiotemporal fluctuation of water vapor in the troposphere. On the other hand, the delay effect due to water vapor could be regarded as a signal reflecting the heterogeneity of water vapor in the troposphere. Indeed, there are many studies that used the estimated atmospheric delay for meteorological applications, which is particularly the case in GNSS [e.g. *Ning et al.*, 2013]. In the following sections, we will address the issues of the atmospheric delay effect in GNSS and InSAR, respectively.

3.2 Principle of neutral atmospheric delay for space geodetic observations

For space geodetic techniques using a microwave with frequencies ranging from 300 MHz to 300 GHz such as GNSS, VLBI and SAR, the propagation delay effect due to the neutral atmosphere in the Earth is the principal error source for determining the observed location and detecting crustal deformations [*Niell, 1996*]. The propagation delay effect is caused by the difference of refractivity in the atmosphere from that in a vacuum ($n = 1$). It is difficult to accurately estimate the amount of propagation delay effect due to the neutral atmosphere, because it is independent of the frequency. In the following, we will describe the brief derivation of the equation that expresses the refractivity in the neutral atmosphere according to *Aparicio and Laroche* [2011].

The refractive index n of a propagating material for electromagnetic waves is given by Maxwell's equation,

$$n = \sqrt{\epsilon_r \mu_r} \tag{3.1}$$

where ϵ_r and μ_r denote the relative dielectric constant and the relative magnetic permeability, respectively.

The electric permittivity of the propagating material is related to microscopic properties through the Lorentz-Lorenz relationship [*Born and Wolf*, 1999],

$$\frac{\epsilon_r - 1}{\epsilon_r + 2} = \frac{4\pi}{3} \sum_i n_i \left[\alpha_i + \frac{\mu_i^2 f(\epsilon_r)}{3 k_B T} \right] \equiv \frac{\delta_\epsilon}{3}. \tag{3.2}$$

Here, n_i denotes number concentrations of substances i, α_i denotes average polarizability, μ_i denotes permanent electric dipole, f denotes a function of ϵ_r, that expresses the interaction of a dipole with the surrounding particles, k_B denotes the Boltzmann constant ($k_B = 1.3806488 \times 10^{-23}$ [J/K]), and T denotes absolute temperature [K]. The quantity f depends on the permittivity of the material, and for air f remains always very close to 1. Therefore hereafter we assume $f = 1$. Because the term $\delta_\epsilon/3$ in the right side of Equation (3.2) is small for air, we can apply the Taylor expansion for ϵ_r to Equation (3.2), yielding the linearized form of Equation (3.2),

$$\epsilon_r = 1 + \delta_\epsilon + \frac{1}{3}\delta_\epsilon^2 + ... \tag{3.3}$$

For low densities, Equation (3.2) can be reduced to the first term in Equation (3.3). Therefore we obtain the linear approximation to the electric susceptibility, ϵ_r^0,

$$\epsilon_r^0 = 1 + 4\pi \sum_i n_i \left[\alpha_i + \frac{\mu_i^2}{3k_B T} \right]. \tag{3.4}$$

On the other hand, the magnetic response to an electromagnetic wave can be expressed as similar to the expression of the electric response. The linearized expression of the magnetic response is,

$$\mu_r = 1 + 4\pi \sum_i n_i \left[\chi_i + \frac{\nu_i^2}{3k_B T} \right] \equiv 1 + \delta_\mu, \tag{3.5}$$

where χ_i denotes the molecular magnetizabilities of substances i which are generally very small and negative, and therefore most substances are diamagnetic. ν_i denotes the molecular permanent magnetic dipole of substances i.

Substituting Equations (3.4) and (3.5) into Maxwell's equation for the refractivity (3.1), the refractivity $N = 10^6(n-1)$ could be expressed as,

$$N = 10^6 \left[\frac{1}{2}(\delta_\epsilon + \delta_\mu) + \frac{1}{24}\delta_\epsilon^2 + ... \right]. \tag{3.6}$$

Here N is the dimensionless parameter which has a convenient scale of excess path (mm) per 1 km propagation [mm/km]. Therefore, the first approximation of (3.6) could be expressed as,

$$N_0 = 10^6 \frac{1}{2}(\delta_\epsilon + \delta_\mu). \tag{3.7}$$

Using Equations (3.4) and (3.5), we could obtain the general form expression of the refractivity under the low-density assumption,

$$N_0 = \rho_d \left(q_1 + \frac{q_2}{T} \right) + \rho_v \left(q_3 + \frac{q_4}{T} \right) \tag{3.8}$$

where q_1, q_2, q_3 and q_4 are constants. Most existing expressions follow similar functional forms, but expressed in terms of pressure,

$$N = \frac{P_d}{T} \left(k_1 + \frac{k_4}{T} \right) + \frac{P_v}{T} \left(k_2 + \frac{k_3}{T} \right), \tag{3.9}$$

although the term represented by the constant k_4 is neglected in all expressions cited in this section.

From the practical point of view, the coefficients in Equation (3.8) are determined from a fit to either experimental or model-generated values. Within this fit, some of the parameters are strongly correlated [*Aparicio and Laroche*, 2011]. To reduce these correlations without increasing degrees of freedom, the following ex-

pression can be chosen for the low-density behavior,

$$N_0 = \rho_d \left(a_1 + a_2 \cdot \tau\right) + \rho_v \left(a_3 + a_4 \cdot \tau\right), \tag{3.10}$$

with $\tau = 273.15/T - 1$.

Equation (3.10) represents the linear approximation of the refractivity. To derive more accurate expression, nonlinear dependencies are not entirely negligible. The expression of the refractivity with nonlinearlity is,

$$N = \left[N_0 + \frac{1}{6}10^{-6}N_0^2 + ...\right] \simeq N_0\left(1 + \frac{1}{6}10^{-6}N_0\right). \tag{3.11}$$

3.3 Neutral atmospheric delay in GNSS

GNSS is one of the space geodetic techniques that allows us to determine the precise location of the receiver with an accuracy on the order of millimeters and to monitor small surface deformations continuously in time. The NAVSTAR GPS (NAVigation System with Time and Ranging Global Positioning System) is an operational system of GNSS maintained by the United States of America, which has been used for the solution of geodetic problems since around 1985. As of November 2013, 32 satellites are in operation. Practically speaking, GPS had been the only operational GNSS system until the Russian GNSS, the Global Navigation Satellite System (GLONASS), started in operation in 2007. At present, the Chinese GNSS, BeiDou Navigation Satellite System, and the Europian GNSS, the Galileo system, are in operation besides GPS and GLONASS. In addition, the first satellite of the Japanese Quasi-Zenith Satellites System (QZSS) started in operation in 2013 and

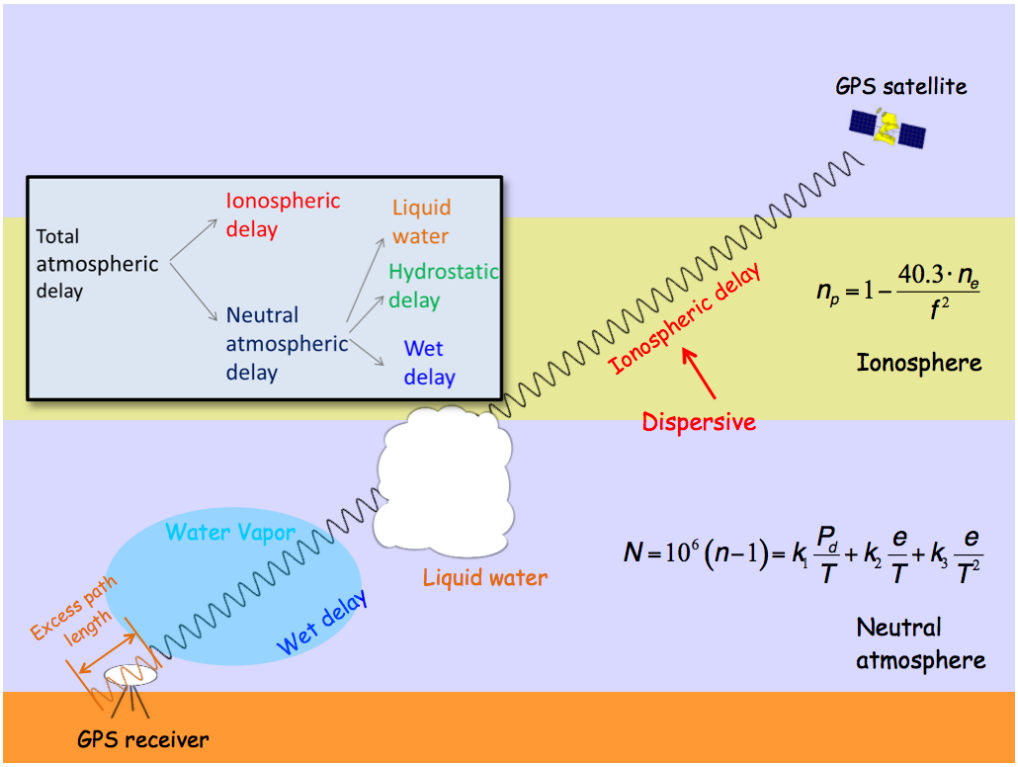

Figure 3.1: The conceptual image of atmospheric propagation delay which includes ionospheric effect and the neutral atmospheric delay.

following satellites will be launched later.

The observed GNSS carrier phase ϕ^{GNSS} consists of several components, and can be expressed as below,

$$\phi^{GNSS} = \frac{2\pi}{\lambda}\left[\rho^i + c(\Delta t^i_{satellite} - \Delta t_{receiver}) + \phi^{GNSS}_{iono} + \phi^{GNSS}_{atm} - \lambda N^i + \phi^{GNSS}_{errors}\right], \quad (3.12)$$

where ρ^i denotes the geometric distance between a GNSS receiver and the ith satellite, c denotes the speed of light ($c = 299,792,458[m/s]$), Δt denotes the clock offset of the GNSS receiver and the ith satellite, ϕ^{GNSS}_{iono} denotes the propagation delay in the ionosphere, ϕ^{GNSS}_{atm} denotes the propagation delay in the neutral atmosphere, λ denotes the wavelength of the GNSS carrier phase, N^i denotes the integer number of

cycles of phase corresponding to range to the *i*th GNSS satellite and ϕ_{errors}^{GNSS} denotes the phase shift due to other errors including the effects of orbit inaccuracies, signal multipath and receiver antenna phase center variations (PCVs). Figure 3.1 shows a conceptual image of the atmospheric delay in microwaves. In the case of the Precise Point Positioning (PPP) method that we used in this study, we use high-precision International GNSS Service (IGS) final orbit data and we assume that effects of multipath and PCVs are significantly small for estimating the zenith propagation delay due to the neutral atmosphere which we concern in this study. Therefore we can ignore the last term in Equation (3.12). The effect of the ionosphere depends on the total amount of the electron content along the signal path, called Total Electron Content (TEC), and the frequency of the carrier phase which means that the ionosphere is dispersive for the GNSS carrier phase. The refractive index in ionized gas n_{iono} can be expressed as,

$$n_{iono} = 1 - \frac{Cn_e}{f^2}, \tag{3.13}$$

where C is a constant value with $C = 40.3$, n_e denotes the electron density with the unit [number of electrons/m^3], and f denotes the frequency of the carrier phase. To integrate Equation (3.13) along the signal path, we can derive the amount of ionospheric delay,

$$\phi_{iono}^{GNSS} = -\frac{40.3}{f^2} \int_s n_e ds \tag{3.14}$$

where s represents the entire propagation path. Equation (3.14) indicates that the ionospheric delay can be estimated by using a combination of dual frequency observations. Therefore, after processing GNSS observation data by the PPP method, we can obtain precise three dimensional coordinates of the receiver's location and the

amount of the zenith propagation delay at the receiver.

In the PPP method, tropospheric delay parameter is estimated in concurrence with estimating the position of the receiver after removing other error sources because it is difficult to precisely model its parameter from other information like the ionospheric delay. This means the increase of unknown parameters for solving observation equation, and therefore many measurements are needed to perform the precise determination of these parameters.

The neutral atmosphere is a mixture of dry gases and water vapor, and water vapor is the only constituent that possesses a dipole moment contribution to its refractivity [*Bevis et al.*, 1992]. From this fact, we can treat the dipole component of the water vapor refractivity separately from the nondipole components of the refractivity of all components in the atmosphere. These two components are referred to as the "*wet*" delay and "*hydrostatic*" delay (often referred to as the "*dry*" delay), respectively, and these components are expressed in the zenith direction as,

$$ZTD = ZHD + ZWD, \tag{3.15}$$

where ZTD represents the zenith total delay, ZHD represents the zenith hydrostatic delay and ZWD represents the zenith wet delay. Here we will introduce these two components from the equation of atmospheric refractivity (3.9) which assumes $k_4 = 0$. Approximating the inverse compressibility factors Z_d^{-1} and Z_w^{-1} as 1, the equation of the atmospheric refractivity is,

$$N = k_1 \frac{P_d}{T} + k_2 \frac{P_v}{T} + k_3 \frac{P_v}{T^2}. \tag{3.16}$$

The equation of state for an ideal gas is,

$$P_i = \rho_i R_i T, \tag{3.17}$$

where ρ denotes the density, R denotes the specific gas constant and the subscript i represents gas species. Substituting Equation (3.17) into Equation (3.16) gives,

$$N = k_1 \rho R_d + k_2^{'} \frac{P_v}{T} + k_3 \frac{P_v}{T^2} \tag{3.18}$$

and the constant parameter $k_2^{'}$ appeared in the above equation is,

$$k_2^{'} = k_2 - k_1 \frac{m_v}{m_d} \tag{3.19}$$

where m_v and m_d represent the molecular weight of water vapor and dry air, respectively. The first term in the right side of the equation represents the hydrostatic delay and the combination of latter two terms represents the wet delay.

3.3.1 Zenith hydrostatic delay

To separate two components from the total neutral atmospheric delay, we can use the theoretical model of the zenith hydrostatic delay presented by *Saastamoinen* [1972]. *Saastamoinen* [1972] presented the zenith hydrostatic delay model that depends only on surface pressure (hereafter we will call this model as Saastamoinen model). We will explain the derivation of Saastamoinen model below.

The zenith hydrostatic delay is defined as the integral over the hydrostatic

refractivity,

$$ZHD = 10^{-6} \int_{h_0}^{\infty} N_h(h) dh, \tag{3.20}$$

where h_0 denotes height of the surface above the mean sea level (msl) [m] and N_h denotes the hydrostatic refractivity which is expressed by the first term of Equation (3.18). With the equation of the state for an ideal gas written in Equation (3.17), the ZHD can be written as,

$$ZHD = 10^{-6} k_1 R_d \int_{h_0}^{\infty} \rho_a(h) dh \tag{3.21}$$

where $\rho_a = \rho_d + \rho_v$. Under the condition of hydrostatic equilibrium, we can use the hydrostatic equation,

$$\frac{dP}{dh} = -\rho_a(h) g(h), \tag{3.22}$$

where $g(h)$ denotes the gravitational acceleration as a function of height h. Integrating Equation (3.22) yields,

$$\int_{P_0}^{0} dP = -\int_{h_0}^{\infty} \rho_a(h) g(h) dh = -P_0 \tag{3.23}$$

where P_0 represents the surface air pressure. Here we will introduce the mean gravity g_m assuming that the gravitation is constant with height and equal to a mean value,

$$g_m \doteq \frac{\int_{h_0}^{\infty} \rho_a(h) g(h) dh}{\int_{h_0}^{\infty} \rho_a(h) dh}. \tag{3.24}$$

Using Equations (3.21), (3.22) and (3.23), we obtain

$$ZHD = 10^{-6} k_1 \frac{R_d}{g_m} P_0. \tag{3.25}$$

Since the mean gravity depends on height and latitude under an assumption by *Saastamoinen* [1972], the mean gravity can be given as [*Davis et al.*, 1985],

$$g_m \doteq g_m^0 \cdot f(\phi, h) \tag{3.26}$$

where g_m^0 denotes the acceleration due to gravity at the center of mass of the vertical column $[m/s^2]$ and ϕ denotes geodetic latitude [rad]. The function $f(\phi, h)$ is expressed as,

$$f(\phi, h) = 1 - 0.00266\cos(2\phi) - 0.00000028h. \tag{3.27}$$

Using Equations (3.25), (3.26) and (3.27), we obtain the equation of Saastamoinen model,

$$ZHD_{saastamoinen} = 10^{-6} k_1 \frac{R_d P_0}{g_m^0(1 - 0.00266\cos(2\phi) - 0.00000028h)}. \tag{3.28}$$

Equation (3.28) has three parameters, surface pressure P_0, geodetic latitude ϕ, and height h. For example in *Davis et al.* [1985], $k_1 = 77.604$ $[K/mbar]$, $R_d = 0.28705376$ $[m^2/s^2K]$ and $g_m^0 = 9.784$ $[m/s^2]$ were used for the calculation of Equation (3.28).

3.3.2 Integrated water vapor

In this section we will show the derivation of Integrated Water Vapor (IWV) from ZWD, following *Bevis et al.* [1992]. IWV is linearly related to Integrated Precipitable Water Vapor (IPWV), namely,

$$IWV = \rho_w \cdot IPWV \tag{3.29}$$

with $\rho_w = 1000$ [kg / m^{-3}]. The ZWD is defined as,

$$ZWD = 10^{-6} \int_{h_0}^{\infty} N_w(h) dh \tag{3.30}$$

in which N_w is a combination of the second and third terms in the right side of Equation (3.16),

$$N_w = k_2^{'} \frac{P_v}{T} + k_3 \frac{P_v}{T^2}. \tag{3.31}$$

Here we introduce the weighted mean temperature of the atmosphere T_m, following *Davis et al.* [1985],

$$T_m = \frac{\int_{h_0}^{\infty} \frac{P_v}{T} dh}{\int_{h_0}^{\infty} \frac{P_v}{T^2} dh}. \tag{3.32}$$

With Equations (3.31) and (3.32), Equation (3.30) could be modified as,

$$ZWD = 10^{-6} (k_2^{'} + \frac{k_3}{T_m}) \int_{h_0}^{\infty} \frac{P_v}{T} dh. \tag{3.33}$$

Using the equation of state for an ideal gas, we have,

$$\int_{h_0}^{\infty} \frac{P_v}{T} dh = R_v \int_{h_0}^{\infty} \rho_v dh, \tag{3.34}$$

and IPWV is defined as,

$$IPWV = \frac{IWV}{\rho_w} = \frac{1}{\rho_w} \int_{h_0}^{\infty} \rho_v dh. \tag{3.35}$$

Therefore, Equation (3.33) can be written as,

$$ZWD = 10^{-6}(k_2^{'} + \frac{k_3}{T_m}) R_v \rho_w \int_{h_0}^{\infty} \rho_v dh = \Pi \cdot IPWV \tag{3.36}$$

with

$$\Pi = 10^{-6}(k_2^{'} + \frac{k_3}{T_m}) R_v \rho_w. \tag{3.37}$$

The quantity Π is dimensionless, Π equals to 6.5 on the average, but varies approximately ranging from 6 to 7. In a practical sense, it is difficult to determine T_m from observation data because of poor observational network of upper air. Therefore, an empirical formula for the weighted mean temperature as function of the surface temperature is given by *Bevis et al.* [1992], $T_m \approx 55.8 + 0.77 T_s$, with which Π can be determined to about 2 % accuracy.

3.3.3 Mapping functions

To derive an amount of propagation delay along paths, ZTD has to be projected in the slant direction with a mapping function. The mapping function $m(e)$

relates the vertical and slant delays and is defined as the ratio of the delay through the atmosphere at geometric elevation angle e, to the delay in the zenith direction. Additionally, there are separate mapping functions for the hydrostatic and water vapor components of the atmosphere, m_h and m_w, respectively. The total delay $\Delta L(e)$ for a path with an elevation angle e can be computed from ZHD and ZWD through,

$$\Delta L(e) = ZHD \cdot m_h(e) + ZWD \cdot m_w(e). \tag{3.38}$$

The simplest mapping function assumes a planar atmosphere and would be given by $1/\sin(e)$. The general form adopted for the mapping functions is the continued fraction with three coefficients a, b and c [*Niell*, 1996],

$$m(e) = \cfrac{1 + \cfrac{a}{1 + \cfrac{b}{1 + c}}}{\sin(e) + \cfrac{a}{\sin(e) + \cfrac{b}{\sin(e) + c}}}. \tag{3.39}$$

To determine three coefficients$a$, b and c, current mapping functions use either surface meteorological measurements and site location [*Davis et al.*, 1985; *Niell*, 1996; *Niell*, 2001 (IMF); *Boehm et al.*, 2006a (VMF1); *Boehm et al.*, 2006b (GMF)]. *Niell* [1996] proposed a mapping function that only needs site location and time of year (hereafter referred to as NMF). Other mapping functions cited before are based on numerical weather model outputs, and hence providing more precise coefficients [*Tesmer et al.*, 2007].

3.3.4 Delay effect due to hydrometeors

The existence of rain droplets, cloud water, snow and so on also affects the refractivity of the atmosphere [*Solheim et al.*, 1999]. In meteorology, any water particles in the atmosphere that exist in the liquid and solid phases are called *hydrometeors*. Hydrometeors also have their own permittivity as does water vapor, and hence could influence the microwave propagation. For nongaseous particles (< 1 mm for L-band), the Clausius-Mossotti equation for refractivity could be used [*Solheim et al.*, 2000],

$$(n-1)\times 10^6 = N = 1.5\times \frac{M}{\rho}\left[\frac{\varepsilon-1}{\varepsilon+2}\right], \tag{3.40}$$

where M is the mass content of the particles per unit of air volume in g m^{-3}, ρ denotes the density of the particles (both in the same units of mass per unit volume), ε denotes the permittivity of the particles.

For liquid water like rain droplets and cloud water, the permittivity is a weak function of temperature and usually the variation of temperature in the atmosphere is within the range between -15°C and 20°C. In this assumption, the permittivity for liquid water varies from about 92 to 74. Therefore, *Sloheim et al.* [1999] suggests the following approximated expression as,

$$N_{liquid} = \frac{3}{2}\frac{M_l}{\rho_l}\left[\frac{\varepsilon_l-1}{\varepsilon_l+2}\right] \approx 1.45 M_l \tag{3.41}$$

where M_l is the mass content of liquid water in g m^{-3}, ρ_l is the density of water (~0.001 g m^{-3}), and ε_l is the permittivity of water.

For solid water like snow and ice, the refractivity of solid water can be ex-

pressed in the same manner as in the case of liquid water [*Hufford*, 1991]. The permittivity of solid water can be given as $\varepsilon_{ice} = 3.185$ [*Mätzler*, 1996]. Using these results, *Brenot et al.* [2006] proposed the following approximate expression for the refractivity of solid water as,

$$N_{ice} = \frac{3}{2}\frac{M_{ice}}{\rho_{ice}}\left[\frac{\varepsilon_{ice}-1}{\varepsilon_{ice}+2}\right] \approx 0.69 M_{ice} \tag{3.42}$$

where M_{ice} is the mass content of solid water in g m^{-3}, ρ_{ice} is the density of ice (~0.000916 g m^{-3}).

3.4 Neutral atmospheric delay in InSAR

The phase of SAR microwaves contains several contributions such as orbital separation, topographic phase, ionospheric effect, delays due to the neutral atmosphere and noise (Equation 2.6). The principle of atmospheric delay effect in SAR is similar to that in GNSS because they use frequency bands of microwave ranging from 300 MHz to 300 GHz, and usually these pulse propagate through the atmosphere. For geoscientists using InSAR, the propagation delay effect often becomes a problem to detect crustal deformations due to the spatial and temporal heterogeneity of water vapor distribution [*Zebker et al.*, 1997]. Unlike GNSS, the hydrostatic delay seldom become a problem because its spatial variation is very small. Therefore the delay effect due to water vapor becomes the major error source in InSAR applications. However, as we will show later, the delay effect due to water vapor in InSAR is the integral of water vapor along the propagating path and could be regarded as a signal of water vapor at the moment of SAR acquisition time. For this reason, we

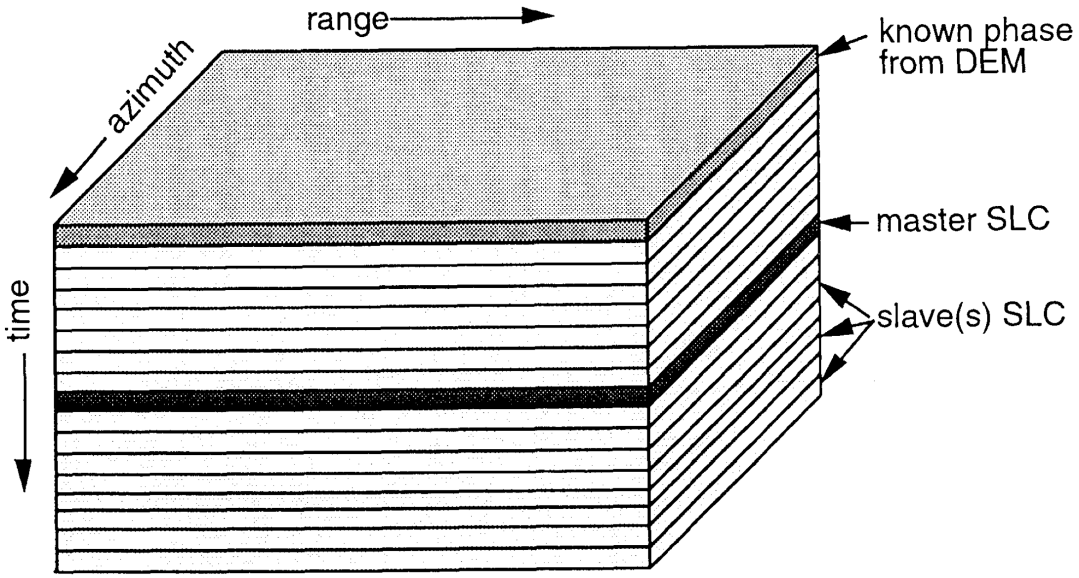

Figure 3.2: Diagram illustrating a stack of SLC SAR images [*Sandwell and Sichoix*, 2000]. Firstly slave images are co-registered to the master image. Then all SLCs are stacked in three dimensions, range, azimuth and time.

could use InSAR as a high-resolution sensor of the water vapor distribution.

In InSAR, the neutral atmospheric delay could be divided into the stratified component and turbulent component [*Hanssen*, 2001]. The stratified delay is caused by mainly the difference of horizontally-averaged profiles of the refractivity between two SAR acquisition times, and thus leads to a large phase delay correlated to the elevation [*Doin et al.*, 2009]. On the other hand, water vapor varies both vertically and horizontally over shorter distances than the dry air pressure and temperature. This characteristic causes delay signals in random pattern in the interferogram, and thus the delay due to water vapor is not correlated with elevation. Consequently the turbulent component is mostly attributed to water vapor heterogeneity.

Numerous studies have attempted to mitigate the neutral atmospheric delay for InSAR. One type of approach is to take advantage of spatiotemporal random

property of the water vapor distribution. This approach uses multiple SAR data for stacking many independent data [*Sandwell and Sichoix*, 2000; *Furuya et al.*, 2007; Figure 2.2], applying temporal low-pass filtering in time series analysis [*Ferretti et al.*, 2001; *Berardino et al.*, 2002]. These approaches can effectively mitigate the neutral atmospheric delay on the observed phase, especially the turbulent delay, but require a large number of SAR data (empirically at least 10 SLCs). Another approach to mitigate the neutral atmospheric delay from interferograms is to model the atmospheric state at the moment of the SAR observation using numerical weather models [e.g. *Wadge et al.*, 2002; *Foster et al.*, 2006, 2013]. Although the numerical weather simulation require the high computational cost, recent development of computer performances allows us to perform numerical weather simulations with horizontal resolutions of few kilometers on personal computers. In recent days, *Foster et al.* [2013] attempted to mitigate the neutral atmospheric delay using the non hydrostatic model, MM5 model, with assimilating local observation data in addition to GPS, GOCE, MODIS data. They concluded that this approach was unable to effectively mitigate the atmospheric delay for InSAR. But they also conclude that it is possible to improve the performance of weather modeling to add more spatially dense meteorological data.

The propagation delay signal due to water vapor in InSAR could be regarded as the signal detecting the spatial distribution of water vapor with high resolution. *Hanssen et al.* [1999] showed a coincidence of the location and shape between the water vapor signal in the interferogram and the precipitation area detected by the weather radar echo (Figure 3.3). *Mateus et al.* [2013] discussed in their article that the standard deviation of the PWV map obtained from ENVISAT after spatial filter-

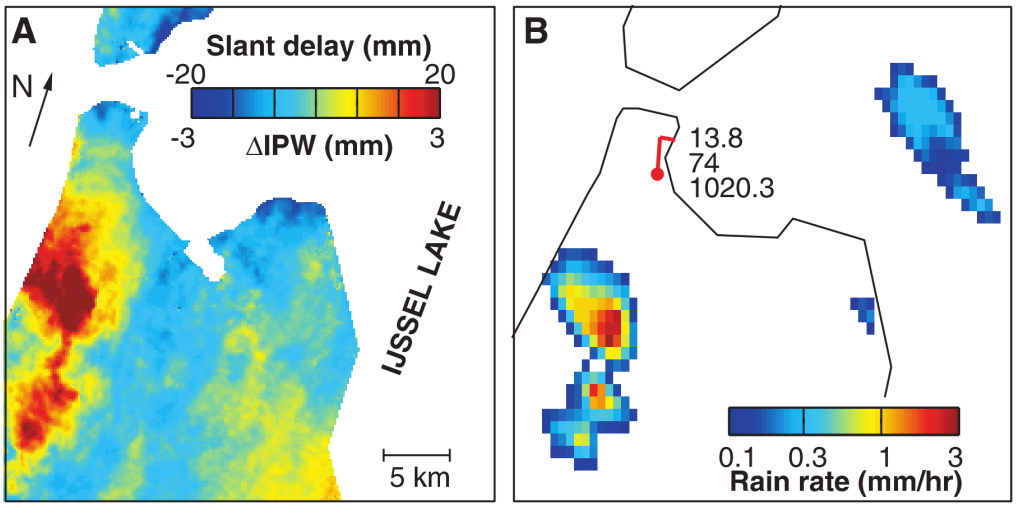

Figure 3.3: (A) The interferogram derived from ERS-1 and ERS-2 satellites operating in a one-day interval mode. (B) The weather radar rain rate at the moment of the ERS-1 data acquisition. [*Hanssen et al.*, 1999].

ing is 0.15 mm. And they mentioned that using multiple SAR satellites and different tracks would give information about the temporal evolution of the PWV spatial distribution with a sampling interval of a few days, increasing the quality of precipitation forecasting applications. As mentioned before, the neutral atmospheric delay, especially the turbulent component, in InSAR is the wet delay, so that it can be converted to the PWV using the relationship in Equations (3.36) and (3.37). According to *Mateus et al.* [2013], the expression is given by,

$$\Delta PWV^{SAR} = \Pi \cdot \frac{\lambda}{4 \cdot \pi} \cdot \phi_{atm} \cos\theta \tag{3.43}$$

where ΔPWV^{SAR} represents the PWV difference between acquisition times of master and slave images, and θ represents the incidence angle.

Chapter 4

Are numerical weather model outputs helpful to reduce tropospheric delay signals in InSAR data?

Paper was published in Journal of Geodesy

Kinoshita, Y., M. Furuya, T. Hobiger and R. Ichikawa, 2013: Are numerical weather model outputs helpful to reduce tropospheric delay signals in InSAR data?, *J. Geodesy*, 87(3), 267-277, doi:10.1007/s00190-012-0596-x.

4.1 Introduction

InSAR allows us to measure surface displacements from the phase differences at two acquisition dates after correcting for orbital contribution and surface topography. Ever since the detection reports of the co-seismic deformation due to the 1992 Landers earthquake [*Massonnet et al.*, 1993] and the glacier movements at Antarctica [*Goldstein et al.*, 1993], InSAR has been applied to a variety of phenomena such as volcano deformation, ground subsidence due to water pumping, strain accumulation around plate boundaries, and post-seismic deformation [e.g., *Massonnet and Feigl*, 1998; *Bürgmann et al.*, 2000; *Hanssen*, 2001; *Simons and Rosen*, 2009; *Furuya*, 2011]. However, InSAR cannot detect every small-amplitude signal due to the presence of errors. In particular, microwave propagation delays caused by the troposphere can mask small-amplitude deformation signals with spatial scales longer than ~10 km.

Microwave propagation delays consist of those originated in the ionosphere and the troposphere, the latter of which further consists of those due to water vapor, dry air and liquid water content [e.g. *Thayer*, 1974; *Wadge et al.*, 2010]. Hydrostatic delay and wet delay can be computed from pressure, temperature, and water vapor distribution data using empirical relations [e.g., *Hanssen*, 2001]. As for the troposphere, the magnitude of the hydrostatic delay is greater than that of the wet delay which amounts to ~20 % at maximum. For the InSAR-based deformation measurements, however, the difference between the total delays at two acquisition epochs is observed, and the effect of wet delay becomes larger, because the hydrostatic delay is largely dependent upon surface air pressure that is nearly constant over time, and

will tend to cancel out at two different epochs [*Zebker et al.*, 1997]; in mountainous areas, however, hydrostatic delays could become significant [*Elliott et al.*, 2008]. While the wet delay is smaller in terms of its amplitude, water vapor distribution is highly variable in both space and time, and its characteristic spatial scale overlaps with that of crustal deformation. The wet delay, therefore, can appear as an artifact of a crustal deformation signal.

To isolate small-amplitude crustal deformation signals from the interferogram, several approaches have been developed to correct for, or at the least reduce the tropospheric delays. In the stacking approach, advantage is taken from the spatio-temporal characteristics of a random troposphere and underlying persistent crustal deformation. Thus, one can sum up a large number of interferograms to reduce tropospheric effects and to detect crustal deformation signals [e.g., *Fujiwara et al.*, 1998; *Furuya et al.*, 2007]. The stacking approach, however, is valid mainly for the detection of secularly steady deformation signals. Meanwhile, we often encounter that phase is highly correlated with the regional topography even after the subtraction of topographic phases [e.g. *Elliot et al.*, 2008; *Fournier et al.*, 2011]. Those phases can be interpreted as the differences in the water vapor distribution over rugged terrain between the two epochs, and are also called "stratified" delay. Taking advantage of the high-resolution DEM, we perform a simple linear or quadratic regression analysis to model and subtract the topography-correlated phases [e.g., *Fujiwara et al.*, 1999]. *Lin et al.* [2010] proposed a scale-dependence in the topography-correlated signals, decomposed the DEM into several spectral components, and performed the similar regression analysis at each spectral component. In the time series analysis techniques such as the Permanent (Persistent) Scatterer [*Ferreti et al.*, 2000; *Hooper*

et al., 2004] and the Small Baseline Subset [*Berardino et al.*, 2002], the tropospheric phases which are random in time are reduced, by applying a low-pass filter along the temporal axis since they will behave temporally random. *Doin et al.* [2009] emphasized the tropospheric delay corrections prior to a stacking or a time-series analysis in order to eliminate biases in long-term strain rate estimates. The calibration-type approaches employ the other independent data to correct for the tropospheric signals. *Onn and Zebker* [2006] proposed an approach to exploit the zenith wet delay data derived from a regional GPS network. *Li et al.* [2005, 2006] employed MERIS, MODIS and GPS water vapor data to estimate and reduce the tropospheric signals in the interferogram. The problem with using GPS is their sparse spatial distribution. Also, MERIS and MODIS data are not always available at the time of the SAR data acquisitions.

Another approach is to compute tropospheric delays, using the output data from a numerical weather model (NWM), and subtract them from the interferogram [e.g. *Shimada*, 1999; *Otsuka et al.*, 2002; *Wadge et al.*, 2002; *Foster et al.*, 2006; *Ozawa and Shimizu*, 2010; *Jolivet et al.*, 2011]. *Shimada* [1999] and *Ozawa and Shimizu* [2010] used a 1.25-degree-mesh Global Analysis (GANAL) model and 10-km-mesh Meso Scale Model (MSM) of Japan Meteorological Agency (JMA), respectively, and concluded that they were ”effective” in reducing tropospheric effects. A similar approach was undertaken by *Jolivet et al.* [2011], who employed the 75-km-mesh ERA-Interim model from European Center for Medium-Range Weather Forecast. However, even in the recent JMA/MSM data, the spatial resolution of operational analysis is 10 km, which is orders-of-magnitude coarser than actual interferograms and evidently unable to reproduce the finer-scale tropospheric signals

that are not correlated with the topography.

Moreover, those operational meteorological data were computed at several fixed epochs in a day, which are usually different from the acquisition times of SAR data by more than an hour. Those operational analysis data are used directly or temporally interpolated to derive the data at the time of the data acquisition. Other studies therefore performed their own NWM computation, using even higher resolution model [e.g., *Otsuka et al.*, 2002; *Wadge et al.*, 2002, 2010; *Foster et al.*, 2006; *Puysségur et al.*, 2007]. *Wadge et al.* [2010] tried to perform the tropospheric delay correction, using a 0.3 km-resolution NWM, but concluded that model results were still inaccurate due to the coarse representation of initial conditions.

The purpose of this paper is to compare the performance of three approaches of tropospheric delay correction, two of which are based on the NWM data, using 54 interferograms formed from 26 acquisition dates in Hokkaido, Japan (Figure 4.1). The first approach is a simple DEM-based linear regression, and the second approach is based on the operational NWM output. While *Shimada* [1999] and *Ozawa and Shimizu* [2010] tested this approach around Mt. Fuji area, Japan, we examine the MSM-based approach at other mountainous areas, where the elevation differences are highly variable from 100 m to 2300 m. In the third approach, we use a state-of-the-art high-resolution non-hydrostatic numerical weather forecasting model, Weather Research and Forecasting (WRF) model [*Skamarock et al.*, 2008], and compute the tropospheric delays at the radar acquisition time with spatial resolution of 1 km. In the second and third approach, we take advantage of the Kashima Ray-Tracing Tool [KARAT, *Hobiger et al.*, 2008] so that we can more realistically perform the computation of tropospheric delays; see *Hobiger et al.* [2010] for the comparison of

ray-tracing approach with the conventional mapping approach. In this study, we do not intend to show the best performance of any approach but to compare and discuss the performance and limitation of the present state-of-the-art approaches.

While global analysis model outputs are shown to be useful to reduce long-wavelength tropospheric signals [e.g., *Doin et al.*, 2009; *Jolivet et al.*, 2011], we focus our attention to the delays with shorter wavelengths. This is partly because both orbit errors and ionosphere can generate long-wavelength noises, which we remove by polynomial fitting in the following analyses, and partly because we can examine the impact of higher-resolution NWM outputs.

4.2 InSAR and Tropospheric delay reduction

4.2.1 Microwave propagation delay

The microwave propagation delay L_e from the surface to the satellite is expressed as the difference of the actual propagation length in the atmosphere from that in the vacuum, namely,

$$L_e = \int_{atm} (n(\mathbf{r}) - 1) ds + \int_{atm} ds - \int_{vac} ds, \tag{4.1}$$

where n is refractive index at position $\mathbf{r}$, and the integration is performed along the propagation path s. The first term represents the electromagnetic delay and the second and third term represents the effect of ray-bending (Figure 4.2). The refractivity of the neutral atmosphere N can be expressed using Equation (3.16) [e.g. *Thayer*, 1974; *Hanssen*, 2001; *Puysségur et al.*, 2007]. We derived these three

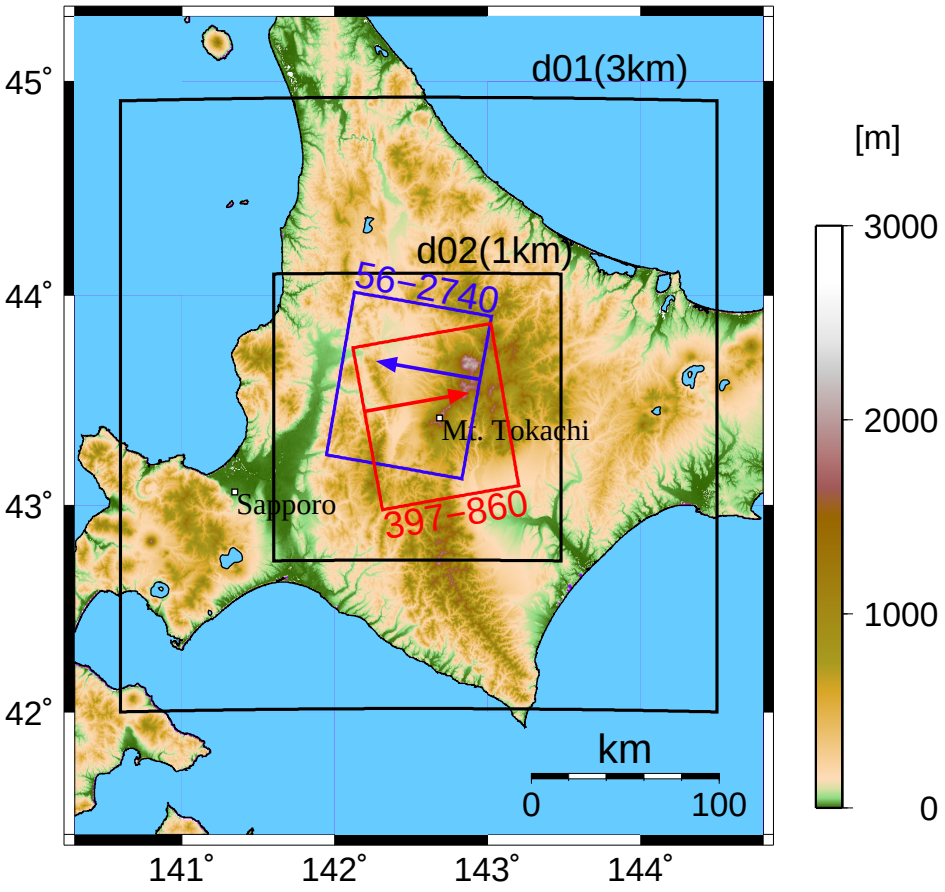

Figure 4.1: Location of the study area. Red and blue rectangle represents the ascending and descending tracks, respectively. Red and blue vectors represent the radar line-of-sight direction. Two black rectangles represent domain 1 (3 km grid-spacing) and domain 2 (1 km grid-spacing) of WRF respectively.

parameters from MSM and WRF. In this study we set the three constants according to *Bevis et al.* [1994], i.e., $k_1 = 77.604(K\ hPa^{-1})$, $k_2 = 70.4(K\ hPa^{-1})$, and $k_3 = 373.900(K^2\ hPa^{-1})$, respectively. Thus the three dimensional refractivity field at the time of SAR acquisition is obtained from Equation (3.16). Finally, instead of using a mapping function approach, total atmospheric path delay at each pixel is calculated with KARAT based on ray tracing method [*Hobiger et al.*, 2010].

In many previous studies, tropospheric delay has been considered as the sum

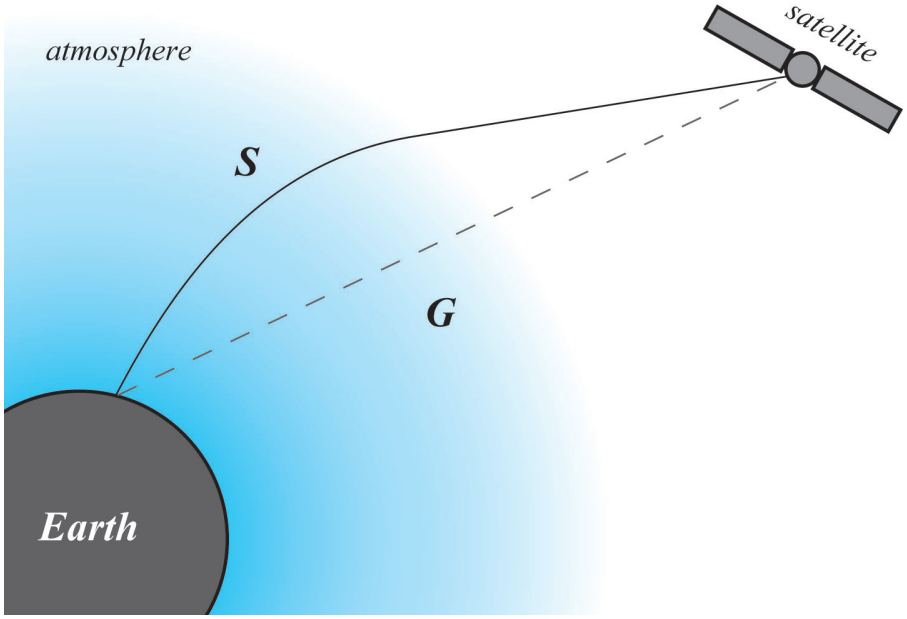

Figure 4.2: The conceptual image of the propagation delay effect on microwaves.

of two components, hydrostatic delay and wet delay, and they have been estimated separately. The hydrostatic delay was modeled as a function of latitude, height and surface pressure [e.g. *Elgered*, 1993]. However, it is derived on the assumption of a hydrostatic approximation in the pressure profile, and hence the zenith total delay is first computed. The zenith total delay is then converted to the slant range delay with a use of a mapping function. Although this approach provides us with a good approximation of the actual delay, we adopt a more rigorous ray-tracing approach without using a mapping function (see *Hobiger et al.* [2010] for details).

4.2.2 InSAR processing

Interferograms were generated from the ALOS/PALSAR level 1.0 data with the use of Gamma SAR processor. Table 4.1 is a list of the SAR data pairs used in this paper. Figure 4.1 shows our study area in the middle of Hokkaido, Japan.

With the exception of the very localized signal at the Mt. Tokachi volcano [*Hobiger et al.*, 2010], no significant large-scale crustal deformations were expected during the analyzed period. The deformation rate and area are not large enough to generate measurable effects on our analyzed data. To correct for the topographic fringes, we use the 10-meter mesh DEM by the Geospatial Information Authority of Japan (GSI). The spatial resolution of each multi-looked interferogram is ~80 m in range and azimuth. Phase unwrapping was performed on multi-looked interferograms after applying adaptive spectral filtering with a strength exponent 0.6 and a filtering window size of 32×32 pixels [*Goldstein and Werner*, 1998].

The orbital contribution is removed with the use of precision orbit data by JAXA, which we do not re-estimate further. Nonetheless, long-wavelength residual phases sometimes remain in the initial interferogram, which could be due to either orbit errors, tropospheric delays, ionospheric delays, or a combination of these effects. However, as we cannot accurately quantify each contribution of these long-wavelength noises, we simply subtract any long-wavelength phases by fitting with second-order polynomials expressed in Equation (2.7) in both range and azimuth direction. Although this procedure surely prevents us from detecting long-wavelength small-amplitude tectonic deformation signals, we do not aim in this study to detect such signals. In the following MSM- and WRF-based approach, however, the removal of long-wavelength polynomials was performed after the subtraction of NWM-based corrections, because the NWM-based models include their own long-wavelength phases. Although the long-wavelength tropospheric model could be useful for long-wavelength deformation studies [*Fournier et al.*, 2011; *Jolivet et al.*, 2011], we removed them to perform fair comparison at small- to medium-wavelength

scales.

4.2.3 Topography-correlated delay correction

Topography-correlated delay correction is readily performed by a simple linear regression analysis on the unwrapped differential phases with the aid of a DEM, and is capable of efficiently reducing the tropospheric artifacts [e.g., *Fujiwara et al.*, 1999; *Cavalié et al.*, 2008; *Ozawa and Shimizu*, 2010]. To compare the results with those derived from NWM-based approaches, we also assume that the tropospheric phase is a linear function of the local elevation and an additional constant. We derive the two coefficients, a_{topo} that is proportional to the elevation and a constant a_{const}, and apply these to the InSAR phases every 32 pixels along range and azimuth directions. The corrected interferogram ϕ_{tc} can be represented as follows:

$$\phi_{tc} = \phi_{org} - (a_{const} + a_{topo}H), \tag{4.2}$$

where ϕ_{org} and H are the interferogram phase after removal of long-wavelength polynomial phases and the local elevation, respectively.

4.2.4 MSM-based approach

In order to examine how effective the operational NWM output is, we compute tropospheric delays, using the temperature, pressure, and water vapor data from the JMA/MSM gridded data.

The JMA/MSM data are available every three hours a day. *Ozawa and Shimizu* [2010] used the data at two nearby epochs to linearly interpolate the data at the instant of

Table 4.1: Details of the processed image pairs

Pair	Master	Slave	Path	Frame	Mode	Bperp (m)	Span (days)	DSC/ASC
D1	24/09/2006	29/06/2008	56	2740	FBS-FBS	1504.0	644	D
D2	24/09/2006	14/08/2008	56	2740	FBS-FBS	-451.5	690	D
D3	12/05/2007	17/05/2009	56	2740	FBS-FBS	-935.5	736	D
D4	12/08/2007	27/09/2007	56	2740	FBS-FBD	495.3	46	D
D5	12/08/2007	29/06/2008	56	2740	FBS-FBS	-1192.9	322	D
D6	12/08/2007	17/08/2009	56	2740	FBS-FBS	-1050.8	736	D
D7	12/08/2007	02/10/2009	56	2740	FBS-FBS	-740.6	782	D
D8	12/08/2007	05/07/2010	56	2740	FBS-FBS	1160.4	1058	D
D9	12/08/2007	20/08/2010	56	2740	FBS-FBS	1363.5	1104	D
D10	27/09/2007	12/11/2007	56	2740	FBD-FBD	81.7	46	D
D11	27/09/2007	29/06/2008	56	2740	FBD-FBS	-1688.0	276	D
D12	27/09/2007	02/10/2009	56	2740	FBD-FBS	-1235.5	736	D
D13	27/09/2007	05/07/2010	56	2740	FBD-FBS	664.9	1012	D
D14	27/09/2007	20/08/2010	56	2740	FBD-FBS	868.0	1058	D
D15	27/09/2007	05/10/2010	56	2740	FBD-FBS	1216.5	1104	D
D16	14/05/2008	05/10/2010	56	2740	FBS-FBS	-565.7	874	D
D17	29/06/2008	14/08/2008	56	2740	FBS-FBS	-1955.3	46	D
D18	29/06/2008	17/05/2009	56	2740	FBS-FBS	-267.3	322	D
D19	29/06/2008	17/08/2009	56	2740	FBS-FBS	142.4	414	D
D20	29/06/2008	02/10/2009	56	2740	FBS-FBS	452.5	460	D
D21	17/05/2009	17/08/2009	56	2740	FBS-FBS	409.7	92	D
D22	17/05/2009	02/10/2009	56	2740	FBS-FBS	719.9	138	D
D23	17/08/2009	02/10/2009	56	2740	FBS-FBS	310.2	46	D
D24	20/05/2010	05/07/2010	56	2740	FBS-FBS	-114.2	46	D
D25	20/05/2010	20/08/2010	56	2740	FBS-FBS	89.0	92	D
D26	20/05/2010	05/10/2010	56	2740	FBS-FBS	437.6	138	D
D27	05/07/2010	20/08/2010	56	2740	FBS-FBS	203.1	46	D
D28	05/07/2010	05/10/2010	56	2740	FBS-FBS	551.8	92	D
D29	20/08/2010	05/10/2010	56	2740	FBS-FBS	348.7	46	D
A1	28/06/2007	13/08/2007	397	860	FBD-FBD	253.6	46	A
A2	28/06/2007	28/09/2007	397	860	FBD-FBD	535.0	92	A
A3	28/06/2007	30/06/2008	397	860	FBD-FBD	-836.8	368	A
A4	28/06/2007	18/08/2009	397	860	FBD-FBD	-954.6	782	A
A5	28/06/2007	03/10/2009	397	860	FBD-FBD	-363.9	828	A
A6	13/08/2007	28/09/2007	397	860	FBD-FBD	281.4	46	A
A7	13/08/2007	30/06/2008	397	860	FBD-FBD	-1090.4	322	A
A8	13/08/2007	18/08/2009	397	860	FBD-FBD	-1208.1	736	A
A9	13/08/2007	03/10/2009	397	860	FBD-FBD	-617.5	782	A
A10	13/08/2007	06/07/2010	397	860	FBD-FBD	1123.3	1058	A
A11	13/08/2007	21/08/2010	397	860	FBD-FBS	1424.6	1104	A
A12	28/09/2007	30/06/2008	397	860	FBD-FBD	-1371.8	276	A
A13	28/09/2007	03/10/2009	397	860	FBD-FBD	-899.0	736	A
A14	28/09/2007	21/05/2010	397	860	FBD-FBD	735.1	966	A
A15	28/09/2007	06/07/2010	397	860	FBD-FBD	842.0	1012	A
A16	15/05/2008	06/10/2010	397	860	FBD-FBD	-632.8	874	A
A17	30/06/2008	18/08/2009	397	860	FBD-FBD	-117.8	414	A
A18	30/06/2008	03/10/2009	397	860	FBD-FBD	472.9	460	A
A19	18/08/2009	03/10/2009	397	860	FBD-FBD	590.6	46	A
A20	21/05/2010	06/07/2010	397	860	FBD-FBD	106.8	46	A
A21	21/05/2010	21/08/2010	397	860	FBD-FBS	408.2	92	A
A22	21/05/2010	06/10/2010	397	860	FBD-FBD	687.1	138	A
A23	06/07/2010	21/08/2010	397	860	FBD-FBS	301.3	46	A
A24	06/07/2010	06/10/2010	397	860	FBD-FBD	580.3	92	A
A25	21/08/2010	06/10/2010	397	860	FBS-FBD	278.9	46	A

SAR data acquisition, and we followed the same procedure. The spatial resolution of JMA/MSM is 10 km, and at 16 constant pressure levels along the vertical axis. Because the ray-tracing of tropospheric delay has to be performed along the radar line of sight, we have to know the actual ellipsoidal height of the surface at a spatial resolution comparable to the interferogram. Because of the coarse resolution of the MSM, we obviously need to perform spatial interpolation not only along the horizontal but also along the vertical directions. Consequently, as in all previously published NWM-based approaches, the MSM-based correction is dependent on the fine-resolution digital ellipsoidal-height model as well.

In order to match the spatial resolution of the interferogram, KARAT first regrids and interpolates the NWM data [*Hobiger et al.*, 2008]. The KARAT searches for 8 grid points in the original MSM data that enclose any arbitrary starting point in the interferogram. Thereby, the lower 4 points are from the closest layer below the point, and the upper 4 points are from the nearest layer above the point. Once these 2×4 points are found, a bilinear interpolation is performed to obtain a value at the desired point at each layer. Finally, a vertical exponential interpolation is performed to get the refractivity at the point, thereby the ray-tracing starts to derive the tropospheric delay. A vertical interpolation based on the grid nodes, however, might introduce significant artifacts where the weather model's DEM differs significantly from the real topography. Nevertheless, in the case of our study, at only less than 0.5 percent of the total pixels the weather model's DEM differ by more than 200 m from the DEM used to generate interferograms. Therefore the issue about a vertical interpolation doesn't affect our results and conclusions. Setting the delay estimates for the master and slave image as D_m and D_s, the MSM-based corrected interfero-

gram ϕ_{msm} becomes as follows;

$$\phi_{msm} = \phi_{int} - (D_m - D_s). \tag{4.3}$$

where ϕ_{int} denotes the initial interferogram.

As stated before, the $(D_m - D_s)$ in Equation (4.4) also includes long-wavelength phases. Thus, after subtracting $(D_m - D_s)$ from ϕ_{int}, we remove the long-wavelength phases by the polynomial fitting to the ϕ_{msm}. The same procedure is performed in the following WRF-based correction, too.

4.2.5 WRF-based approach

The MSM data are much coarser than the interferogram in terms of their spatial resolution, and are available only 8 times a day (every 3 hours). The WRF model can produce spatially denser tropospheric data at the instant of the SAR data acquisition with the expectation that the WRF would provide a more realistic troposphere.

WRF is a non-hydrostatic numerical weather prediction model mainly developed at U. S. National Center for Atmospheric Research (NCAR) and National Center for Environmental Prediction (NCEP), and is the next generation model of the MM5 which has been used by *Foster et al.* [2006] and *Puysségur et al.* [2007] for similar studies. Employing the output data of JMA/MSM as the initial and boundary conditions for the WRF, we perform the numerical integration. Here, the numerical integration consists of two nested domains increasing in resolution (3, 1 km and shown in Figure 4.1. For the topography in the NWM, we use the global topography model (GTOPO30) with a horizontal resolution of 1 km, which is still coarser

than that of the interferogram. In the vertical direction, there are 60 layers from the ground surface to the 10 hPa level (~30 km altitude). Since some parameter data such as soil moisture are not provided in the JMA/MSM data, we complement them with those available from the global objective analysis data by U.S. NCEP (http://dss.ucar.edu/datasets/ds083.2/). Although it is possible to change a variety of parameter settings in the WRF, we set all the parameters as default values. The prediction performance of the WRF is shown be comparable to that of JMA's Non-Hydrostatic Model at the spatial resolution of 20 km [*Hayashi et al.*, 2008; *Chan et al.*, 2010], but an inter-comparison of non-hydrostatic models is beyond the scope of this paper. As done in the MSM-based reduction, the original WRF data are re-gridded and interpolated to match the spatial resolution of the interferogram. The corrected interferogram ϕ_{WRF} becomes as follows;

$$\phi_{WRF} = \phi_{int} - (D'_m - D'_s). \tag{4.4}$$

4.3 Results and Discussion

The 54 original and corrected interferograms are shown in Figures 4.3 and 4.4. We observe that all the data pairs include signals correlated with the local topography although the extent of correlation varies in each case. The peak-to-peak amplitude of the topography-correlated signals can reach 10~20 cm changes along the radar LOS. In addition to the topography-correlated signals, we also notice broad signals with the spatial scale of 5~50 km that are not correlated with the topography. We consider that most of them are due to the heterogeneous tropospheric delays.

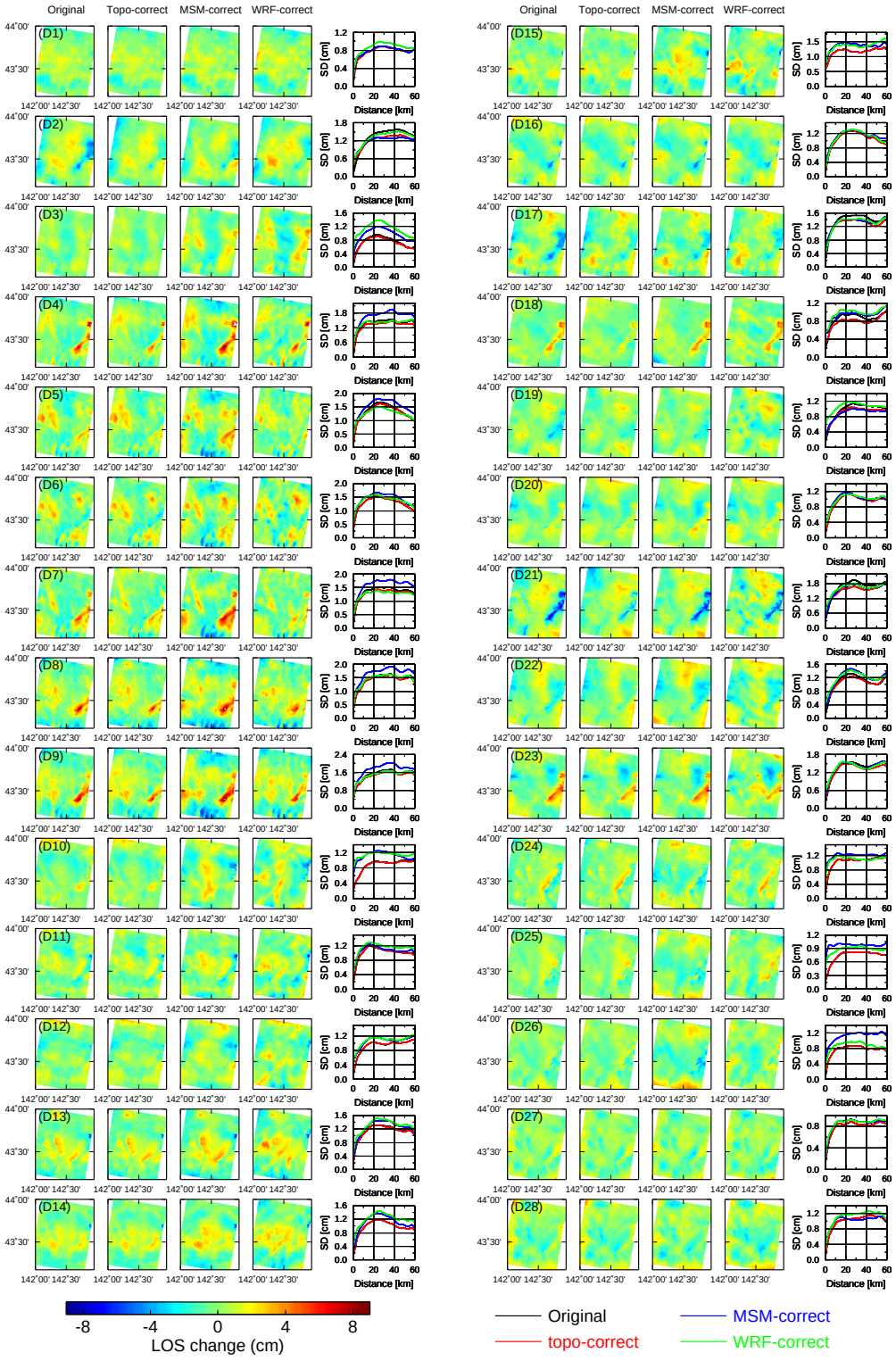

Figure 4.3: 28 original and corrected interferograms and their variograms. (Left column) Original interferogram after removal of long-wavelength phases, (Second column from left) Topography-correlated delay correction based on DEM, (Third column from left) MSM-based correction, (Fourth column from left) WRF-based correction, (Fifth column from left) the variograms of four interferograms. Details of each pair are listed in Table 4.1.

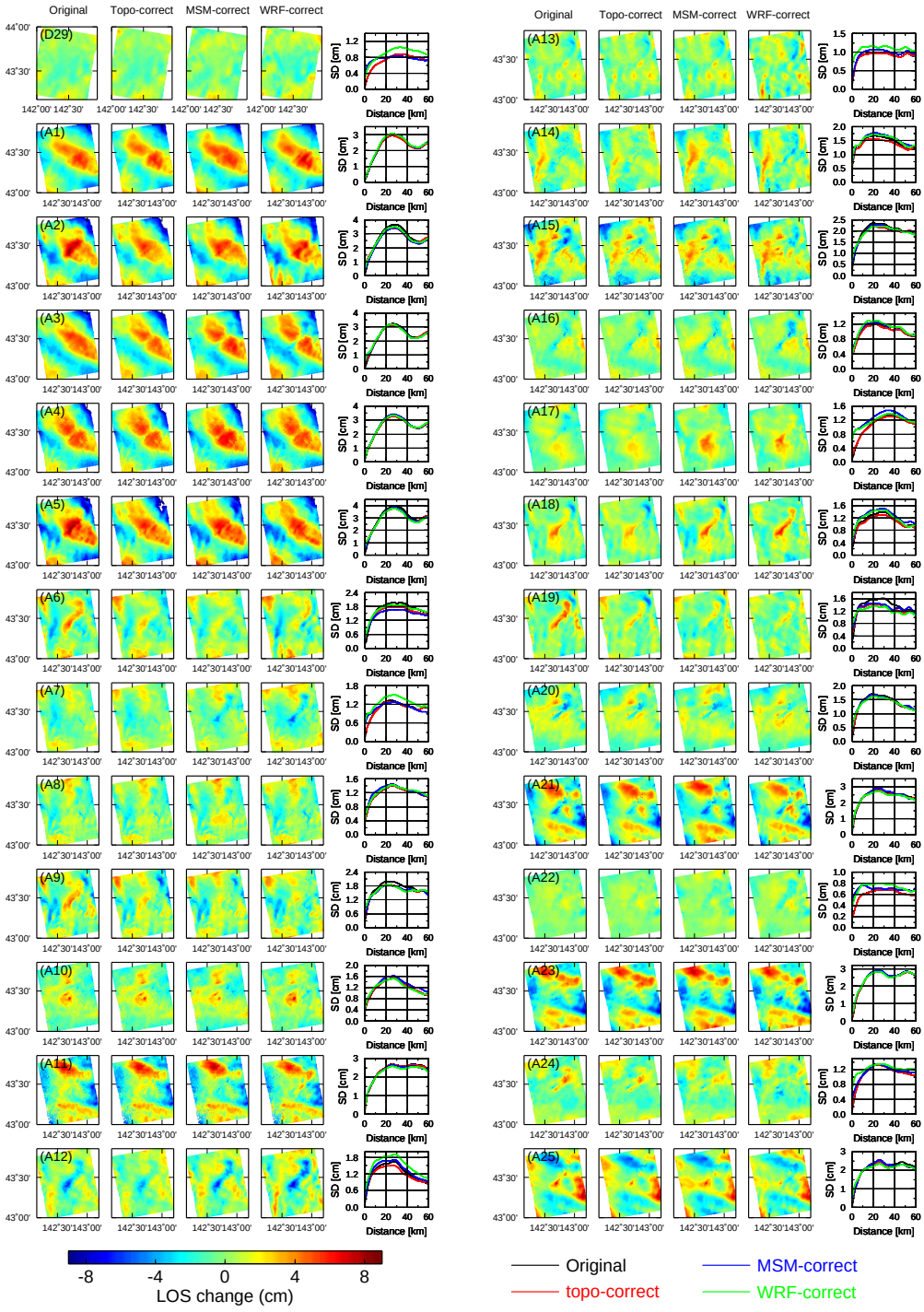

Figure 4.4: 26 original and corrected interferograms and their variograms. (Left column) Original interferogram after removal of long-wavelength phases, (Second column from left) Topography-correlated delay correction based on DEM, (Third column from left) MSM-based correction, (Fourth column from left) WRF-based correction, (Fifth column from left) the variograms of four interferograms. Details of each pair are listed in Table 4.1.

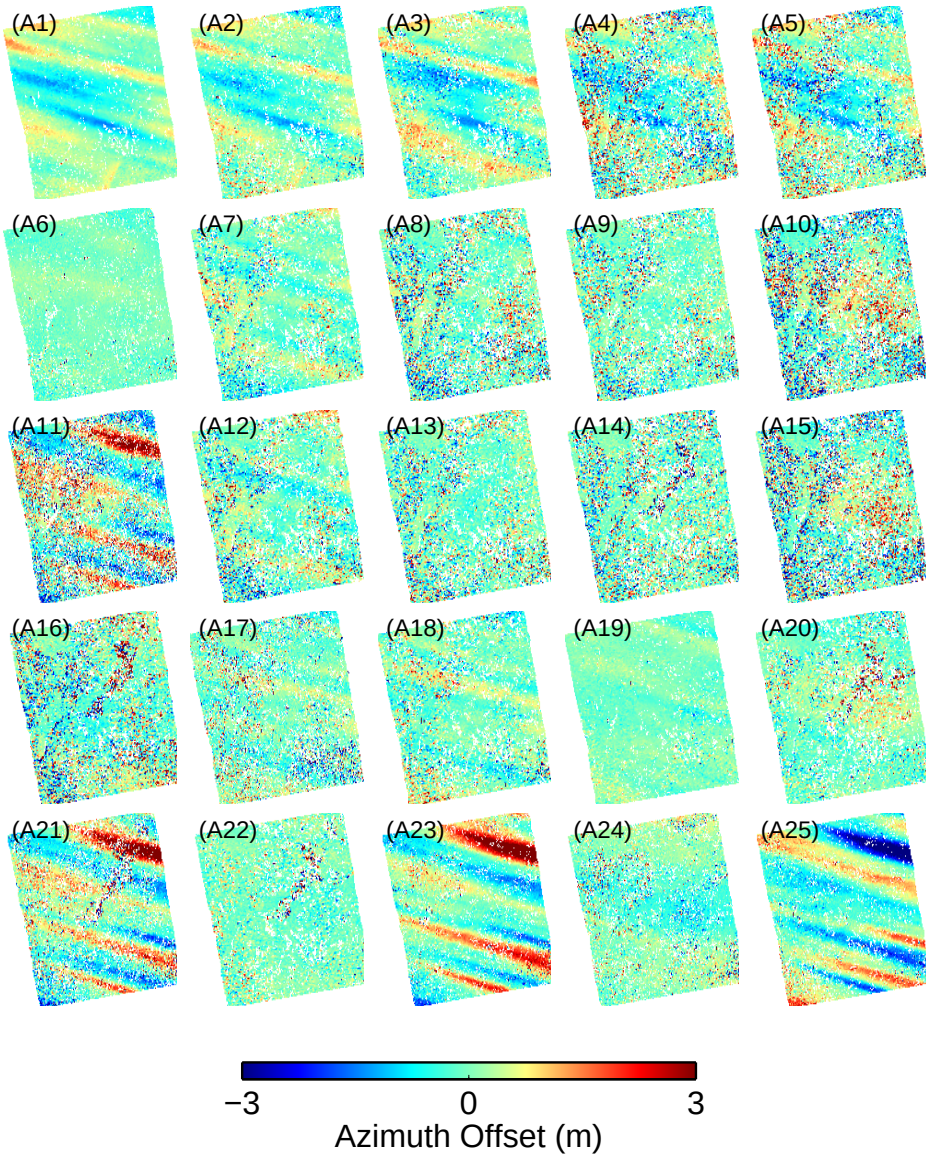

Figure 4.5: Azimuth offsets of ascending orbit data. Details of each pair are listed in Table 4.1.

However, in the case of L-band SAR data, the effect of ionospheric signal becomes significant as compared to the C-band and X-band SAR data (e.g. ERS, ENVISAT, and TerraSAR-X), and may be a non-negligible error source in some of the ALOS/PALSAR interferograms [*Shimada et al.*, 2008]. We can judge the

ionospheric effects on the interferogram from the azimuth offset data since spatial variations in the free electron density in the ionosphere can cause azimuth positional shifts and are observed as "azimuth streak" in the azimuth offset data [*Gray et al.*, 2000; *Meyer et al.*, 2006]. Figures 4.5 and 4.6 show the azimuth offset data of ascending and descending orbit, respectively (see Table 4.1). The clearer streaks in the ascending data probably appear because the PALSAR data are acquired at the local time around 22:30, when the ionospheric disturbances are larger than during the day (descending data). However, because the impact of ionospheric disturbances on the interferogram is evaluated from an integration of the azimuth offset along the azimuth (flight) direction [*Meyer et al.*, 2006], the ionospheric effects will generate longer-wavelength phases in the interferogram that were mostly taken out by the removal with the polynomial fitting. In this study, 9 azimuth offset data (Figure 4.5, A1-A5, A11, A21, A23 and A25) show clear streaks due to the ionosphere, and interferograms of those data reveal larger long-wavelength phase disturbances than other data. Consequently, the effects of ionosphere on some but not all of the original ascending InSAR data are not negligible.

The second column in Figures 4.3 and 4.4 shows interferograms after the topography-correlated delay correction. We notice that the topography-correlated signals were notably reduced particularly for 19 interferograms (D2, D4, D5, D7-D9, D17, D18, D21, D23 in Figure 4.3, and , , A2, A5, A6, A9, A12, A14, A15, A18, and A19 in Figure 4.4), each of which included large apparent range changes around the mountain areas (see first column in Figures 4.3 and 4.4). However, we also observe that there still remain signals that are correlated with the topography with amplitudes reaching ±5 cm, for instance in D8, D9, and D23. In Figure 4.4 A6,

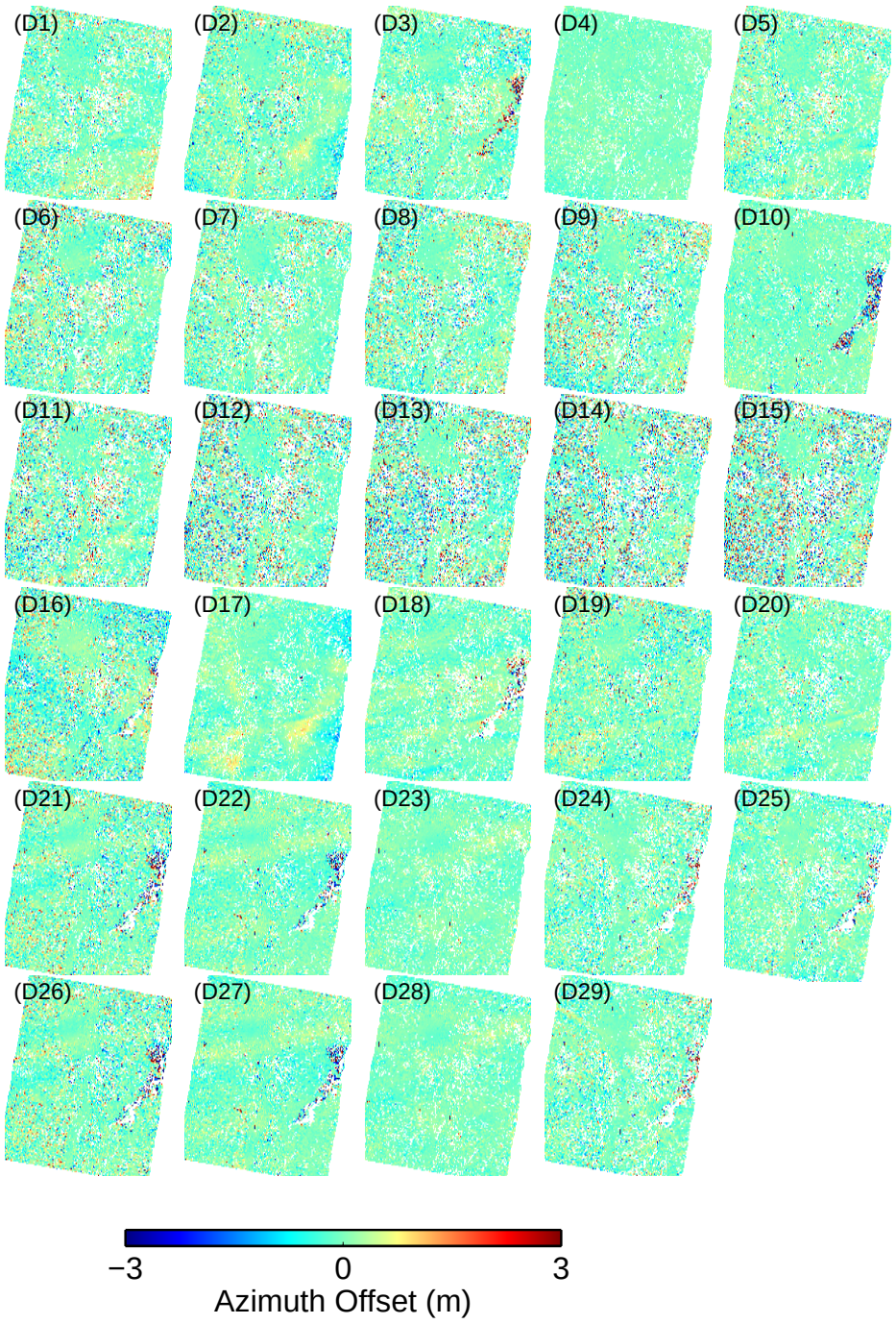

Figure 4.6: Azimuth offsets of descending orbit data. Details of each pair are listed in Table 4.1.

for example, the areas of positive range changes around the mountain areas clearly decreased with topography-correlated delay correction, but those negative changes to the south-east of the mountain areas do not change appreciably. The first-order polynomial regression as expressed by Equation (4.3) might be not optimal for the entire scene, and higher-order polynomial regression may be necessary. More elaborate DEM-based approaches may be able to reduce the apparent signals [e.g., *Lin et al.*, 2010]. However, as we often aim to detect crustal deformation signals that are correlated with the regional topography, which is often the case, for instance, at volcanoes [*Beauducel et al.*, 2000] and along major faults [*Elliot et al.*, 2008], and thus the DEM-based approaches should be applied very carefully in order not to take out the desired deformation signals.

The third column of Figures 4.3 and 4.4 shows interferograms after the MSM-based delay correction. In 11 interferograms (D2, D17, D19, D21, D24 in Figure 4.3, and A2, A5, A6, A9, A19, and A24 in Figure 4.4), we observe that the large amplitude signals in original interferograms could be efficiently reduced, particularly over the mountain areas. Especially for D19 and A6, the MSM-based approach reduces the signals more efficiently than the DEM-based approach. However, we also acknowledge that in some cases there arises other apparent LOS changes on the order of ~5 cm that were absent in original interferograms. For instance, those distributed in the mountain areas in D3 of Figure 4.3, to the north and to the south in D26 and to the middle of A17 were all generated after the MSM-based correction. It is thus evident that the MSM-based approach does not always eliminate the tropospheric signals. Additionally, in A24 the positive signals in the middle to the north-east of the original interferogram were absent after the MSM-based correction, but arose

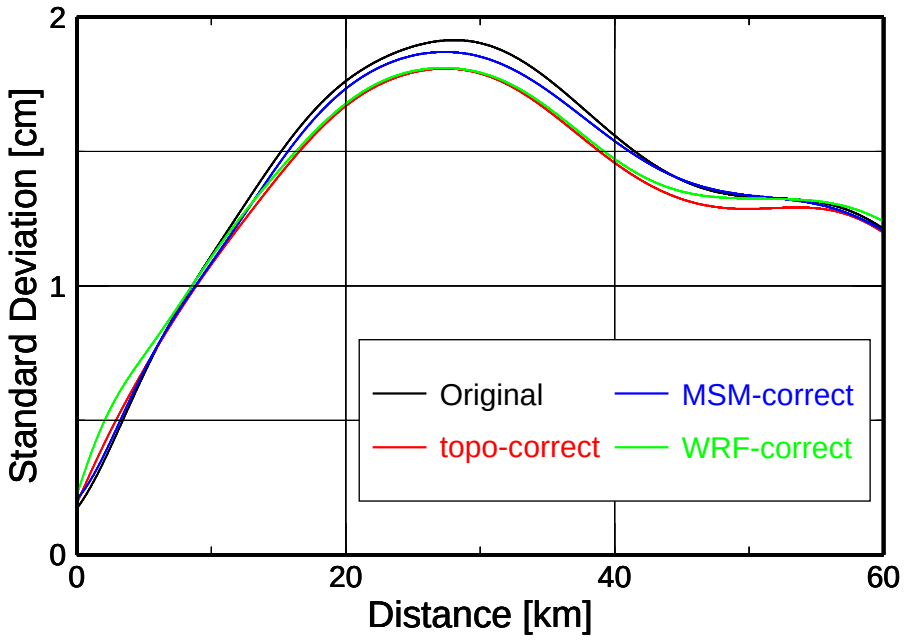

Figure 4.7: Variograms of four original and corrected interferograms for all (54) data pairs.

around the north-west corner and to the south-east with a scale of ~20 km that were absent in the original interferogram. Since those signals are not apparently correlated with the topography, we consider that they could represent some non-stratified heterogeneous signals and would be artifacts due to the errors in the MSM data. The ionospheric influence in A24 seems to be small in light of the small amplitude in the azimuth offset data of A24 in Figure 4.5.

The fourth column of Figures 4.3 and 4.4 shows interferograms after the WRF-based delay correction. Overall, derived interferograms reveal similar signals as those after the MSM-based correction. The topography-correlated signals in the original interferograms became smaller by WRF-based approach as observed in interferograms after MSM-based correction. However, we need to acknowledge that,

even if the WRF-data are derived at the instant of SAR data acquisitions with a spatial scale of 1-km, the heterogeneous signals with the spatial scale ranging from 5 to 50 km may not be efficiently reduced (for example, see D12, D23, A7, and A14 in Figures 4.3 and 4.4). Although we performed the numerical integration using the WRF model with 1-km spatial scale, we should recall that the initial and boundary conditions for the numerical integration are all based on the MSM and NCEP analysis data whose spatial and temporal resolution is coarser than those in the WRF. As discussed by *Wadge et al.* [2010], we need more accurate data sets for the initial and boundary conditions.

It is evident from Figures 4.3 and 4.4 that the amplitude of tropospheric delay signals depends on the spatial scale and tends to become larger as the spatial scale becomes larger. Although it can be simply computed and sometimes useful, a single standard deviation computed from the entire pixel population in the residual interferogram does not represent the multi-scale characteristics in the tropospheric delay signals. In order to quantify the magnitude of the residual tropospheric delays in each interferogram, we use the variogram,

$$\gamma(\mathbf{h}) = \frac{1}{2}\left(\phi(\mathbf{x}) - \phi(\mathbf{x}+\mathbf{h})\right)^2 \tag{4.5}$$

which computes the variance of all pixel pairs at a given distance h and allow us to examine the scale-dependence of the two-dimensional signals [e.g. *Hanssen*, 2001; *Hobiger et al.*, 2010; *Ozawa and Shimizu*, 2010].

The fifth column of Figures 4.3 and 4.4 shows the square-root of the variogram (standard deviation, SD) for each interferogram with and without the tropospheric delay corrections. In the variograms, a reduction of the SD over the wavelengths of

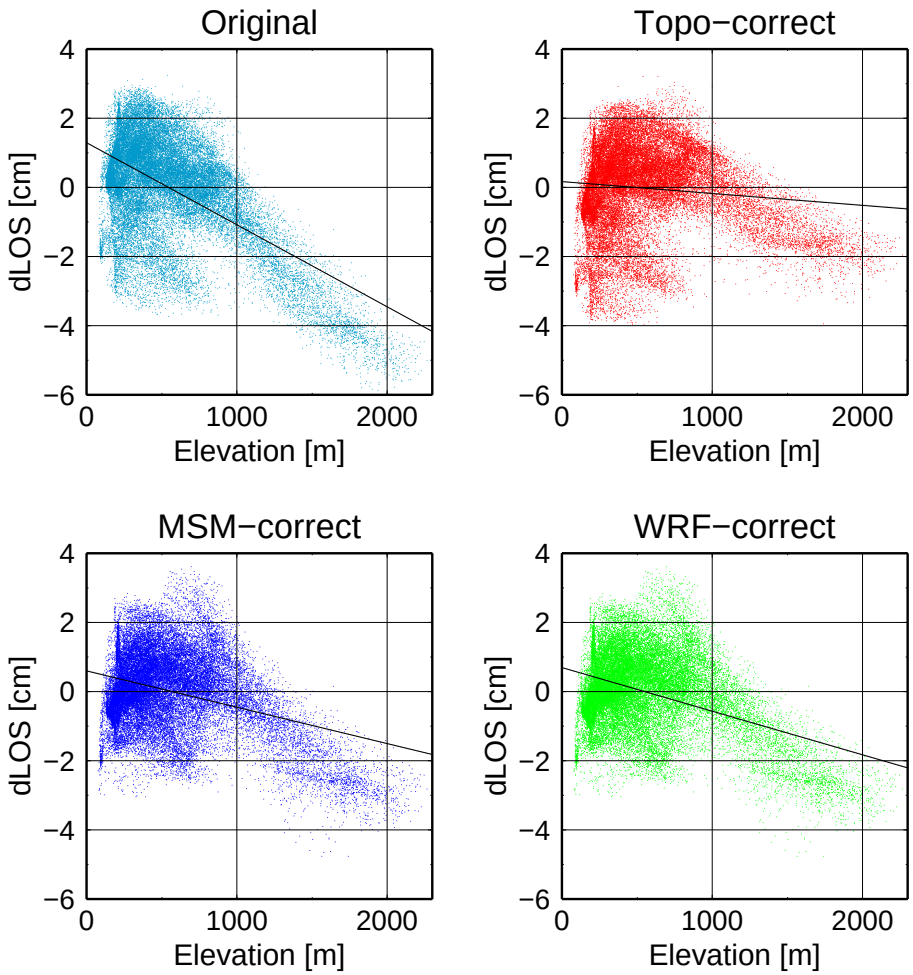

Figure 4.8: Variation of the phase with elevation of the surface and the approximated line (black line) in D2 (see Table 4.1). (Upper left) Scatter plot of the original interferogram. (Upper right) That of the DEM-based corrected interferogram. (Bottom left) That of the MSM-based corrected interferogram. (Bottom right) That of the WRF-based corrected interferogram.

20~40 km is recognized in 20 interferograms for the DEM-based correction, in 9 interferograms for the MSM-based correction and in 15 interferograms for the WRF-based correction. However, we also recognize a SD increase in 25 interferograms for the MSM-based correction and 23 interferograms for the WRF-based correction. It turns out that the performance of each correction approach strongly depends on each

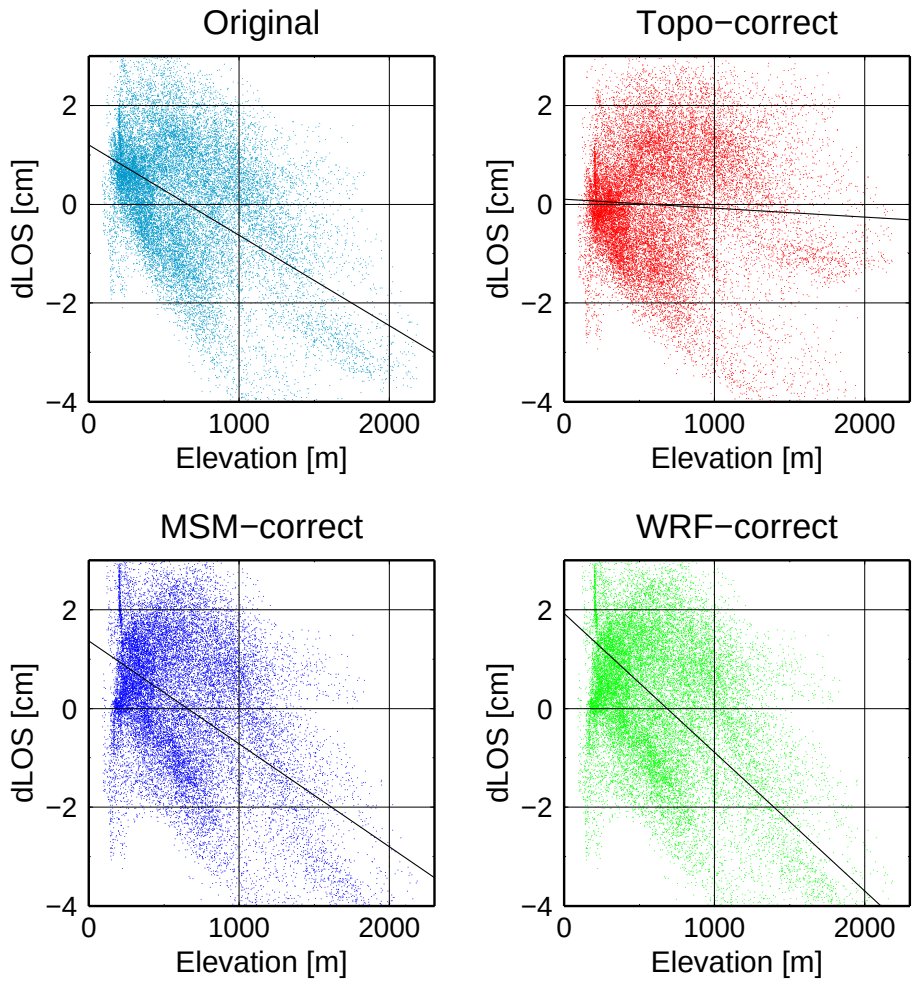

Figure 4.9: Variation of the phase with elevation of the surface and the approximated line (black line) in A12 (see Table 4.1). (Upper left) Scatter plot of the original interferogram. (Upper right) That of the DEM-based corrected interferogram. (Bottom left) That of the MSM-based corrected interferogram. (Bottom right) That of the WRF-based corrected interferogram.

interferogram, and that no straightforward conclusions can be drawn regarding the different correction approaches.

Figure 4.7 shows summarized variograms of four original and corrected interferograms for all 54 data pairs shown in Figures 4.3 and 4.4. This also indicates that the DEM-based approach is the most effective for correcting original interfero-

grams chosen here. However, the WRF-based approach shows the performance as equivalent as the DEM-based approach over the wavelengths of 20~40 km, but worse performance over the wavelengths of shoter than 20 km and longer than 40 km. The amount of SD reduction of the MSM-based approach is smaller than that of other approaches in this study, although a SD reduces in a way.

We examined how the phase dependence with elevation varied after each correction approach. Figures 4.8 and 4.9 are examples for D2 and A12, respectively. Whereas the MSM- and WRF-based correction reduce the phase dependences with elevation and the extent of the ”non-stratified” phase variation in the interferogram of D2 (Figure 4.8), those in A12 increase the effect (Figure 4.9). Figures 4.10 and 4.11 summarize the analysis for all interferograms, and indicate how each correction reduced or increased the phase dependences with elevation, by normalizing with the slope of original interferograms. The MSM-based correction often generate larger slopes that in the original signals (29 interferograms in Figures 4.10 and 4.11), indicating that the MSM-based NWM outputs make the original non-corrected data even ”noisier”; the same results are also found in the WRF-based corrections (23 interferograms in Figures 4.10 and 4.11).

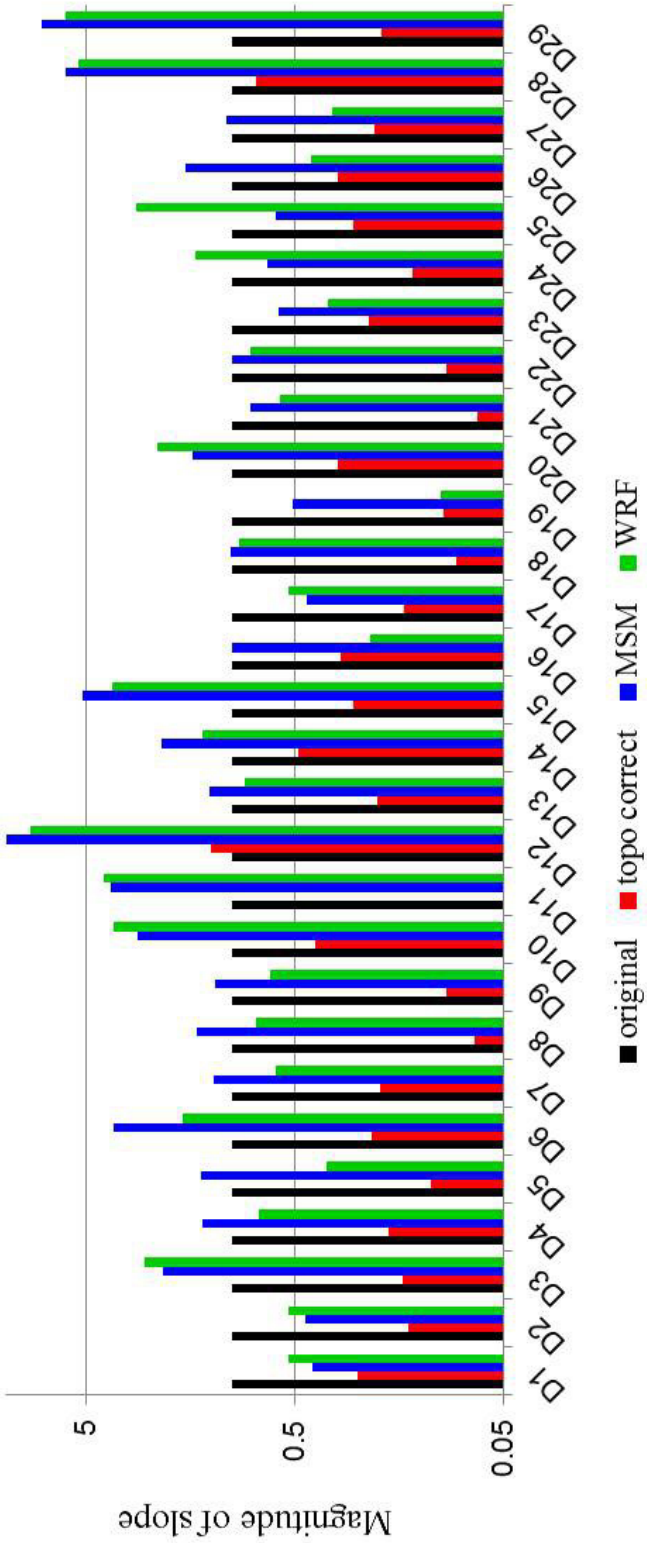

Figure 4.10: The slope magnitude for all 29 descending interferograms with and without the tropospheric delay corrections. Slopes of each interferogram are normalized by that of the original interferogram. The red bar in D11 is absent due to the very small value (0.02).

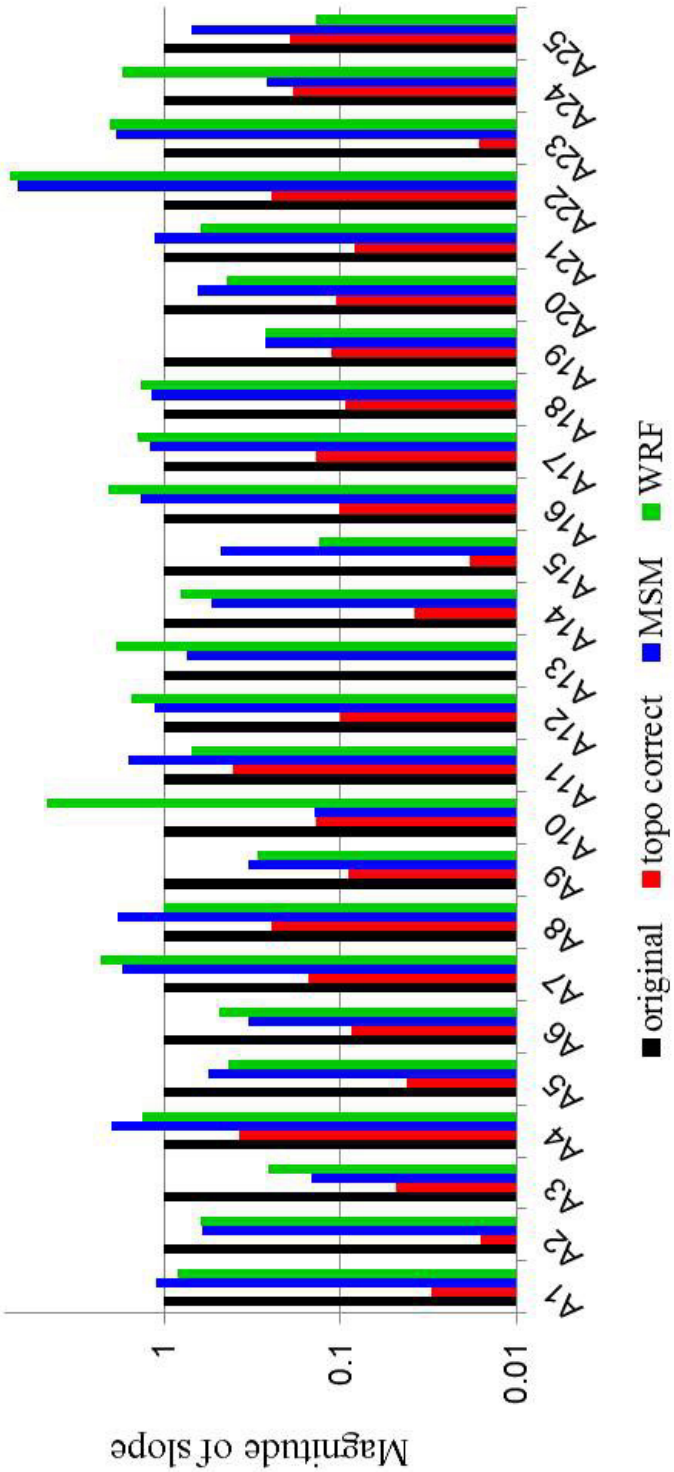

Figure 4.11: The slope magnitude for all 25 ascending interferograms with and without the tropospheric delay corrections. Slopes of each interferogram are normalized by that of the original interferogram. The red bar in A13 is absent due to the very small value (0.00467).

We consider that the initial and boundary conditions for the numerical integration are not accurate and precise enough to fully take advantage of the potential performance of the WRF model. Even if the WRF's spatial resolution is set to be 1-km and we compute the tropospheric state at any desired instant, the initial and boundary conditions are still based on the MSM-based low resolution data. As pointed out by *Jolivet et al.* [2011], while "stratified" tropospheric delay could be significantly reduced with the NWM output, it is not easy to correct for the "non-stratified" (heterogeneous) tropospheric delay because of its poor spatio-temporal resolution. Our study also supports this point to some extent (Figures 4.10 and 4.11); the phase dependence with elevation is reduced in 21 pairs corrected with MSM and 29 pairs with WRF. However, the phase dependence with elevation increases in 29 pairs corrected with MSM and 23 pairs with WRF. It could be because the climate of the case area (Hokkaido, Japan) is humid and variable throughout the year, making the task more challenging than in less variably humid parts of the world. In order to generate better results with the WRF-based approach, we will need much higher-resolution tropospheric data both spatially and temporally, which would surely be possible in the future.

4.4 Summary

We applied three types of tropospheric delay corrections to 54 interferograms formed from 26 SAR images. If the expected deformation signals are not closely correlated with the topography, and if the "stratified" tropospheric phases are dominant, we found that the simple DEM-based approach will be more effective to cor-

rect for the tropospheric phases than using corrections based on the weather models, because the DEM-based approach fit a better model than any other forward models. If one aims to detect small amplitude deformation signals that are correlated with the topography, the NWM-based approach is preferable, and the DEM-based approach should be carefully applied. However, our results indicate that the NWM-based approach is not able to substantially reduce the tropospheric signals when the topography-uncorrelated signals are dominating. We consider that further improvements are necessary in the initial and boundary values for the high spatial-temporal resolution NWM so that the NWM outputs can be helpful in the tropospheric delay correction.

Chapter 5

InSAR observation and numerical modeling of the water vapor signal during a heavy rain: A case study of the 2008 Seino event, central Japan

Paper was published in Geophysical Research Letters

Kinoshita, Y., M. Shimada and M. Furuya, 2013: InSAR observation and numerical modeling of the water vapor signal during a heavy rain: A case study of the 2008 Seino event, central Japan, *Geophys. Res. Lett.*, 40(17), 4740-4744, doi:10.1002/grl.50891.

5.1 Introduction

InSAR phase signals contain information not only regarding ground displacements, but also on the effects of atmospheric delay [e.g., *Zebker et al.*, 1997]. In the absence of signals caused by surface deformations, ionospheric effects and other errors in the digital elevation model or orbit data, InSAR can measure the spatial distribution of precipitable water vapor with unprecedented spatial resolution [*Hanssen et al.*, 1999]. In contrast to precipitation data, water vapor distribution data can convey the distribution of precipitable water, providing unique and useful information about the spatial and temporal evolution of rain systems. For instance, *Shoji et al.* [2009] achieved improved forecasting performance by assimilating the precipitable water vapor data derived from GPS observations for a heavy rain event in Japan.

During 2-3 September 2008, a torrential rain event known as the Seino heavy rain occurred over wide areas of central Japan (Figure 5.1). The Automated Meteorological Data Acquisition System (AMeDAS) of JMA recorded the total precipitation over the two days as 250 mm and 430 mm at Ibigawa and Ozu, respectively. JAXA conducted an emergency observation of the heavy rain using PALSAR, an L-band SAR sensor onboard ALOS, at an off-nadir angle of 45.1°, which is not a normal observation procedure. On 21 January 2010, when atmospheric conditions were dry and stable, JAXA acquired another PALSAR image of the same areas. Using these data, we generated an InSAR image to provide a detailed representation of the heterogeneous water vapor distribution during the heavy rain event. Near the Ibi River, we detected localized but large-amplitude signals that were associated with the water vapor distribution during the heavy rain.

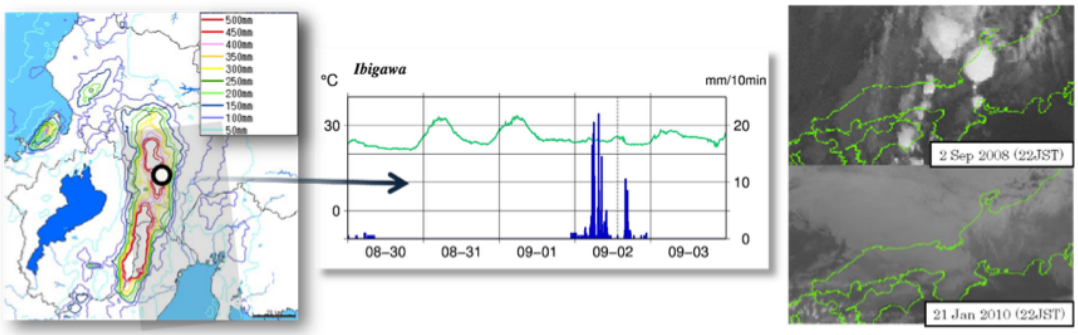

Figure 5.1: (Left) Two-days total precipitation from 2 September 2008 to 3 September 2008 derived from the weather radar observation. (Center) Time-series of 10-min duration rainfall data at *Ibigawa* (the location is depicted as a symbol "I" in Figure 5.2) from 00 JST on 2 September 2008 to 24 JST on 3 September 2008. (Right) Infrared satellite image of MTSAT-1R

The purposes of this study are; 1) to derive the three-dimensional (3D) water vapor distribution that explains the localized signal and 2) to clarify the spatial-temporal evolution of the water vapor signals associated with the Seino heavy rain event using a high-resolution NWM.

5.2 InSAR Data Analysis

To correct for the orbital and topographic fringes, we used precision orbit data from JAXA and the 10 m DEM generated by GSI, respectively. From the two sets of ALOS/PALSAR level 1.0 raw data described above, we generated an unwrapped interferogram (Figure 5.2a) with a perpendicular baseline of 2886.8 m. The interferogram reveals a localized large-amplitude signal (anomaly A in Figure 5.2a), which has a LOS change of approximately 130 mm and a horizontal scale of 10 km near Ibi River. Assuming that this localized signal are doe to water vapor, from Equation (3.42) this signal indicates approximately 15 mm higher PWV in the zenith

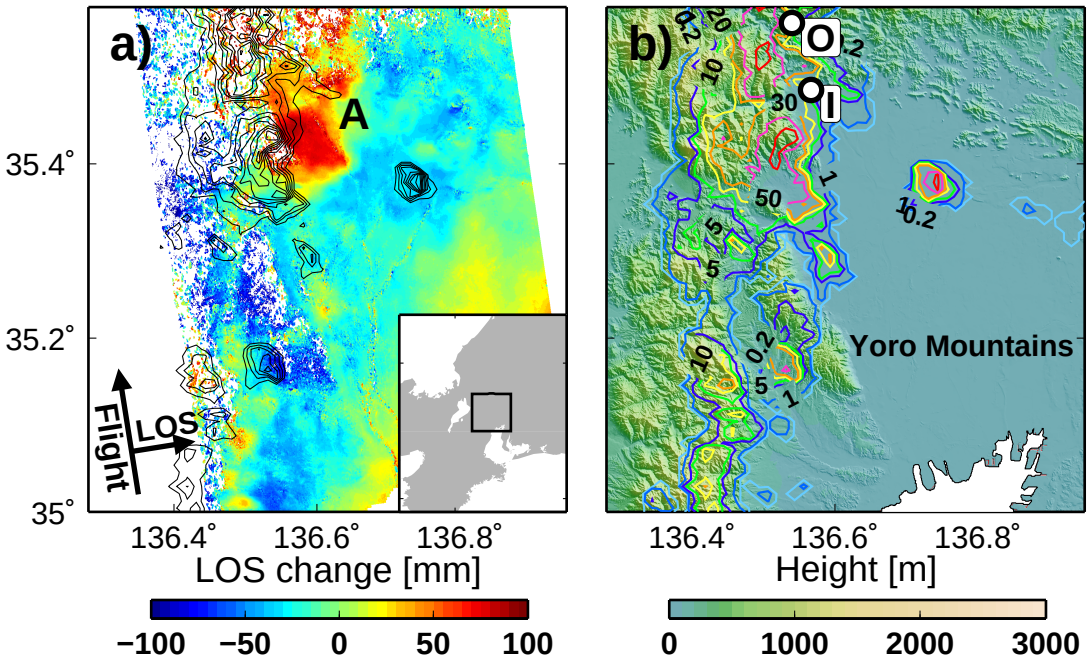

Figure 5.2: (a) The unwrapped differential interferogram. The SAR data were acquired by the L-band ALOS/PALSAR on 2 September 2008 (slave) and 21 January 2010 (master). The contour lines represent the distribution of rainfall intensity at 13:30 UTC, as derived from the weather radar (WR) with an interval of 10 mm/hr. The region of maximum rainfall intensity is located 5 km west of localized signal A in the interferogram. (b) The shaded topographic image and the WR echo distribution with colored contour lines. The values of the colored lines are 80 (red), 50 (pink), 30 (orange), 20 (yellow), 10 (green), 5 (dark blue), 1 (blue) and 0.2 mm/hr (sky blue). White circles I and O indicate the locations of the AMeDAS stations at Ibigawa and Ozu, Japan, respectively.

direction than that of the surrounding mean PWV.

We first verified that this signal was attributable to the water vapor in the troposphere and not from any crustal deformation, DEM error or effect of the ionosphere. An analysis using Japan's dense GPS network, GEONET, detected no crustal deformation in this region. Moreover, other interferograms with the same spatial and temporal coverage as that in Figure 5.2 indicated no significant fringe near anomaly A in Figure 5.2a (Figure 5.3a). The topographic fringe can be expressed in Equation (2.6),

and the interferogram during the heavy rain event have a perpendicular baseline of 2886.8 m. Therefore to assess the DEM error using another interferogram derived from a normal observation procedure with an off-nadir angle of 34.3°, the required perpendicular baseline is,

$$B_{\perp}^{required} = \frac{\sin\theta^{normal}}{\sin\theta^{emergency}} \cdot B_{\perp} = 2296.6[m], \tag{5.1}$$

so that we generated another interferogram using the standard observation mode with a perpendicular baseline of 2179 m, and the sensitivity to the DEM error in this measurement was equivalent to that of the interferogram displayed in Figure 5.2a. In this interferogram (Figure 5.3b), no localized signals were located near anomaly A. Thus, these results indicate that anomaly A can be attributed neither to crustal deformations nor to DEM errors. The ionospheric artifacts become obvious as "streaking" in the azimuth offset data, which is proportional to the derivative of a phase variation with regard to the azimuth direction [*Gray et al.*, 2000; *Meyer et al.*, 2006]. Although azimuth streaks were found in the pair of SAR data sets used in Figure 5.2 (Figure 5.3c), the spatial scale of these azimuth streaks was much greater than that of anomaly A, suggesting that anomaly A was unlikely to have been caused by an ionospheric effect.

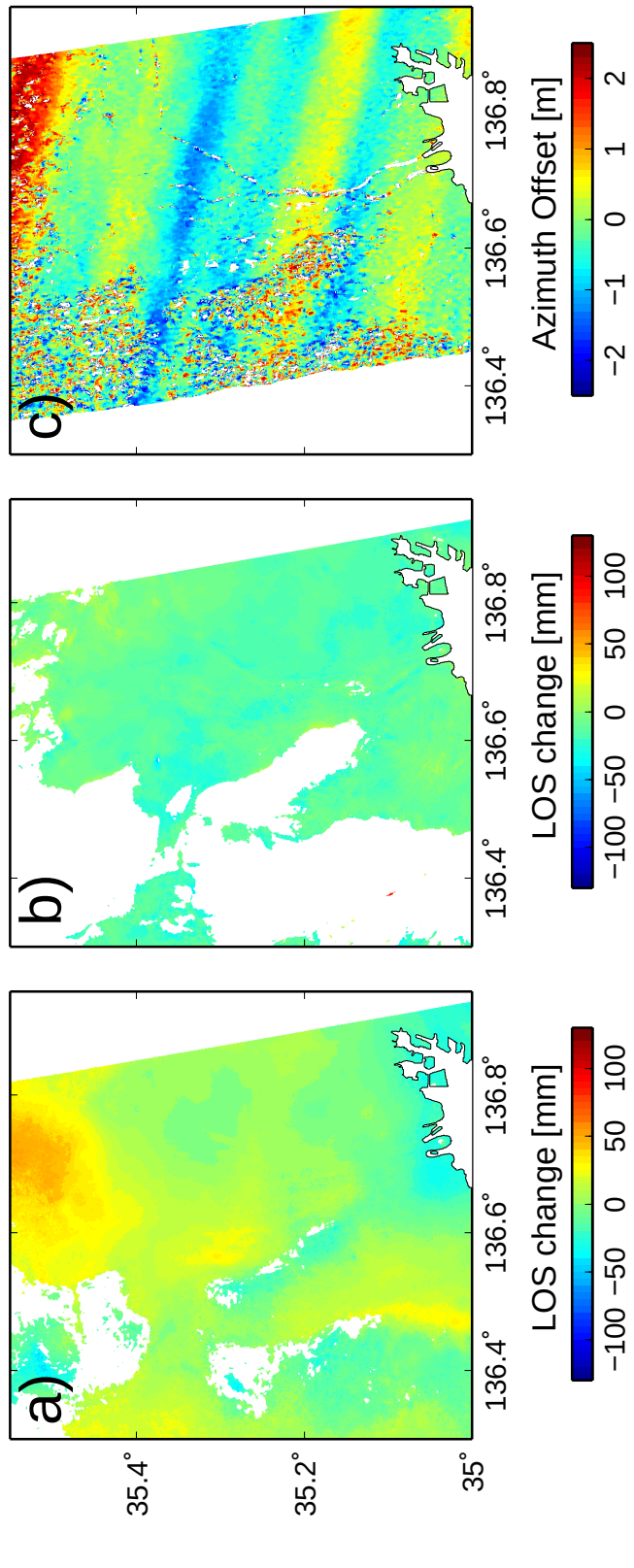

Figure 5.3: Two interferograms for (a) 23 October 2007 - 31 July 2010, with a perpendicular baseline of 559 m, and (b) 9 March 2008 - 28 October 2009, with a perpendicular baseline of 2179 m, and (c) the azimuth offset image.

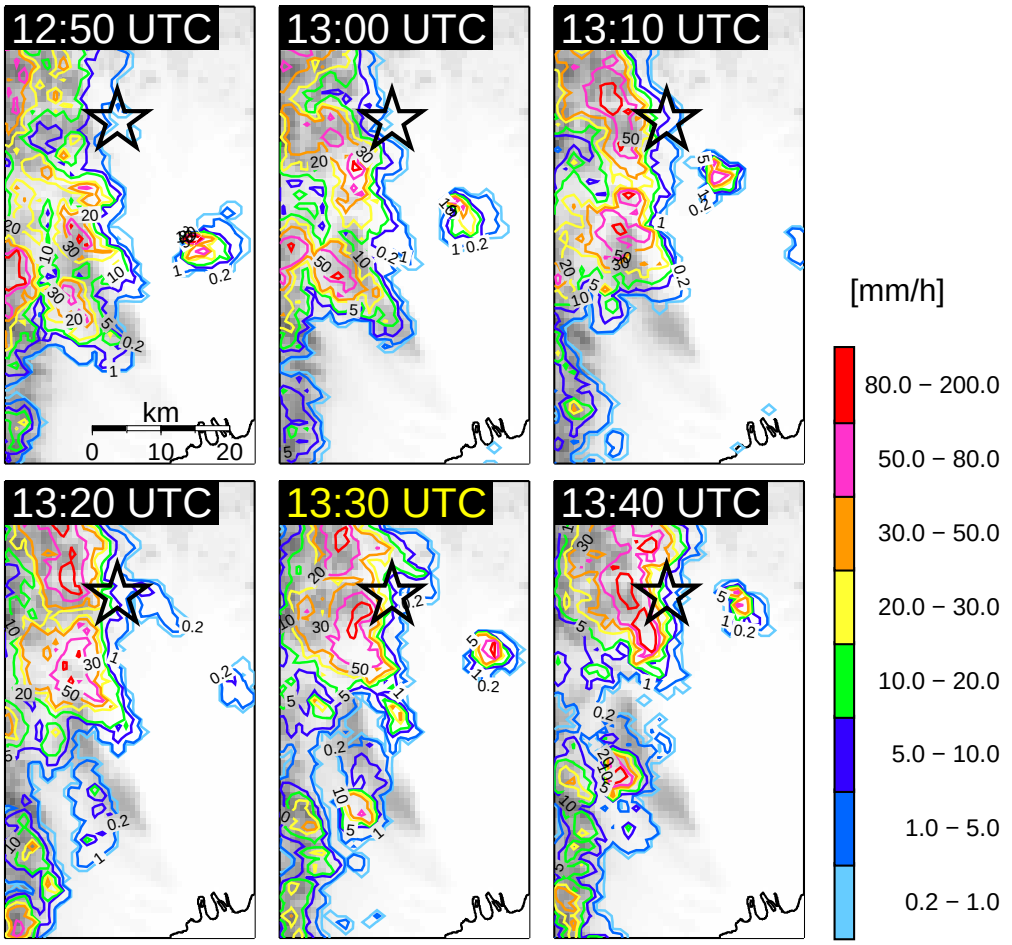

Figure 5.4: Time series of weather radar echo distributions around the SAR observation time.

In addition, the weather radar image at the moment of the SAR image acquisition indicates a small area with a high rainfall intensity at the precise location of anomaly A (Figure 5.2b, contour; Figure 5.4). The high rainfall intensity indicates that there was a well-developed thundercloud at that location, and thus, strongly supporting the interpretation that anomaly A was caused by the presence of water vapor during the heavy rain event.

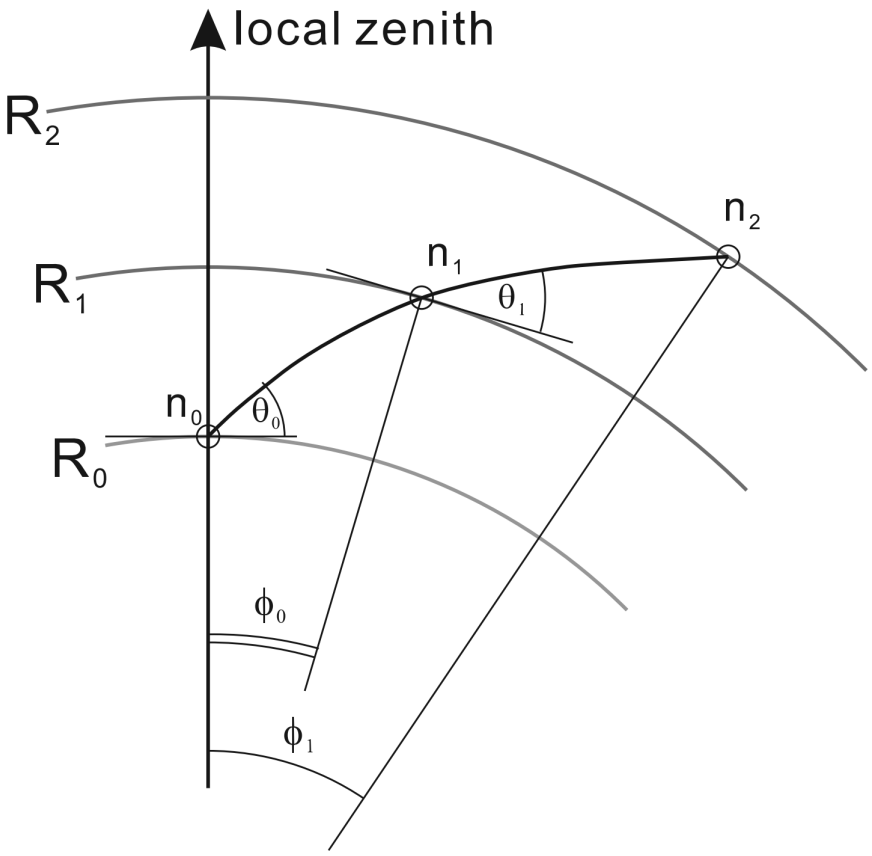

Figure 5.5: The schematic image of the Thayer approach.

5.3 3D Water Vapor Modeling

The propagation delay ΔL of microwaves in a neutral atmosphere can be computed by integrating the refractive index n along their propagation paths and can be expressed as Equation (4.1). The refractive index n can be expressed as a function of the partial pressures of dry air and water vapor and absolute temperature as shown in Equation (3.10) [*Aparicio and Laroche*, 2011]. In this study we set the four constants according to *Aparicio and Laroche* [2011], i.e., $a_1 = 222.682$, $a_2 = 0.069$, $a_3 = 6701.605$, and $a_4 = 6385.886$, respectively. In contrast to the case of GNSS,

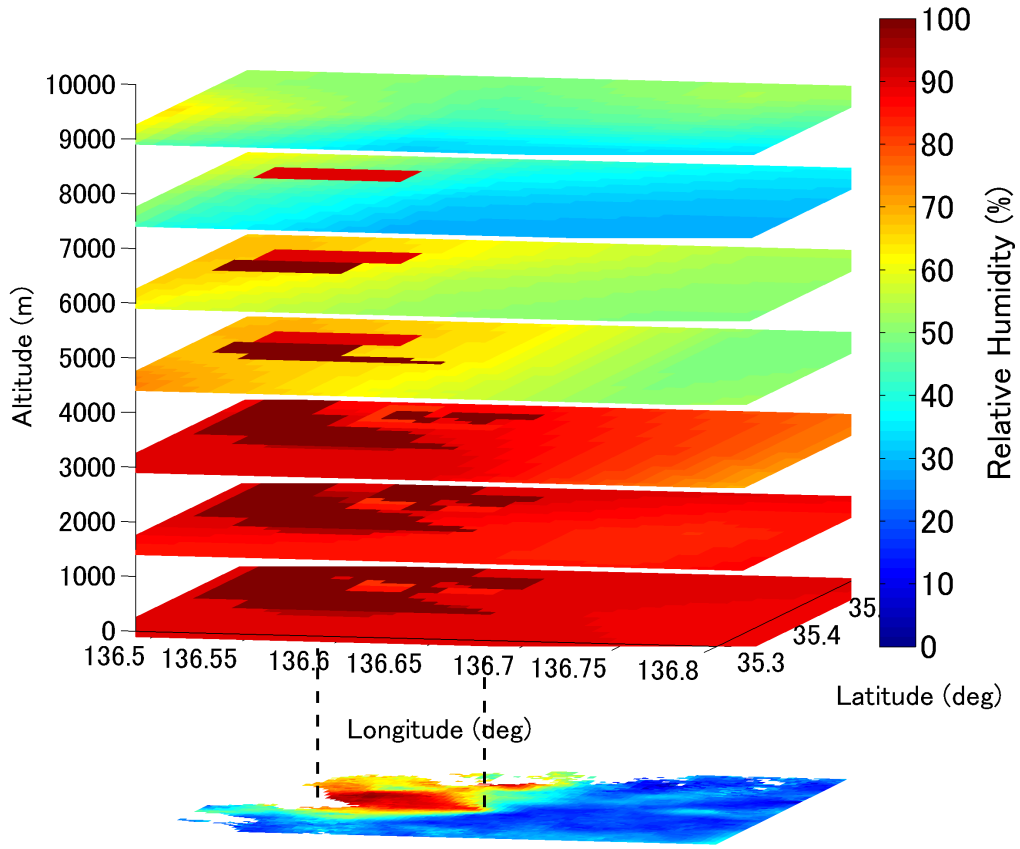

Figure 5.6: The estimated three-dimensional (3D) relative humidity (RH) field. The slant view of the interferogram shown in Figure 5.2 was depicted under the 3D RH field. Saturated air was estimated from the surface to 9000 m above the ground level over anomaly A in Figure 5.2.

we can assume that the delay effect of dry air on InSAR images is negligible [*Zebker et al.*, 1997], and thus the delay effect on InSAR data can be considered as primarily attributable to the heterogeneity of water vapor.

To investigate the distribution of water vapor at the time of the SAR acquisition, a forward model of the 3D water vapor distribution for the heavy rain event was constructed based on anomaly A in Figure 5.2a. The purpose of this modeling was to construct a physically meaningful model for the water vapor that explained

anomaly A, although the model was largely artificial. The extent of tropospheric delay at each pixel was computed using a ray-tracing technique [*Hobiger et al.*, 2008]. The effect of ray bending in the azimuthal direction is negligible in Earth's atmosphere, and thus for computational efficiency, the Thayer approximation that neglects the bending effect in the azimuthal direction was used [*Hobiger et al.*, 2008]. The schematic image is illustrated in Figure 5.5.

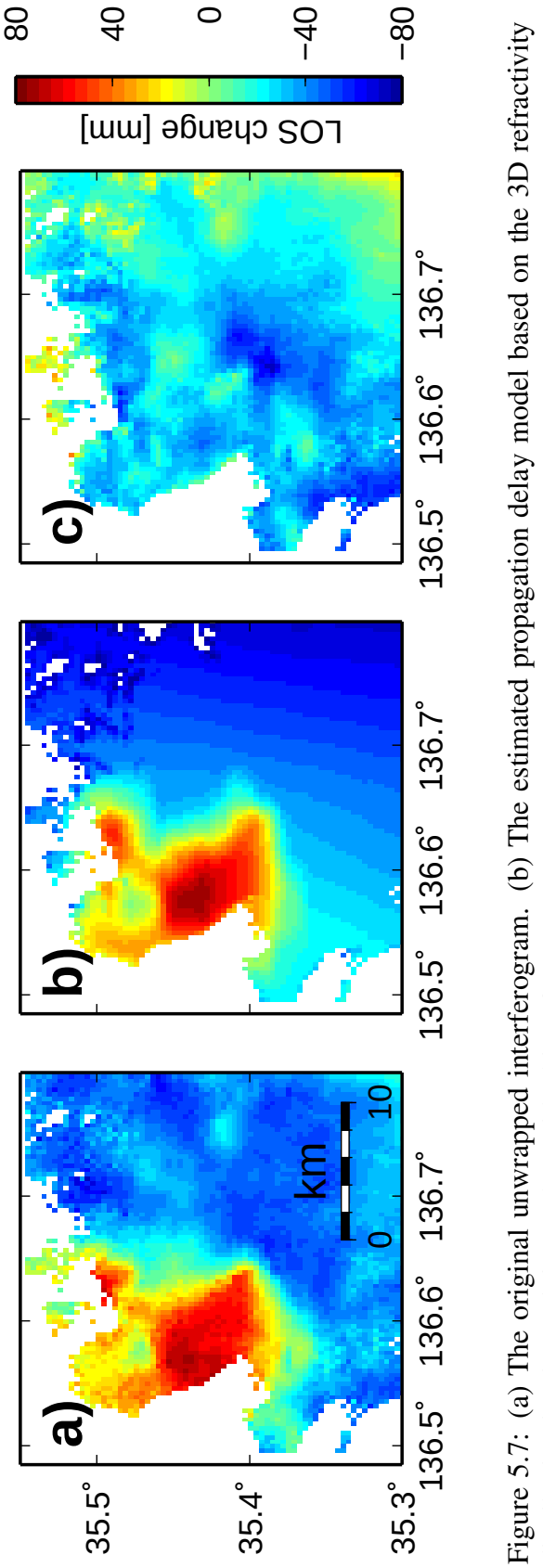

Figure 5.7: (a) The original unwrapped interferogram. (b) The estimated propagation delay model based on the 3D refractivity distribution in Figure 5.6. (c) The residual interferogram.

As an initial estimate, we established the 3D distributions of the partial pressure of dry air, as well as those of the temperature and partial water pressure of water vapor, from the 10 km mesh MSM data and the 16 vertical layers obtained from JMA. These fields were interpolated within a 100 km by 100 km square centered around anomaly A at a horizontal resolution of 1 km and with 200 vertical layers. The water vapor distribution of the location of the InSAR observation was then constructed by trial and error to clarify anomaly A in the interferogram. Two assumptions were made to derive the refractivity distribution: 1) In a convective system, air is saturated with water vapor starting at the surface and proceeding upward toward the upper troposphere; we therefore included saturated air from the lowest layer upward for the estimation: 2) Values for the partial pressure of dry air and temperature were fixed to those of the MSM because the spatial variability of these parameters is low, within a few tens of kilometers, and the MSM is considered to represent these two parameters accurately. These assumptions allowed us to estimate a feasible 3D distribution of water vapor with little ambiguity.

Although the MSM data indicated an extremely humid lower troposphere (relative humidity, RH, greater than 90 %) and a relatively dry upper troposphere (RH less than 60 %) on a synoptic scale, there were no anomalous saturated (100 % RH) signals corresponding to anomaly A. The inferred 3D refractivity distribution indicated a column of saturated air rising from the surface to 9000 m above ground level within 10 km of anomaly A (Figure 5.6). The inferred delay from this distribution can reproduce anomaly A (Figure 5.7). Although the distribution of water vapor cannot be absolutely estimated, it is clear that the humidity levels in the middle troposphere were extremely high above anomaly A. Based on the relationship between

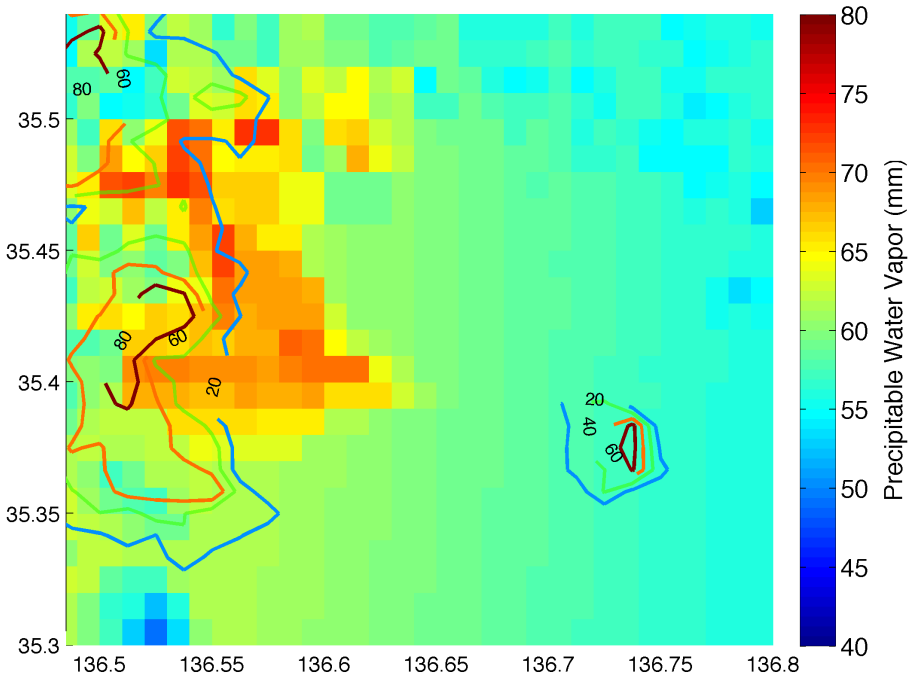

Figure 5.8: The PWV distribution derived from the estimated 3D water vapor distribution. Colored contours represent the echo distribution of the weather radar observation at the moment of SAR data acquisition.

saturated vapor and temperature, the capability of air to hold water vapor at altitudes higher than 6000 m is approximately 10 % that of the entire atmosphere. Therefore, the inferred "high humidity tower" in Figure 5.6 could realistically occur. When we calculated the zenith PWV from the estimated water vapor field, the modeled PWV approached 73 mm around anomaly A, which is approximately 13 mm higher than the mean value of the surrounding PWV. The location of the maximum PWV was also 3 km east of the location of the maximum weather radar echo. The location of the water vapor signal in the interferogram does not precisely coincide with the location of the high water vapor distribution because of its side-looking perspective.

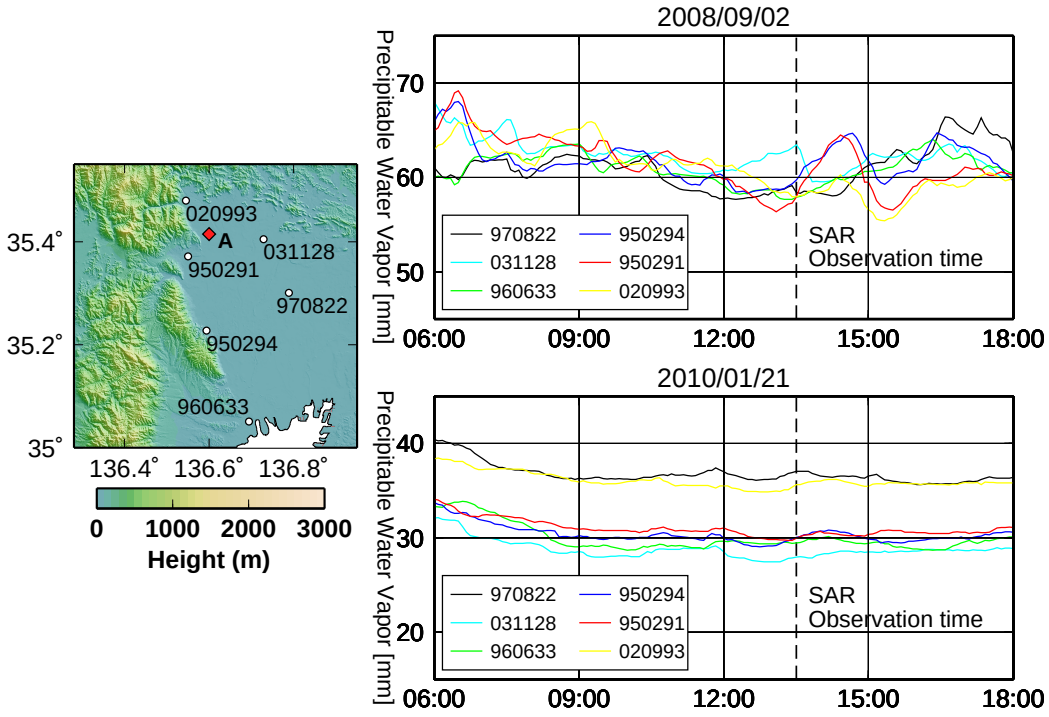

Figure 5.9: (Left) Locations of the six GEONET stations. The diamond indicates the location of anomaly A. (Upper right) The PWV time series for 2 September 2008 derived from the GEONET data using the PPP method and a time interval of 5 minutes. The vertical dashed line at 13:30 UTC indicates the SAR acquisition time, and the diamond indicates the location of anomaly A. Although there are no obvious signals indicating the existence of the deep convective system detected by the interferogram, the PWVs of all six stations are obviously different throughout the period relative to those of 21 January 2010. (Bottom right) The PWV time series derived from the GEONET data for 21 January 2010.

To validate the adequacy of our modeling, we analyzed the GPS PWV data from six GEONET stations (Figure 5.9). The GPS data were computed using the PPP method implemented in the GpsTools (Takasu and Kasai, 2005) with a time resolution of 5 minutes, and the MSM surface pressure and surface temperature data were used for the calculations of GPS PWV shown in Equation (3.36). Figure 5.9 clearly indicates that the GPS PWVs on 2 September 2008 were temporally more variable than those on 21 January 2010, revealing increases of 5-8 mm in the PWV

value at sampling stations 950291 and 950294 one hour before and after the SAR observation. These observation results are consistent with those of the InSAR observation.

During a heavy rain episode, both water vapor and hydrometeors can potentially influence the LOS changes obtained from GPS zenith total delay observation [*Brenot et al.*, 2006]. Although we have ignored the effect of hydrometeors in Figure 5.7 for the sake of simplicity, we discuss below their effect on the LOS changes, as indicated by WRF-based forward modeling results.

5.4 Propagation Delay Simulations with NWM

To clarify which local weather systems caused the localized delay signal in the interferogram, a numerical experiment for the heavy rain event was conducted using a high-resolution non-hydrostatic NWM, the WRF model [*Skamarock et al.*, 2008].

5.4.1 WRF Parameter Setting

The WRF is a non-hydrostatic numerical weather prediction model currently in operational use at NCAR and NCEP. We used WRF-ARW version 3.4 for our simulations. The data for the initial and boundary conditions of the model were constructed from the global analyses of NCEP with a $1^\circ \times 1^\circ$ resolution. Four nested grid domains were used in the simulation, with each domain centered at 35.0°N and 135.0°E. The horizontal resolutions of each domain were 9 km, 3 km, 1 km and 333 m; the horizontal resolution of the fourth domain could significantly resolve small-scale phenomena on the order of 1 km. All of the domains contained 65 verti-

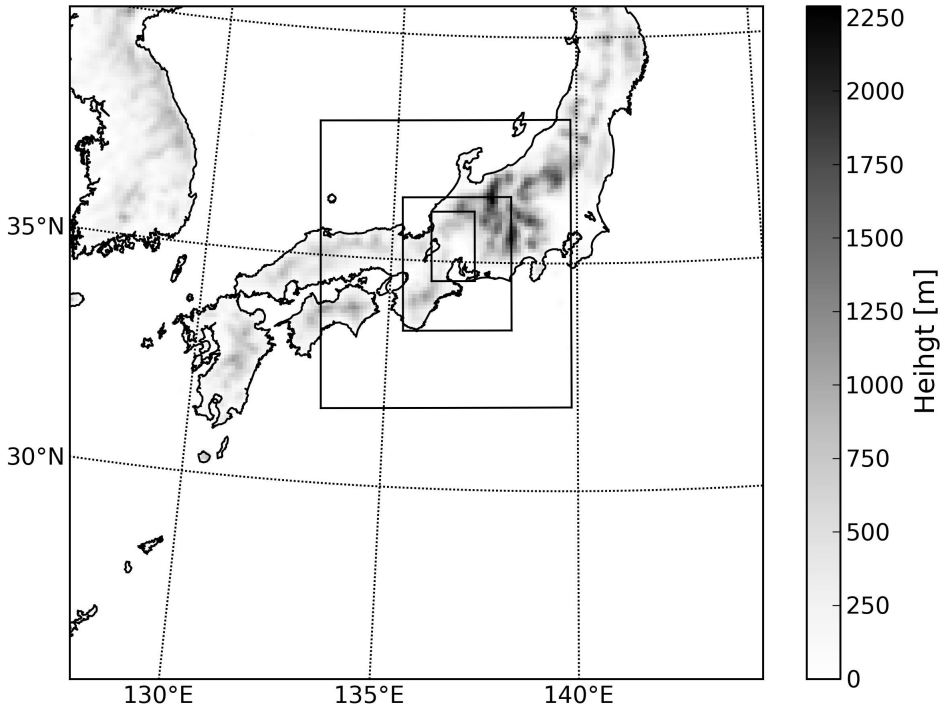

Figure 5.10: Domains of WRF simulations. The horizontal resolution of the finest domain is 333 m.

cal layers in a sigma coordinate system [*Laprise*, 1992], and all of the domain tops reached 30 km. The Morrison two-moment bulk cloud microphysics scheme [*Morrison et al.*, 2009], which accounts for six water variables (cloud water, cloud ice, rainwater, snow, graupel and hail), was used in all four of the domains. The 30-second (approximately 1 km) resolution GTOPO30 was used for the topography of our simulations. The simulations covered 12 hours, from 06:00 Coordinated Universal Time (UTC) to 18:00 UTC, for each SAR acquisition date.

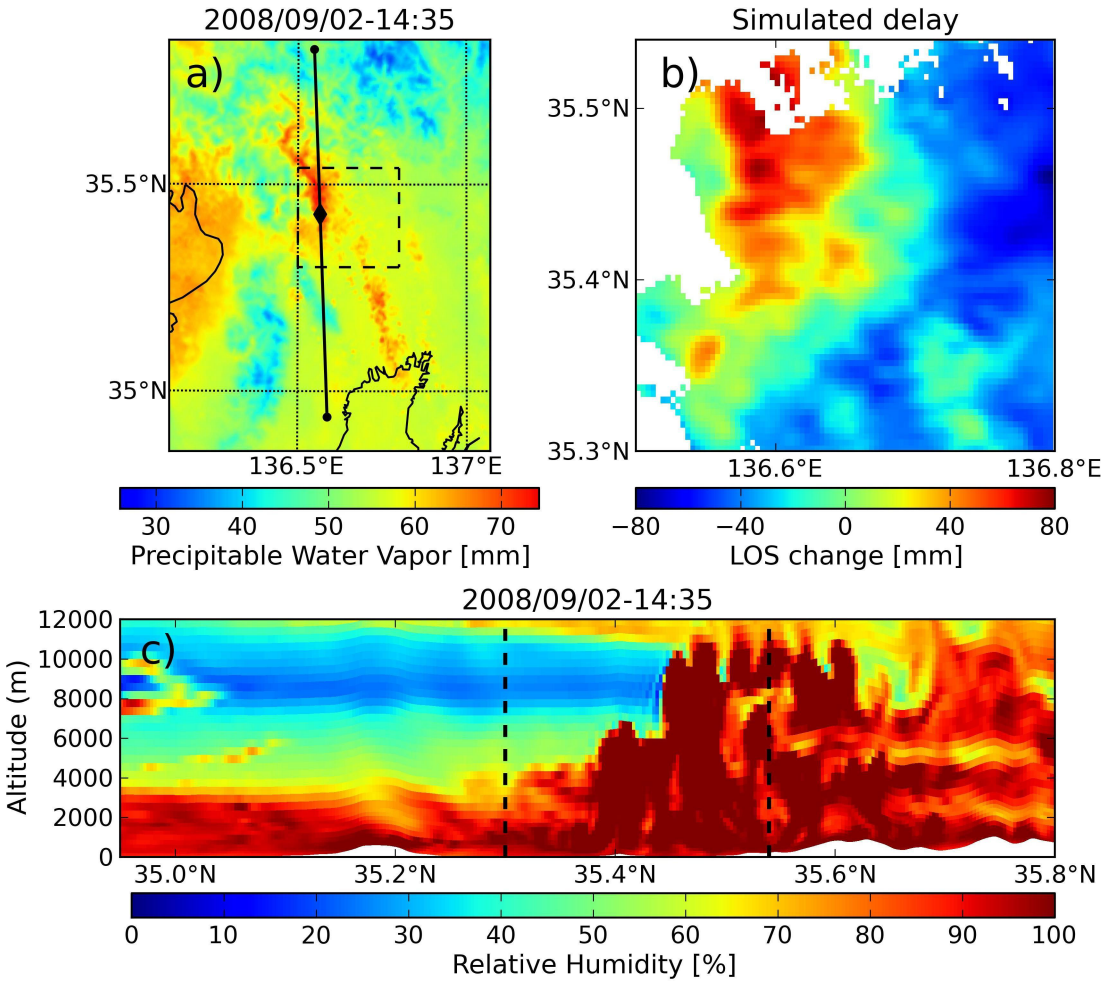

Figure 5.11: (a) The PWV distribution at 14:35 UTC on 2 September 2008 derived from the WRF simulation. The area between the dashed lines indicates the area of Figure 5.7 and 5.11b. The black line indicates the position of the profile of (c). The diamond symbol (136.56°E, 35.43°N) indicates the location of Figure 5.16. (b) The simulated total delay distribution of water vapor and hydrometeors as derived from the WRF simulations. This figure represents the difference of the two simulations corresponding to the SAR observation data for the interferogram. (c) The relative humidity profile along the black line in (a). The dashed lines indicate the upper and lower limits of the latitude in (b).

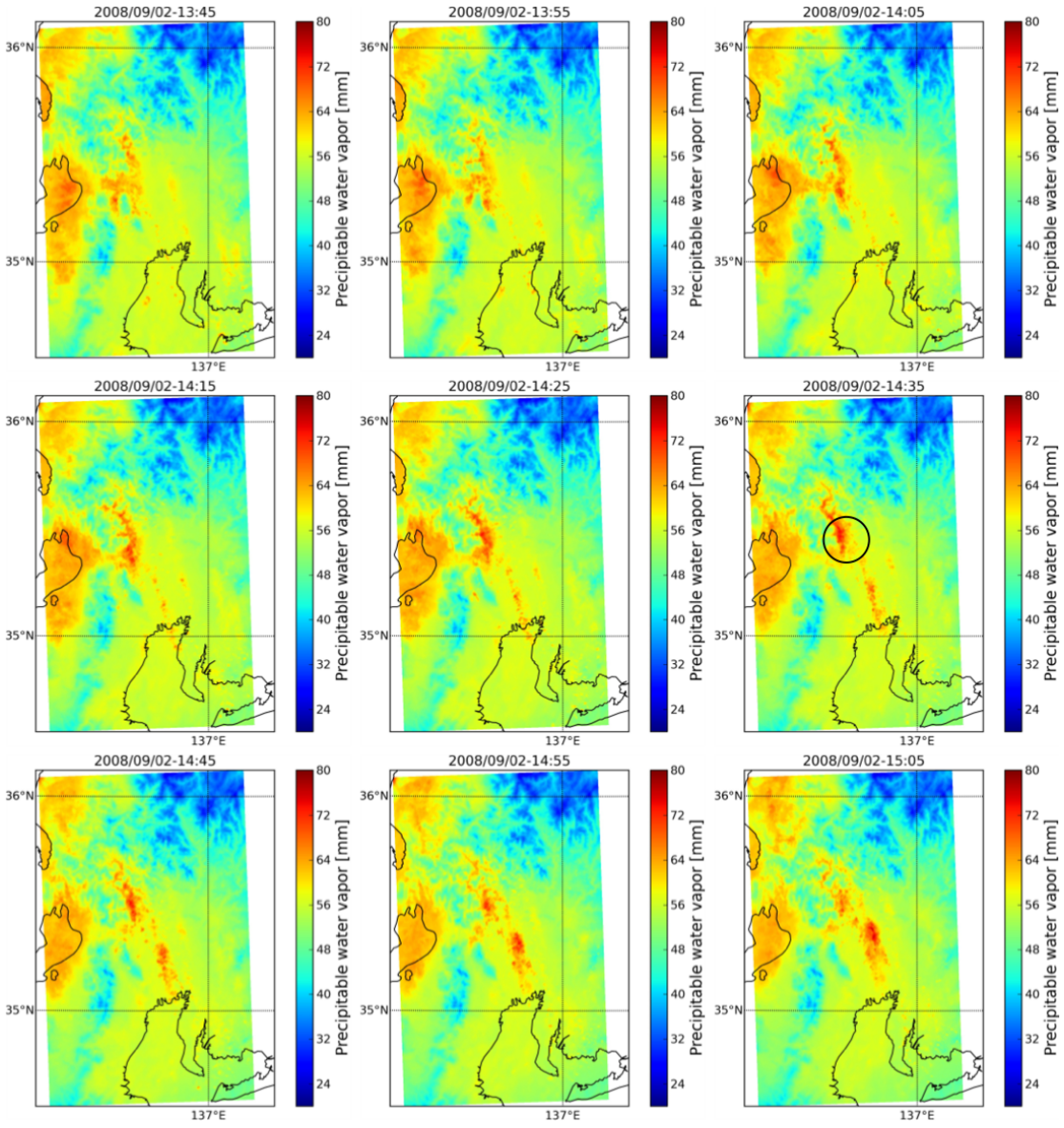

Figure 5.12: PWV time series on 2 September 2008 simulated by the WRF model. The circle at 14:35 UTC indicates the location of the anomaly A in the interferogram.

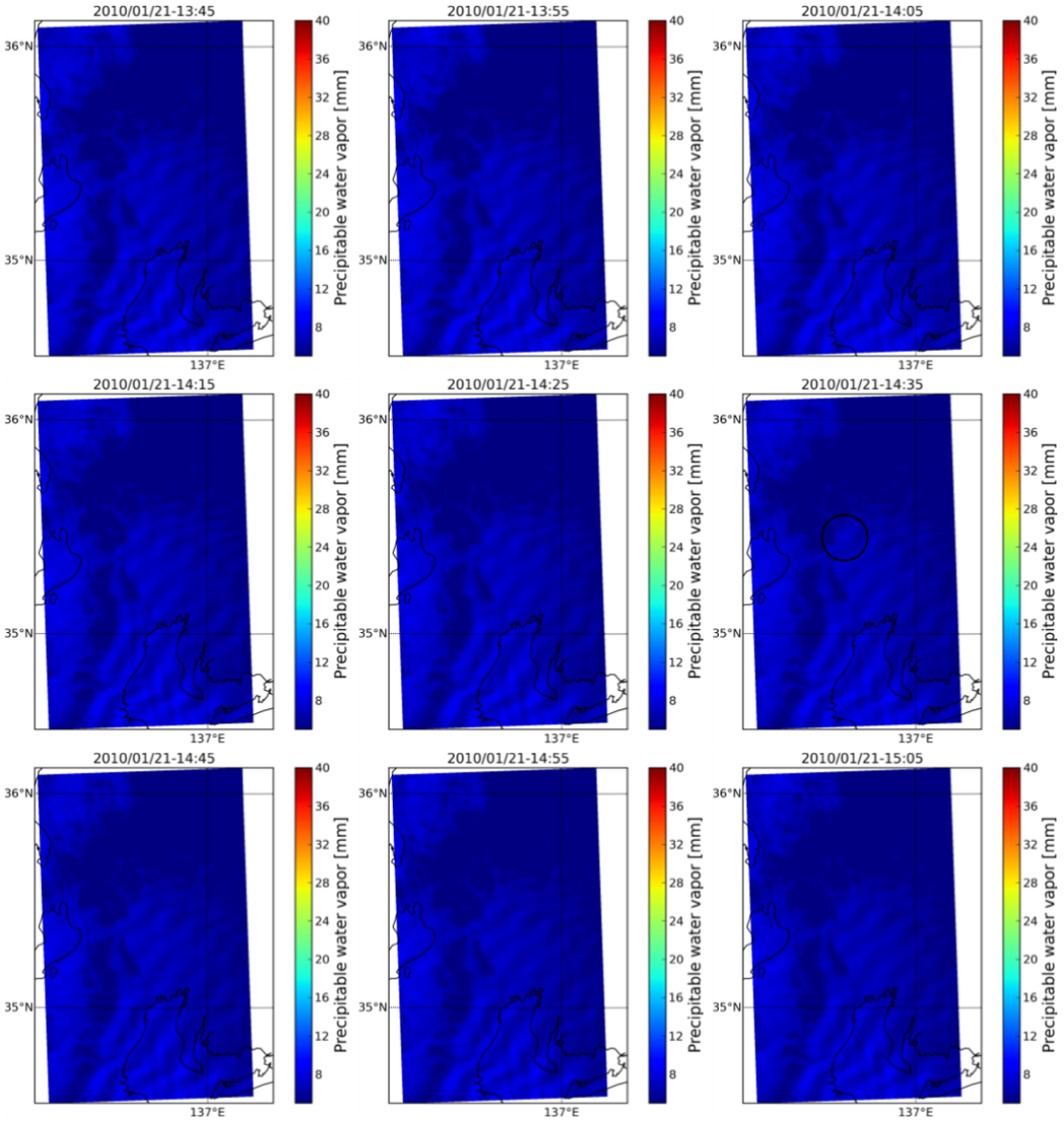

Figure 5.13: PWV time series on 21 January 2010 simulated by the WRF model. The circle at 14:35 UTC indicates the location of the anomaly A in the interferogram. It is obvious that there are not any localized signals in all epochs.

5.4.2 Simulation Results

The WRF simulations successfully reproduced a deep convection cell that passed through the location of anomaly A at 14:35 UTC, one hour after the PALSAR observation time. Although the timing difference between simulated meteorological phenomena and actual observations is an important issue in forecasting, it can be ignored when the focus of the investigation is on the processes of these phenomena [e.g. *Zhang and Zhang*, 2012]. The zenith PWV at the location of anomaly A was 15 mm higher than that around the signal (Figure 5.11a). Both the maximum amplitude and the spatial scale of the simulated propagation delay were comparable to those of the interferogram (Figure 5.11b). Although the interior of the convection was saturated with water vapor (Figure 5.11c), it also contained a significant number of hydrometeors. The amount of delay due to the hydrometeors, as calculated according to *Brenot et al.* [2006], approached 40 mm, comprising 20 % of the total delay (Figure 5.14c), although the spatial distribution of the hydrometeors was significantly more localized than that of water vapor. The simulation clearly demonstrated that a deep convective system could cause a localized delay signal with an amplitude of greater than approximately 10 cm in an interferogram (Figure 5.14d).

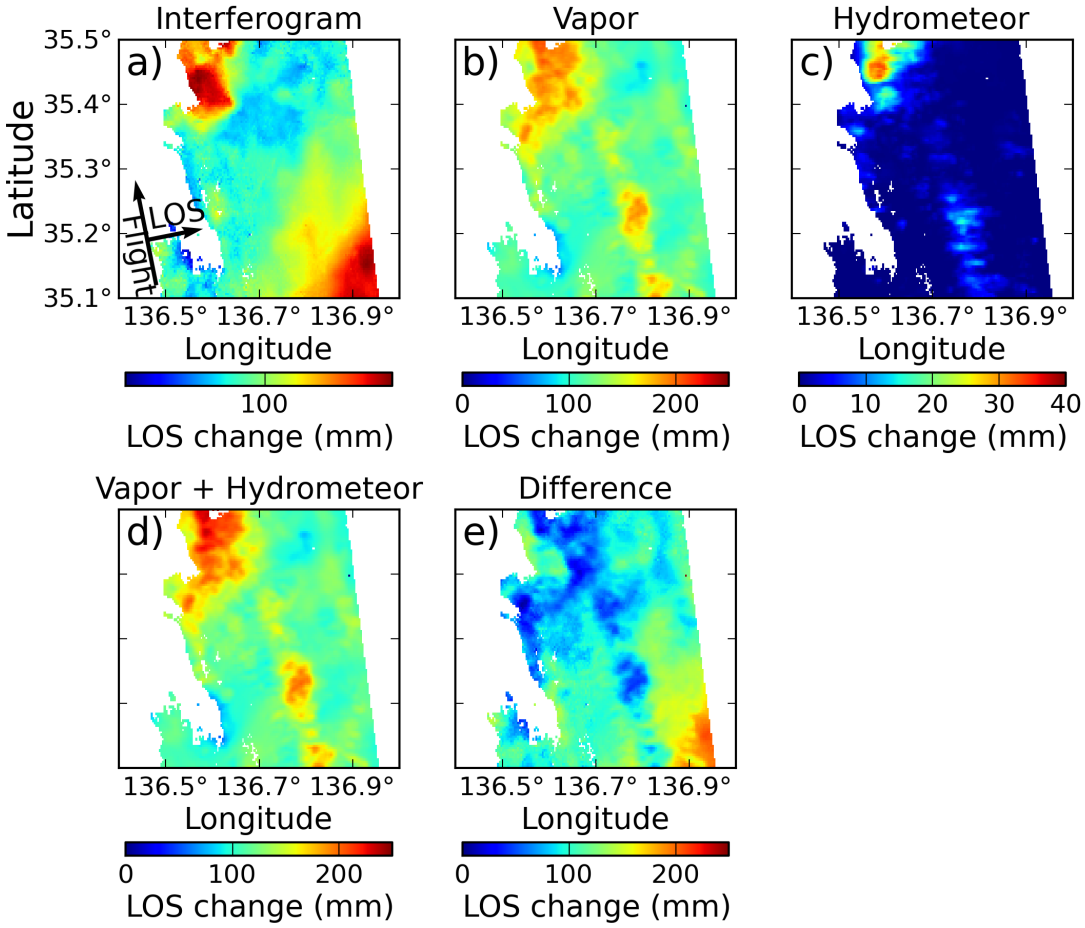

Figure 5.14: (a) The original interferogram as shown in Figure 5.2a. (b) The map of WRF-simulated delay due solely to water vapor. (c) The map of WRF-simulated delay due solely to hydrometeors. This effect reaches up to 40 mm near anomaly A. (d) The map of the combined WRF-simulated delay for b and c. (e) The residual between a and d.

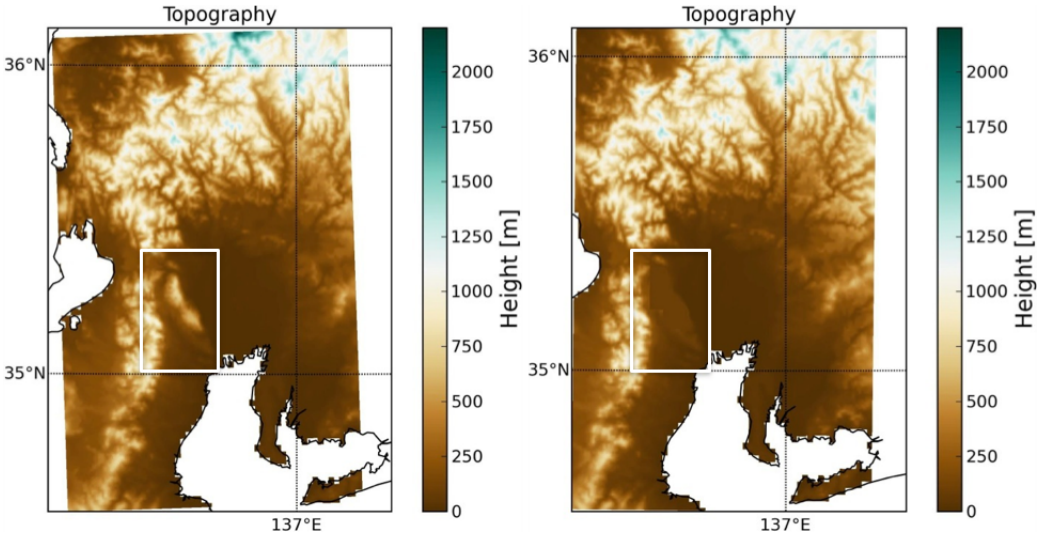

Figure 5.15: (Left) The topography used for the original simulation. (Right) The topography without the Yoro Mountain. The white square in this figure indicates the location of the Yoro mountain.

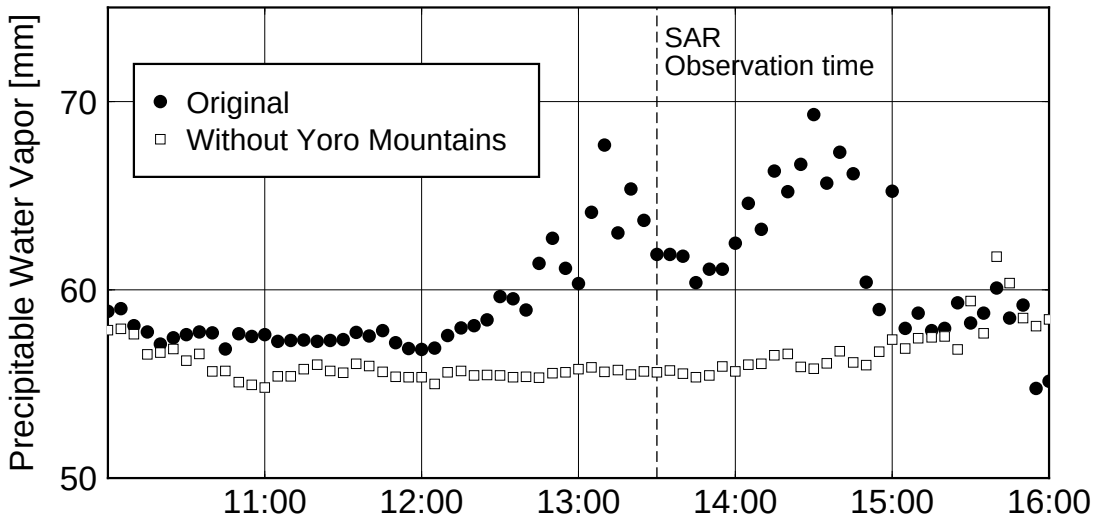

Figure 5.16: Time series of the PWV derived from the WRF simulations at 136.56°E, 35.43°N (the diamond symbol in Figure 5.11a). The dotted line indicates the PWV derived from the original simulation, and the square line indicates the PWV derived from the simulation conducted without the Yoro Mountains. The dashed line at 13:30 UTC indicates the SAR acquisition time.

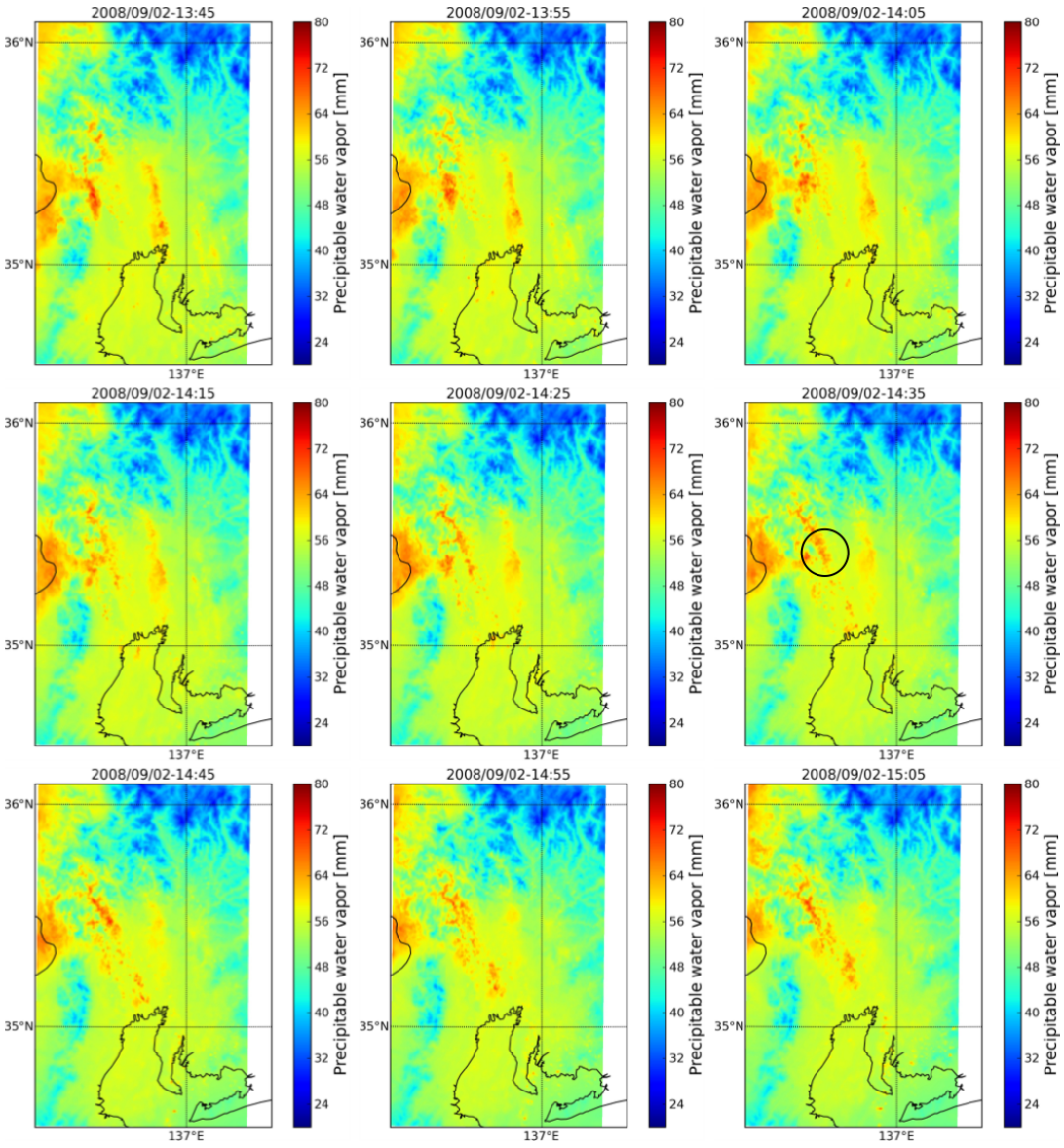

Figure 5.17: PWV time series on 2 September 2008 simulated by the WRF model without the Yoro Mountain. The circle at 14:35 UTC indicates the location of the anomaly A in the interferogram.

The PWV time series of the simulation results (Figure 5.12 and 5.13) indicate that with a background of a southerly wind, the convection was generated on the leeward side of the Yoro Mountains, which are approximately 1000 m tall (Figure 5.2b). We therefore speculated that the Yoro Mountains, 20 km south of anomaly A, contributed to the generation of the convection that caused anomaly A. To confirm this speculation, another WRF simulation was conducted in which the Yoro Mountains were removed from GTOPO30 (Figure 5.15), and this simulation did not produce the deep convective system generated in the original simulation (Figure 5.17). This conclusion was reached from the comparison of the simulated PWV time series at the location of anomaly A (Figure 5.16). During the Seino heavy rain event, the lower layer of the troposphere was extremely humid, and the higher layers of the troposphere were dry, as shown in Figure 5.6, suggesting that the conditions on the synoptic scale were very unstable. Therefore, these simulations strongly suggest that the deep convection leading to anomaly A was initiated by the orographic lift of the Yoro Mountains under unstable conditions with a background southerly wind.

5.5 Discussion

Previous studies of the mesoscale convective systems associated with extreme rain events have largely relied on data derived from weather radar systems and NWMs [e.g., *Schumacher and Johnson*, 2005]. Conventional weather radar, however, can only detect hydrometeors (rain and cloud droplets); thus, the behavior of water vapor and PWV during the the development of mesoscale convective systems remains uncertain. Although GPS-based water vapor data are helpful in this regard [e.g.,

Champollion et al., 2009; *Adams et al.*, 2011], the spatial resolution of these data is limited to only a few tens of kilometers or more due to the sparse distribution of GPS stations. The present study reports the first observational detection of the 3D water vapor structures attributable to a heavy rain episode obtained using InSAR. Although the analyzed data set is based on an emergency InSAR observation, which was a largely accidental event, more reliable opportunities to exploit InSAR data for the investigation of the water vapor behavior of mesoscale tropospheric dynamics will be available in the future, given the shorter orbital repetition intervals of future SAR missions such as ALOS-2 and Sentinel.

Chapter 6

Conclusion

In InSAR, the propagation delay due to water vapor still remains a problem to separate other geodynamical signal related to such as earthquakes and volcanic activities. Nevertheless, the study about the propagation delay due to water vapor is insufficient. On the other side, water vapor is one of the most important but poorly understood parameter for meteorology so that InSAR which has the potential to provide water vapor distributions with unprecedented spatial resolution to numerical weather simulations. For elucidating the mechanism of the behavior of water vapor and establishing the method to mitigate the neutral atmospheric delay in InSAR, it is necessary to increase studies about water vapor in both sides of space geodesy and meteorology. In this thesis we studied the behavior of water vapor in InSAR. The studies I conducted are summarized as follow:

Capter 4: Are numerical weather model outputs helpful to reduce tropospheric

delay signals in InSAR data?

1. Three types of tropospheric delay corrections (DEM-based, MSM, WRF) are applied to 54 interferograms formed from 26 SAR images.

2. The simple DEM-based approach will be more effective to correct for the tropospheric phases than corrections based on NWMs if the ”stratified” tropospheric phases are dominant.

3. If one aims to detect small amplitude deformation signals that are correlated with the topography, the NWM-based approach is preferable.

4. Further improvements are necessary in the initial and boundary values for the high spatial-temporal resolution NWM.

Capter 5: InSAR observation and numerical modeling of the water vapor signal during a heavy rain: A case study of the 2008 Seino event, central Japan

1. The localized signal during the heavy rain was detected by ALOS/PALSAR interferometry, whose amplitude reached up to 13 cm within 8 km square.

2. The 3D water vapor distribution was estimated with a ray-tracing technique, indicating a saturated air column rising from the surface to 9000 m a.g.l.

3. WRF simulations were performed, suggesting that the deep convection responsible for the localized signal was initiated by the orographic lift of the Yoro Mountain.

4. The WRF result indicated that the delay effect of hydrometeors reached up to 4 cm but localized more than that of water vapor.

After the end of twentieth century, satellite SAR missions have made it possible to capture spatial distributions of surface deformations related to geodynamical phenomena using InSAR technique, and its advanced technique like time series allows us to detect small-amplitude large-scale displacements related to plate tectonics. On the other hand, in spite of the potential that InSAR could also capture the distribution of water vapor, there have been few studies using InSAR for meteorology. The critical limitations are the long repetition period of SAR satellites and the difficulty to separate the water vapor signal from other signals. However, there is a movement to overcome former limitation to launch new SAR satellites which have shorter repetition periods (e.g. ALOS-2, Sentinel-1) and to launch so-called ”geosynchronous SAR” with a repetition period of half a day. In addition, time series analysis can be used to separate surface deformation signal from InSAR phase. Therefore InSAR will increasingly become powerful tool even for meteorologist.

Bibliography

[1] Adams, D. K., R. M. S. Fernandes, E. R. Kursinski, J. M. Maia, L. F. Sapucci *et al.* (2011), A dense GNSS meteorological network for observing deep convection in the Amazon, *Atmos. Sci. Let.*, *12*, 207–212, doi:10.1002/asl.312.

[2] Aparicio, J. M., and S. Laroche (2011), An evaluation of the expression of the atmospheric refractivity for GPS signals, *J. Geophys. Res.*, *116*, D11104, doi:10.1029/2010JD015214.

[3] Beauducel, F., P. Briole, and J. Froger (2000), Volcano-wide fringes in ERS synthetic aperture radar interferograms of Etna (1992–1998): Deformation or tropospheric effect?, *J. Geophys. Res.*, *105*(B7), 16391–16402, doi:10.1029/2000JB900095.

[4] Bechor, N. B. D., and H. A. Zebker (2006), Measuring two-dimensional movements using a single InSAR pair, *Geophys. Res. Lett.*, *33*(16), 15, doi:10.1029/2006GL026883.

[5] Berardino, P., G. Fornaro, R. Lanari, and E. Sansostic (2002), A New Algorithm for Surface Deformation Monitoring Based on Small Baseline Dif-

ferential SAR Interferograms, *IEEE. Trans. Geosci. Remote Sensing*, *40*(11), 2375-2383, doi:10.1109/TGRS.2002.803792.

[6] Bevis, M., S. Businger, T. A. Herring, C. Rocken, R. A. Anthes, and R. H. Ware (1992), GPS meteorology: Remote Sensing of Atmospheric Water Vapor Using the Global Positioning System, *J. Geophys. Res.*, *97*D14, 15787–15801, doi:10.1029/92JD01517.

[7] Bevis, M., S. Businger, S. Chiswell, T. A. Herring, R. A. Anthes, C. Rocken, and R. H. Ware (1994), GPS meteorology: Mapping zenith wet delays onto precipitable water, *J. Appl. Meteor.*, *33*, 379-386, doi: http://dx.doi.org/10.1175/1520-0450(1994)033¡0379:GMMZWD¿2.0.CO;2.

[8] Boehm, J., B. Werl, and H. Schuh (2006), Troposphere mapping functions for GPS and very long baseline interferometry from European Centre for Medium-Range Weather Forecasts operational analysis data, *J. Geophys. Res.*, *111*B2, doi:10.1029/2005JB003629.

[9] Boehm, J. A. Niell, P. Tregoning, and H. Schuh (2006), Global Mapping Function (GMF): A new empirical mapping function based on numerical weather model data, *Geophys. Res. Lett.*, *33*(L07304), doi:10.1029/2005GL025546.

[10] Brenot, M., V. Ducrocq, A. Walpersdorf, C. Champollion, and O. Caumont (2006), GPS zenith delay sensitivity evaluated from high-resolution NWP simulations of the 8–9 September 2002 flash-flood over southeastern France, *J. Geophys. Res.*, *111*, D15105, doi:10.1029/2004JD005726.

[11] Bürgmann, R., D. Schmidt, R. M. Nadeau, M. d'Alessio, E. Fielding, D. Manaker, T. V. McEvilly, and M. H. Murray (2000), Earthquake potential along the northern Hayward fault, California, *Science*, *289*, 1178-1182, doi:10.1126/science.289.5482.1178.

[12] Cavalié, O., C. Lasserre, M. P. Doin, G. Peltzer, S. Jianbao, X. Xiwei, and Z. K. Shen (2008), Measurement of interseismic strain across the Haiyuan fault (Gansu, China), by InSAR, *Earth Planet. Sci. Lett.*, *275*, 246-257, doi:10.1016/j.epsl.2008.07.057.

[13] Champolion, C., C. Flamant, O. Bock, F. Masson, D. D. Turner, and T. Weckwerth (2009), Mesoscale GPS tomography applied to the 12 June 2002 convective initiation event of IHOP_2002, *Q. J. R. Meteorol. Soc.*, *135*, 645–662, doi:10.1002/qj.386.

[14] Chan, S. T., T. F. Chan, and W. K. Wong (2010), An Intercomparison of WRF-ARW and JMA-NHM Performance in Prediction of Tropical Cyclones over the South China Sea in 2008, 29th Conference on Hurricanes and Tropical Meteorology, *American Meteorological Society*, P2.62.

[15] Cumming, I. G., and Wong, F. H. (2005), Digital Processing of Synthetic Aperture Radar Data: Algorithms and Implementation, *Artech House Print on Demand*.

[16] Curlander, J. C., and McDonough, R. N. (1991), Synthetic Aperture Radar: Systems and Signal Processing, *Wiley-Interscience; 1 edition*.

[17] Davis, J. L., T. A. Herring, I. I. Shapiro, A. E. Rogers, and G. Elgered (1985), Geodesy by radio interferometry: Effects of atmospheric modeling errors on estimates of baseline length, *Radio Sci.*, *20*, 1593–1607.

[18] Doin, M., C. Lasserre, G. Peltzer, O. Cavalié, and C. Doubre (2009), Corrections of stratified tropospheric delays in SAR interferometry: Validation with global atmospheric models, *J. Appl. Geophys.*, *69*, pp. 35-50, doi:10.1016/j.jappgeo.2009.03.010.

[19] Elgered, G. (1993), Tropospheric radio path delay from ground-based microwave radiometry, in *Atmospheric Remote Sensing by Microwave Radiometry*, edited by M. A. Janssen, pp. 215-258.

[20] Elliot, J. R., J. Biggs, B. Parsons, and T. J. Wright (2008), InSAR slip rate determination on the Altyn Tagh Fault, northern Tibet, in the presence of topographically correlated atmospheric delays, *Geophys. Res. Lett.*, *35*, L12309, doi:10.1029/2008GL033659.

[21] Ferreti, A., C. Prati, and F. Rocca (2000), Nonlinear Subsidence Rate Estimation Using Permanent Scatterers in Differential SAR Interferometry, *IEEE. Trans. Geosci. Remote Sensing*, *38*(5), 2202-2212.

[22] Foster, J., B. Brooks, T. Cherubini, C. Shacat, S. Businger, and C. Werner (2006), Mitigating atmospheric noise for InSAR using a high resolution weather model., *Geophys. Res. Lett.*, *33*, L16304, doi: 10.1029/2006GL026781.

[23] Foster, J., J. Kealy, T. Cherubini, S. Businger, Z. Lu, and M. Murphy (2013), The utility of atmospheric analyses for the mitigation of artifacts in InSAR, *J. Geophys. Res.*, *118*(2), 748–758, doi:10.1002/jgrb.50093.

[24] Fournier, T., M. E. Pritchard, and N. Finnegan (2000), Accounting for atmospheric delays in InSAR data in a search for long-wavelength deformation in South America, *IEEE. Trans. Geosci. Remote Sensing*, *99*, 1-12, doi:10.1109/TGRS.2011.2139217.

[25] Fujiwara, S., P. A. Rosen, M. Tobita, and M. Murakami (1998), Crustal deformation measurements using repeat-pass JERS 1 synthetic aperture radar interferometry near the Izu Peninsula, Japan, *J. Geophys. Res.*, *103*, 2411-2426, doi: 10.1029/97JB02382.

[26] Fujiwara, S., M. Tobita, M. Murakami, H. Nakagawa, and P. A. Rosen (1999), Baseline Determination and Correction of Atmospheric Delay Induced by Topography of SAR Interferometry for Precise Surface Change Detection (in Japanese with abstract and figure captions in English), *J. Geod. Soc. Jpn.*, *45*(4), 315-325.

[27] Furuya, M., K. Mueller, and J. Wahr (2007), Active salt tectonics in the Needles Distinct, Canyonlands (Utah) as detected by interferometric synthetic aperture radar and point target analysis, *J. Geophys. Res.*, *112*, B06418, doi:10.1029/2006JB004302.

[28] Furuya, M. (2011), SAR Interferometry, in *Encyclopedia of Solid Earth Geophysics*, Part 16, 1041–1049, ed. H. Gupta.

[29] Galloway, D. L., K. W. Hudnut, S. E. Ingebritsen, S. P. Phillips, G. Peltzer, F. Rogez, and P. A. Rosen (1998), Detection of aquifer system compaction and land subsidence using interferometric synthetic aperture radar, Antelope Valley, Mojave Desert, California, *Water Resources Res.*, *34*(10), 2573–2585, doi:10.1029/98WR01285.

[30] Goldstein, R. M., H. Engelhardt, B. Kamb, and R. M. Frolich (1993), Sattelite radar interferometry for monitoring ice-sheet motion - Application to an antarctic ice stream, *Science*, *262*, 1525-1530, doi:10.1126/science.262.5139.1525.

[31] Goldstein, R. M., and C. L. Werner (1998), Radar interferogram filtering for geophysical applications, *Geophys. Res. Lett.*, *25*, doi:10.1029/1998GL900033.

[32] Gray, A. L., K. E. Mattar, and G. Sofko (2000), Influence of ionospheric electron density fluctuations on satellite radar interferometry, *Geophys. Res. Lett.*, *27*(10), 1451–1454, doi:10.1029/2000GL000016.

[33] Hanssen, R. (1998), Atmospheric heterogeneities in ERS tandem SAR interferometry, chapter 2, *Delft University Press*, The Netherland.

[34] Hanssen, R. F., T. M. Weckwerth, H. A. Zebker, and R. Klees (1999), High-resolution water vapor mapping from interferometric radar measurements, *Science*, *283*, 1297–1299, doi:10.1126/science.283.5406.1297.

[35] Hanssen, R. F. (2001), Radar Interferometry: Data Interpretation and Analysis, *Kluwer Acad., Norwell, Mass.*

[36] Hobiger, T., R. Ichikawa, Y. Koyama, and T. Kondo (2008), Fast and accurate ray-tracing algorithms for real-time space geodetic applications using numerical weather models, *J. Geophys. Res.*, *113*, D20302, doi:10.1029/2008JD010503.

[37] Hobiger, T., Y. Kinoshita, S. Shimizu, R. Ichikawa, M. Furuya, T. Kondo, and Y. Koyama (2010), On the importance of accurately ray-traced troposphere corrections for Interferometric SAR data, *J. Geodesy*, doi:10.1007/s00190-010-0393-3.

[38] Hooper, A., H. Zebker, P. Segall, and B. Kampes (2004), A new method for measuring deformation on volcanoes and other natural terrains using InSAR persistent scatterers, *Geophys. Res. Lett.*, *31*, L23611, doi:10.1029/2004GL021737.

[39] Hufford, G. (1991), A model for the complex permittivity of ice at frequencies below 1 THz, *Int. J. Infrared Millimeter Waves*, *12*(7), 677–682, doi:10.1007/BF01008898.

[40] Jolivet, R., R. Grandin, C. Lasserre, M. P. Doin, and G. Peltzer (2011), Systematic InSAR tropospheric phase delay corrections from global meteorological reanalysis data, *Geophys. Res. Lett.*, *38*(17), doi: 10.1029/2011GL048757.

[41] Laprise, R. (1992), The Euler equations of motion with hydrostatic pressure as an independent variable, *Mon. Weather Rev.*, *120*, 197–207, doi:10.1175/1520-0493(1992)120<0197:TEEOMW>2.0.CO;2.

[42] Li, Z., J. P. Muller, P. Cross, and E. J. Fielding (2005), Interferometric synthetic aperture radar (InSAR) atmospheric correction: GPS, Moderate Resolution Imaging Spectroradiometer (MODIS), and InSAR integration, *J. Geophys. Res.*, *110*, B03410, doi:10.1029/2004JB003446.

[43] Li, Z., E. J. Fielding, P. Cross, and J. P. Muller (2006), Interferometric synthetic aperture radar atmospheric correction: Medium Resolution Imaging Spectrometer and Advanced Synthetic Aperture Radar integration, *Geophys. Res. Lett.*, *33*, L06816, doi:10.1029/2005GL025299.

[44] Lin, Y. N., M., Simons, E. A. Hetland, P. Muse, and C. DiCaprio (2010), A Multiscale approach to estimating topographically correlated propagation delays in radar interferograms, *Geochem. Geophys. Geosyst.*, *11*, Q09002, doi:10.1029/2010GC003228.

[45] Massonnet, D., M. Rossi, C. Carmona, F. Adragna, G. Peltzer, K. Feigl, and T. Raboute (1993), The displacement field of the Landers earthquake mapped by radar interferometry, *Nature*, *364*, 138-142, doi:10.1038/364138a0.

[46] Massonnet, D., and K. L. Feigl (1998), Radar interferometry and its application to changes in the earth's surface, *Rev. Geophys.*, *36*(4), 441-500, doi:10.1029/97RG03139.

[47] Massonnet, D., and K. L. Feigl (2010), Radar interferometry and its application to changes in the Earth 's surface, *Rev. Geophys.*, *36*(4), 441–500, doi:10.1029/97RG03139.

[48] Mätaler, C. (1996), Microwave permittivity of dry snow, *IEEE. Trans. Geosci. Remote Sensing*, *34*(2), 573–581, doi:10.1109/36.485133.

[49] Mateus, P., G. Nico, and J. Catalão (2013), Can spaceborne SAR interferometry be used to study the temporal evolution of PWV?, *Atmos. Res.*, *119*, 70–80, doi:10.1016/j.atmosres.2011.10.002.

[50] Meyer, F., R. Bamler, N. Jakowski, and T. Fritz (2006), The potential of low-frequency sar systems for mapping ionospheric tec distributions, *Geosci. Remote Sens. Lett.*, *3*(4), 560–564, doi:10.1109/LGRS.2006.882148.

[51] Meyer, F., R. Bamler, N. Jakowski, and T. Fritz (2006), Methods for small scale ionospheric TEC mapping from broadband L-band SAR data, in *Proc. IGARSS*, Denver, CO, Jul. 31-Aug. 4, 3735-3738.

[52] Meyer, F., and D. Sandwell (2012), SAR interferometry at Venus for topography and change detection, *Planet. Space Sci.*, *73*(1), 130–144, doi:10.1016/j.pss.2012.10.006.

[53] Morrison, H., G. Thompson, and V. Tatarskii (2009), Impact of cloud microphysics on the development of trailing stratiform precipitation in a simulated squall line: Comparison of one- and two-moment schemes, *Mon. Weather Rev.*, *137*, 991–1007, doi:10.1175/2008MWR2556.1.

[54] Niell, A. E. (1996), Global mapping functions for the atmosphere delay at radio wavelengths, *J. Geophys. Res.*, *101*, No. B2, 3227–3246, doi:10.1029/95JB03048.

[55] Niell, A. E. (2001), Preliminary evaluation of atmospheric mapping functions based on numerical weather models, *Phys. Chem. Earth*, *26*, 475–480, doi:10.1016/S1464-1895(01)00087-4

[56] Ning, T., G. Elgered, U. Willén, and J. Johansson (2013), Evaluation of the atmospheric water vapor content in a regional climate model using ground-based GPS measurements, *J. Geophys. Res.*, *118*, 1–11, doi:10.1029/2012JD018053.

[57] Onn, F., and H. A. Zebker (2006), Correction for interferometric synthetic aperture radar atmospheric phase artifacts using time series of zenith wet delay observations from a GPS network, *J. Geophys. Res.*, *111*, B09102, doi:10.1029/2005/JB004012.

[58] Otsuka, A., S. Kobayashi, and H. Seko (2002), A wind-induced delay pattern in SAR interferometry and numerical simulation, *J. Jpn. Soc. Photogrammetry and Remote Sensing*, *41*(4), 85-98.

[59] Ozawa, T. and S. Shimizu (2010), Atmospheric noise reduction in InSAR analysis using numerical weather model (in Japanese with abstract and figure captions in English), *J. Geod. Soc. Jpn.*, *56*(4), 137–147.

[60] Puysségur, B., R. Michel, and J. Avouac (2007), Tropospheric phase delay in interferometric synthetic aperture radar estimated from meteorological model and multispectral imagery, *J. Geophys. Res.*, *112*, B05419, doi:10.1029/2006JB004352.

[61] Raucoules, D., and M. Michele (2010), Assessing Ionospheric Influence on L-Band SAR Data: Implications on Coseismic Displacement Measurements

of the 2008 Sichuan Earthquake, *IEEE. Trans. Geosci. Remote Sensing*, *7*(2), 286–290, doi:10.1109/LGRS.2009.2033317.

[62] Saastamoinen, J. (1972), Atmospheric correction for the troposphere and stratosphere in radio ranging of satellites, in *The Use of ArtificialSatellites for Geodesy*, *Geophys. Monogr. Ser.*, vol. 15, edited by S. W. Henriksen, A. Mancini, and B. H. Chovitz, pp. 247–251, AGU, Washington,

[63] Saepuloh, A., M. Urai, N. Aisyah, C. Widiwijayanti, and P. Jousset (2013), Interpretation of ground surface changes prior to the 2010 large eruption of Merapi volcano using ALOS/PALSAR, ASTER TIR and gas emission data, *J. Volcanol. Geotherm. Res.*, 261, 130143, doi:10.1016/j.jvolgeores.2013.05.001.

[64] Sandwell, D., and L. Sichoix (2000), Topographic phase recovery from stacked ERS interferometry and a low ‐ resolution digital elevation model, *J. Geophys. Res.*, *105*(B12), 28211–28222, doi:10.1029/2000JB900340.

[65] Schumacher, R. S., and R. H. Johnson (2005), Organization and environmental properties of extreme-rain-producing mesoscale convective systems, *Mon. Weather Rev.*, *133*(4), 961–976, doi:10.1175/MWR2899.1.

[66] Shimada, M. (1999), Correction of the Satellite's State Vector and the Atmospheric Excess Path Delay in the SAR Interferometry –An Application to Surface Deformation Detection– (in Japanese with abstract and figure captions in English), *J. Geod. Soc. Jpn.*, *45*(4), 327-346.

[67] Shimada, M., Y. Muraki, and Y. Otsuka (2008), Discovery of anomalous stripes over the Amazon by the PALSAR onboard ALOS satellite, in *Proc. IEEE IGARSS*, Jul. 2008, pp.II-387-II-390.

[68] Shirzaei, M., and T. R. Walter (2011), Estimating the Effect of Satellite Orbital Error Using Wavelet-Based Robust Regression Applied to InSAR Deformation Data, *IEEE. Trans. Geosci. Remote Sensing*, *49*(11), 4600–4605, doi:10.1109/TGRS.2011.2143419.

[69] Shoji, Y., M. Kunii, and K. Saito (2009), Assimilation of Nationwide and Global GPS PWV Data for a Heavy Rain Event on 28 July 2008 in Hokuriku and Kinki, Japan, *Sci. Online Lett. Atmos.*, *5*, 45–48, doi:10.2151/sola.2009-012.

[70] Simons, S. and P. A. Rosen (2009), Interferometric Synthetic Aperture Radar, in *Geodesy, Treatise on Geophysics*, *3*, 391–446, ed. T. Herring, Elsevier.

[71] Skamarock, W. C., J. B. Klemp, J. Dudhia, D. O. Gill, D. M. Barker *et al.* (2008), A description of the Advanced Research WRF version 3, *NCAR Tech Note NCAR/ TN-475+STR*, 113 pp. NOAA, Boulder, Colo.

[72] Solheim, F., J. Vivekanandan, R. H. Ware, and C. Rocken (1999), Propagation delays induced in GPS signals by dry air, water vapor, hydrometeors and other particulates, *J. Geophys. Res.*, *104*(D8), 9663–9670, doi:10.1029/1999JD900095.

[73] Takasu, T., and S. Kasai (2005), Evaluation of GPS Precise Point Positioning (PPP) Accuracy, *IEICE Technical Report*, *105*(208), 40–45.

[74] Tesmer, V., J. Boehm, R. Heinkelmann, and H. Schuh (2007), Effects of different tropospheric mapping functions on the TRF, CRF, and position time-series estimated from VLBI, *J. Geodesy*, *81*, 6–8, 409–421, doi:10.1007/s00190-006-0126-9.

[75] Thayer, G. D. (1974), An improved equation for the radio refractive index of air, *Radio Sci.*, *9*(10), 803–807.

[76] Wadge, G., P. W. Webley, I. N. James, R. Bingley, A. Dodson, S. Waugh, T. Veneboer, G. Puglisi, M. Mattia, D. Baker, S. C. Edwards, S. J. Edwards, and P. J. Clarke (2002), Atmospheric models, GPS and InSAR measurements of the tropospheric water vapour field over Mount Etna, *Geophys. Res. Lett.*, *29*, doi:10.1029/2002GL015159.

[77] Wadge, G., M. Zhu, R. J. Holley, I. N. James, P. A. Clark, C. Wang, and M. J. Woodage (2010), Correction of atmospheric delay effects in radar interferometry using a nested mesoscale atmospheric model, *J. Appl. Geophys.*, *72*(2), 141–149.

[78] Zebker, H. A., P. A. Rosen, and S. Hensley (1997), Atmospheric effects in interferometric synthetic aperture radar surface deformation and topographic maps, *J. Geophys. Res.*, *102*, 7547–7563, doi:10.1029/96JB03804.

[79] Zhang, M., and D. L. Zhang (2012), Subkilometer Simulation of a Torrential-Rain-Producing Mesoscale Convective System in East China. Part I: Model Verification and Convective Organization, *Mon. Weather Rev.*, *140*, 184–201, doi:10.1175/MWR-D-11-00029.1.